ELECTRONIC SUPPLEMENTARY INFORMATION

Shedding a new light on quadrupolar 1,4-dihydropyrrolo [3,2-*b*]pyrroles: impact of electron-deficient scaffolds over emission

Bartosz Szymański,[a,b] Smruti Ranjan Sahoo,[c] Olena Vakuliuk,[a] Rashid Valiev,[d]
Ruslan Ramazanov,[d] Piotr Łaski,[b] Katarzyna N. Jarzembska,[b] Radosław Kamiński,[b]
Mohammad B. Teimouri,*[a,e] Glib Baryshnikov,*[c] Daniel T. Gryko *[a]

[a] Institute of Organic Chemistry, Polish Academy of Sciences, Kasprzaka 44/52, 01-224 Warsaw, Poland
[b] Department of Chemistry, University of Warsaw, Żwirki i Wigury 101, 02-089 Warsaw, Poland
[c] Laboratory of Organic Electronics, Department of Science and Technology, Linköping University, SE-60174 Norrköping, Sweden
[d] Department of Chemistry, University of Helsinki, FI-00014 Helsinki, Finland
[e] Faculty of Chemistry, Kharazmi University, 15719-14911 Tehran, Iran

1. General remarks

All chemicals were used as received unless otherwise noted. Transformations with air and oxygen sensitive compounds were performed under a stream of argon. The reaction progress was monitored by means of thin layer chromatography (TLC), which was performed on aluminium foil plates, covered with Silica gel 60 F254 (Merck). The pyrrolo[3,2-b]pyrroles' syntheses were conducted based on conditions optimized in previous publication.[1] The identity and purity of prepared compounds were proved by ^{1}H NMR and ^{13}C NMR spectroscopy as well as by mass spectrometry (APCI-MS or EI-MS). NMR spectra were measured on Varian 500 MHz and Varian 600 MHz instruments. Chemical shifts for ^{1}H NMR are expressed in parts per million (ppm) relative to tetramethylsilane (δ = 0.00 ppm) or chloroform-d (δ = 7.26 ppm). Chemical shifts for ^{13}C NMR are expressed in ppm relative to chloroform-d (δ = 77.0 ppm). Data are reported as follows: chemical shift, multiplicity (s = singlet, d = doublet, dd = doublet of doublets, t = triplet, td = triplet of doublets, q = quartet, quint = quintet, sex = sextet, m = multiplet), coupling constant (in Hz) and integral. All melting points for crystalline products were measured with automated melting point apparatus EZ-MELT and were given without correction.

2. Synthetic procedures

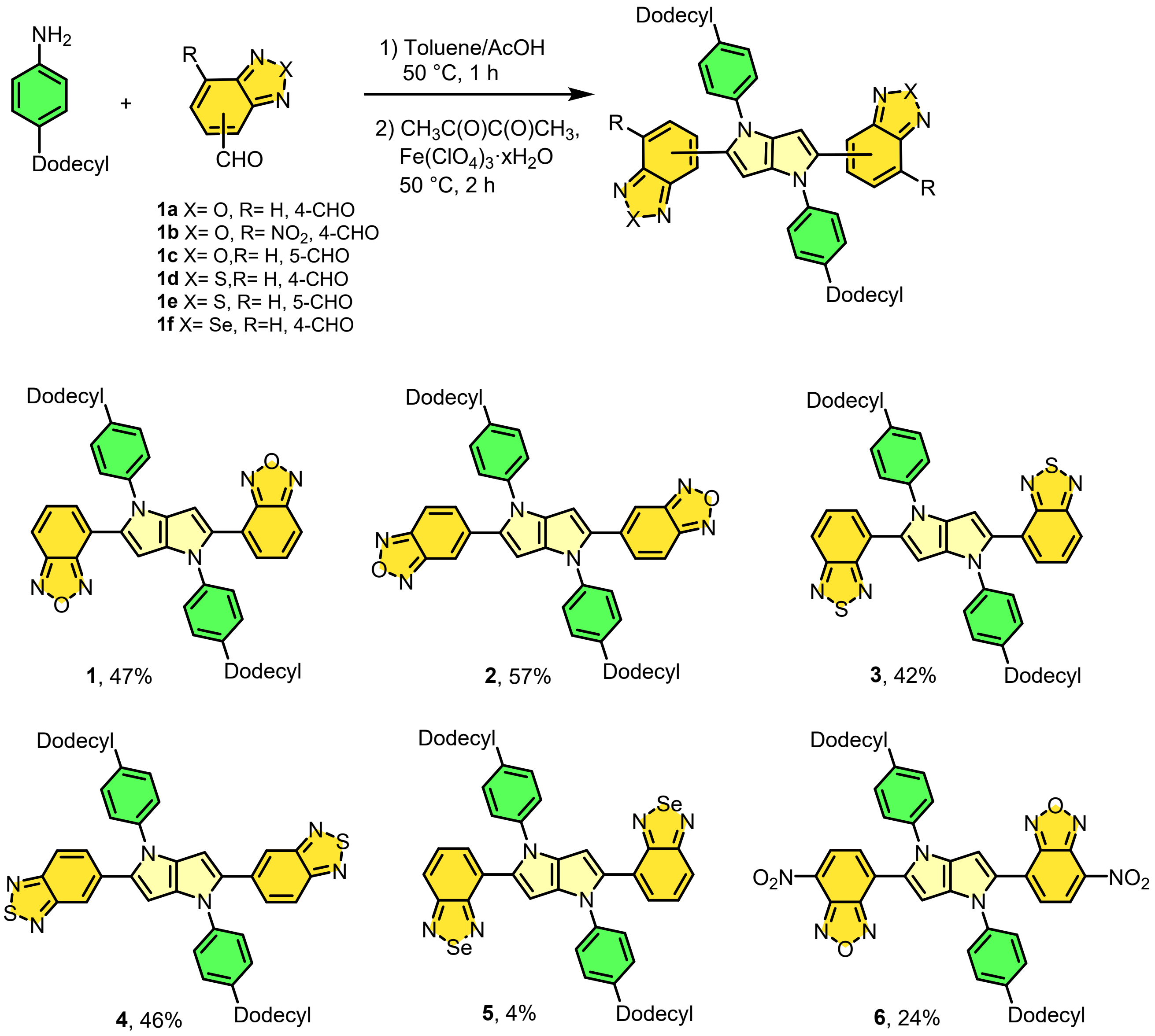

Scheme S1. Synthesis of centrosymmetric **1**–**6** TAPPs.

The preparation of **2,5-bis(4-(2,1,3-benzoxadiazolyl))-1,4-bis(4-dodecylphenyl)-1,4-dihydropyrrolo[3,2-b]pyrrole** (**1**) has been reported elsewhere and its spectral properties concur with the literature data.[2]

2,5-Bis(5-(2,1,3-benzoxadiazolyl))-1,4-bis(4-dodecylphenyl)-1,4-dihydropyrrolo[3,2-*b*]pyrrole (**2**): Glacial acetic acid (2 mL), toluene (2 mL), benzo[*c*][1,2,5]oxadiazole-5-carbaldehyde (**1c,** 296 mg, 2 mmol, 2 eq.) and 4-dodecylaniline (522 mg, 2 mmol, 2 eq.) were placed in a 50 mL round-bottom flask equipped with a magnetic stir bar. The mixture was reacted at 50°C for 1 h in open flask. After that time, $Fe(ClO_4)_3 \cdot \times H_2O$ (20 mg, 5 mol$_{\%}$) was added, followed by butane-2,3-dione (87 μL, 1 mmol, 1 eq.). The resulting mixture was stirred at 50°C (oil bath) in an open flask under air for 17 hours. Next, 3 mL of acetonitrile was added which resulted in precipitation of orange crystals of **2**. They were recrystallized from mixture of dichloromethane and hexanes, affording 476 mg (57%) of pure product as an orange solid. M.p. 175−176 °C (DCM/hexanes). ^{1}H NMR (500 MHz, chloroform-d) δ 7.64 (dd, J = 9.4, 1.0 Hz, 2H), 7.48 (t, J = 1.3 Hz, 2H), 7.39 (dd, J = 9.4, 1.5 Hz, 2H), 6.59 (s, 2H), 2.70-2.62 (m, 4H), 1.66 (p, J = 7.5 Hz, 4H), 1.38–1.25 (m, 36H), 0.88 (t, J = 6.8 Hz, 6H). ^{13}C NMR (126 MHz, chloroform-d) δ 149.5, 148.2, 142.1, 136.8, 135.8, 135.2, 133.8, 133.3, 129.7, 125.1, 115.7, 111.3, 96.6, 35.5, 31.9, 31.3, 29.7, 29.6, 29.5, 29.4, 22.7, 14.1 HRMS (EI): m/z calculated for $C_{54}H_{66}N_6O_2$: 830.5247 [$M^{\cdot+}$]; found: 830.5261.

The analogue **2a** was synthesised using the same molar ratio of substrates and the same conditions, starting from *p*-toluidine instead of 4-dodecylaniline. Upon addition of acetonitrile dark orange crystals formed which were purified by recrystallization from mixture of dichloromethane and hexanes. Next, the crystals were taken to X-ray diffraction and optical studies. ^{1}H NMR (500 MHz, chloroform-d) δ 7.65 (d, J = 9.4 Hz, 2H), 7.46 (s, 2H), 7.39 (dd, J = 9.3, 1.5 Hz, 2H), 7.24 (d, J = 2.4 Hz, 8H), 6.56 (s, 2H), 2.41 (s, 6H). HRMS (EI): m/z calculated for $C_{32}H_{22}N_6O_2$: 522.1804 [$M^{\cdot+}$]; found: 522.1797.

2,5-Bis(4-(2,1,3-benzothiadiazolyl))-1,4-bis(4-dodecylphenyl)-1,4-dihydropyrrolo[3,2-*b*]pyrrole (**3**): Glacial acetic acid (2.5 mL), toluene (2.5 mL), benzo[*c*][1,2,5]thiadiazole-4-carbaldehyde (**1d,** 328 mg, 2 mmol, 2 eq.) and 4-dodecylaniline (522 mg, 2 mmol, 2 eq.) were placed in a 50 mL round-bottom flask equipped with a magnetic stir bar. The mixture was reacted at 50°C for 1 h in open flask. After that time, $Fe(ClO_4)_3{\cdot}\times H_2O$ (20 mg, 5 mol$_{\%}$) was added, followed by butane-2,3-dione (87 μL, 1 mmol, 1 eq.). The resulting mixture was stirred at 50°C (oil bath) in an open flask under air overnight. Next, 3 mL of acetonitrile was added and the flask with reaction mixture was moved to the fridge. After 1 hour crude **3** was filtered off, washed with acetonitrile and recrystallized from hot dichloromethane affording 295 mg (42%) of pure product as a yellow solid. M.p. 162−163°C (DCM). ^{1}H NMR (500 MHz, chloroform-d) δ 7.81-7.76 (m, 2H), 7.39 (dd, J = 8.7, 7.1 Hz, 2H), 7.25–7.20 (m, 4H), 7.16 (dd, J = 7.1, 1.0 Hz, 2H), 7.14–7.09 (m, 4H), 7.05 (s, 2H), 2.59 (t, J = 7,7 Hz, 4H), 1.62−1.58 (m, 4H), 1.34−1.28 (m, 10H), 1.26 (m, 26H), 0.88 (t, J = 6.9 Hz, 6H). ^{13}C NMR (126 MHz, chloroform-d) δ 155.5, 153.2, 140.6, 137.8, 133.3, 131.9, 129.3, 129.1, 127.8, 126.6, 125.0, 118.8, 98.5, 35.4, 31.9, 31.3, 29.7, 29.7, 29.6, 29.6, 29.5, 29.4, 29.3, 22.7, 14.1. HRMS (EI): m/z calculated for $C_{54}H_{66}N_6S_2$: 862.4790 [$M^{\cdot+}$]; found: 862.4824.

The analogue **3a** was synthesised using the same molar ratio of substrates and the same conditions, starting from *p*-toluidine instead of 4-dodecylaniline. Upon addition of acetonitrile red crystals formed which were purified by recrystallization from mixture of dichloromethane and hexanes. Next, the crystals were taken to X-ray diffraction and optical studies. ^{1}H NMR (500 MHz, chloroform-d) δ 7.79 (dd, J = 8.8, 1.0 Hz, 2H), 7.40 (dd, J = 8.8, 7.1 Hz, 2H), 7.23–7.20 (m, 4H), 7.15 (dd, J = 7.1, 1.0 Hz, 2H), 7.12 (d, J = 8.0 Hz, 4H), 7.04 (s, 2H), 2.35 (s, 6H). HRMS (EI): m/z calculated for $C_{32}H_{22}N_6S_2$: 554.1347 [$M^{\cdot+}$]; found: 554.1344.

2,5-Bis(5-(2,1,3-benzothiadiazolyl))-1,4-bis(4-dodecylphenyl)-1,4-dihydropyrrolo[3,2-*b*]pyrrole (**4**): Glacial acetic acid (2 mL), toluene (2 mL), benzo[*c*][1,2,5]thiadiazole-5-carbaldehyde (**1e,** 328 mg, 2 mmol, 2 eq.) and 4-dodecylaniline (522 mg, 2 mmol, 2 eq.) were placed in a 50 mL round-bottom flask equipped with a magnetic stir bar. The mixture was reacted at 50°C for 1 h in an open flask. After that time, $Fe(ClO_4)_3{\cdot}{\times}H_2O$ (20 mg, 5 mol$_{\%}$) was added, followed by butane-2,3-dione (87 µL, 1 mmol, 1 eq.). The resulting mixture was stirred at 50°C (oil bath) in an open flask under air for 17 hours. Next, 5 mL of acetonitrile was added and the flask with reaction mixture was moved to the fridge. After 1 hour crude **4** was filtered off, washed with acetonitrile and recrystallized from mixture of dichloromethane and hexanes, affording 392 mg (46%) of pure product as an orange solid. M.p. 137−138°C (DCM/hexanes). ^{1}H NMR (500 MHz, chloroform-d) δ 7.79 (d, J = 8.6 Hz, 4H), 7.53 (d, J = 9.6 Hz, 2H), 7.28−7.18 (m, 8H), 6.60 (s, 2H), 2.64 (t, J = 7,8 Hz, 4H), 1.66−1.62 (m, 4H), 1.34 (d, J = 7.5 Hz, 8H), 1.28 (d, J = 12.1 Hz, 36H), 0.87 (t, J = 6.7 Hz, 6H). ^{13}C NMR (126 MHz, chloroform-d) δ 155.2, 153.7, 141.4, 137.1, 135.2, 134.7, 133.3, 131.1, 129.5, 125.1, 120.6, 118.1, 96.2, 35.5, 31.9, 31.3, 29.7, 29.6, 29.6, 29.5, 29.4, 29.3, 22.7, 14.1. HRMS (EI): m/z calculated for $C_{54}H_{66}N_6S_2$: 862.4790 [$M^{\cdot+}$]; found: 862.4811. X-ray quality crystals were grown by a solvent-evaporation method.

2,5-Bis(4-(2,1,3-benzoselenadiazolyl))-1,4-bis(4-dodecylphenyl)-1,4-dihydropyrrolo[3,2-*b*]pyrrole (**5**): Glacial acetic acid (2mL), toluene (2mL), 4-formyl-2,1,3-benzoselenadiazole (**1f**, 212 mg, 1 mmol, 2 eq.) and 4-dodecylaniline (261 mg, 1 mmol, 2 eq.) were placed in a 50 mL round-bottom flask equipped with a magnetic stir bar. The mixture was reacted at 50°C for 1 h in an open flask. After that time, $Fe(ClO_4)_3{\cdot}{\times}H_2O$ (10 mg, 5 mol$_{\%}$) was added, followed by butane-2,3-dione (44 µL, 0.5 mmol, 1 eq.). The resulting mixture was stirred at 50°C (oil bath) in an open flask under air for 17 hours. Next, 3 mL of acetonitrile was added, but no precipitate was found. The mixture was concentrated using rotary evaporator and from such a crude mixture, dry column vacuum chromatography was conducted, using silica gel and 1:1 dichloromethane / hexanes mixture as eluent. Yield: 19 mg (4%). Dark red solid. M.p. 196−197°C (DCM/hexanes). ^{1}H

NMR (500 MHz, chloroform-d) δ 7.64 (d, J = 8.9 Hz, 2H), 7.30 (dd, J = 8.9, 6.9 Hz, 2H), 7.22 (d, J = 8.1 Hz, 4H), 7.09 (d, J = 8.0 Hz, 4H), 7.05 (d, J = 6.8 Hz, 2H), 6.96 (s, 2H), 2.57 (t, J = 7.7 Hz, 4H), 1.62–1.56 (m, 4H), 1.28 (d, J = 16.8 Hz, 36H), 0.88 (t, J = 6.8 Hz, 6H) ^{13}C NMR (126 MHz, chloroform-d) δ 161.0, 159.0, 140.4, 137.9, 133.0, 132.3, 129.6, 129.0, 128.7, 128.1, 128.1, 124.8, 121.0, 98.6, 35.4, 31.9, 31.4, 29.7, 29.7, 29.6, 29.6, 29.5, 29.4, 29.3, 29.1, 22.7, 14.1. HRMS (EI): m/z calculated for $C_{54}H_{66}N_6Se_2$: 958.3679 [$M^{\cdot+}$]; found: 958.3640. X-ray quality crystals were grown by a solvent-evaporation method.

2,5-Bis(4-(7-nitro-2,1,3-benzoxadiazolyl))-1,4-bis(4-dodecylphenyl)-1,4-dihydropyrrolo[3,2-*b*]pyrrole (**6**): Glacial acetic acid (2 mL), toluene (2 mL), 4-formyl-7-nitro-2,1,3-benzoxadiazole (**1b,** 386 mg, 2 mmol, 2 eq.) and 4-dodecylaniline (522 mg, 2 mmol, 2 eq.) were placed in a 50 mL round-bottom flask equipped with a magnetic stir bar. The mixture was reacted at 50°C for 1 h in an open flask. After that time, $Fe(ClO_4)_3\cdot\times H_2O$ (20 mg, 5 mol$_{\%}$) was added, followed by butane-2,3-dione (87 µL, 1 mmol, 1 eq.). The resulting mixture was stirred at 50°C (oil bath) in an open flask under air for 17 hours. Next, 3 mL of acetonitrile was added which resulted in precipitation of dark blue crystals of **6.** The product was purified on dry column vacuum chromatography, using silica gel and 1:1 dichlormethane/hexanes mixture as eluent. Yield: 225 mg (24%). Dark blue solid. M.p. 188–189°C. ^{1}H NMR (500 MHz, chloroform-d) δ 8.19 (d, J = 8.1 Hz, 2H), 7.43 (s, 2H), 7.39–7.28 (m, 8H), 6.82 (d, J = 8.1 Hz, 2H), 2.80–2.61 (m, 4H), 1.79–1.61 (m, 4H), 1.55 (m, 4H), 1.44–1.18 (m, 36H), 0.88 (t, J = 6.8 Hz, 6H). ^{13}C NMR (126 MHz, chloroform-d) δ 149.0, 143.6, 143.4, 138.6, 136.1, 133.6, 132.4, 130.8, 130.3, 128.8, 125.7, 123.5, 102.6, 35.6, 31.9, 31.3, 29.7, 29.6, 29.6, 29.5, 29.4, 29.3, 22.7, 14.1. HRMS (EI): m/z calculated for $C_{54}H_{64}N_8O_6$: 920.4949 [$M^{\cdot+}$]; found: 920.4951. X-ray quality crystals were grown by a solvent-evaporation method.

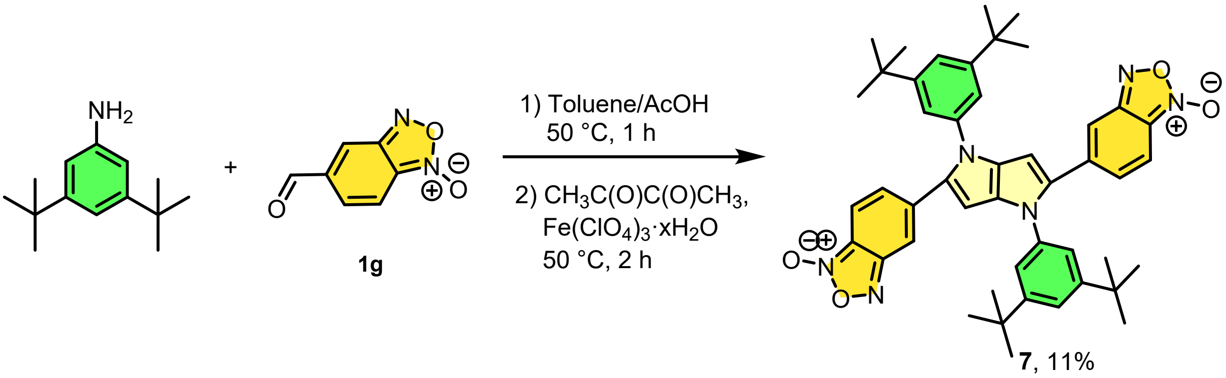

Scheme S2. Synthesis of compound **7**.

5,5'-(1,4-Bis(3,5-di-tert-butylphenyl)-1,4-dihydropyrrolo[3,2-b]pyrrole-2,5-diyl)bis(benzo[c][1,2,5]oxadiazole 1-oxide) (**7**): Glacial acetic acid (2 mL), toluene (2 mL), 6-formylbenzo[*c*][1,2,5]oxadiazole 1-oxide **1g** (2 mmol, 0.328 g), and 3,5-di-*tert*-butylaniline (2 mmol, 0.410 g) were placed in a 25 mL round-bottom flask equipped with a magnetic stir bar. The mixture was stirred at 50 °C for 1 h. After that time, $Fe(ClO_4)_3 \cdot \times H_2O$ (22 mg, 0.06 mmol) was added, followed by diacetyl (88 µL, 1 mmol). The resulting mixture was stirred at 50°C (oil bath) in an open flask under air for 2 hours. After cooling to room temperature, the precipitate was filtered off, washed with cold methanol and diethyl ether, and dried under vacuum affording **7** (83 mg, 11%) as a red solid. The dried product thus obtained showed a single spot on TLC (EtOAc-hexanes 1:2) and was pure enough for all analytical purposes.

For single crystal X-ray analysis: The red long needle-like crystals of compound **7** were obtained from slow diffusion of acetonitrile into the dilute solution of **7** in chloroform (vapor diffusion technique) after 4 days. Red needles; m.p.: 193–194°C (dec.); ^{1}H NMR (500 MHz, chloroform-d) δ 1.28 (s, 36H), 6.53 (s, 2H), 7.08-7.19 (br s, 8H), 7.26–7.36 (br s, 2H), 7.38–7.41 (m, 2H); ^{13}C NMR (151 MHz, chloroform-d) δ 152.8, 152.2, 149.9, 138.1, 134.8, 133.4, 129.0, 128.2, 121.6, 120.7, 119.6, 115.2, 96.3, 35.0, 31.3; HRMS (APCI): *m/z* calculated for $C_{46}H_{50}N_6O_4$: 750.3894 [M$^+$]; found: 750.3900.

For compound **7** there are different spectra than for the remaining compounds due to the conversion of two regioisomeric forms of benzofuroxane moieties into each other, which is a known dynamic phenomenon.[3]

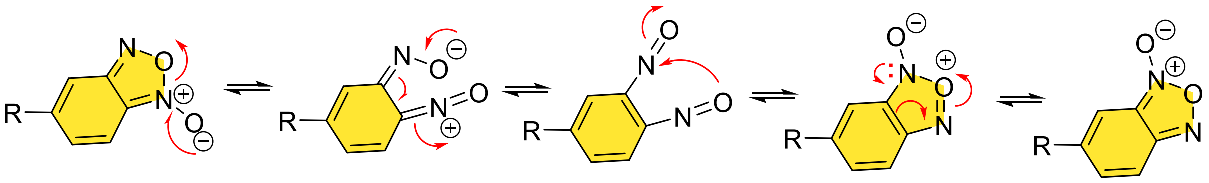

Scheme S3. Delocalization in benzofuroxane moieties, providing equilibrium of two regioisomers.

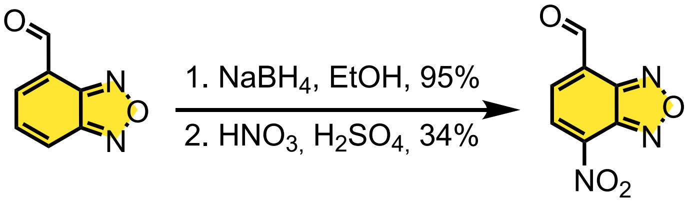

Scheme S4. Synthesis of **1b**.

4-Hydroxymethyl-2,1,3-benzoxadiazole (**S1**) was synthesized following modified literature procedure.[4] 296 mg (2 mmol) of 4-formyl-2,1,3-benzoxadiazole was placed in a 50 mL round-bottom flask equipped with a magnetic stir bar and 10 mL anhydrous ethanol was added. The mixture was cooled down to 0°C (ice bath). Then, 83.6 mg (1.1 eq., 2.2 mmol) of $NaBH_4$ was added in one portion. Colour of the mixture has changed from pale yellow to purple. The reaction process was being checked by TLC. After 1 hour a full conversion was observed, and aqueous solution of ammonium acetate was added, followed by 2 M $HCl_{(aq)}$. Product was extracted with dichloromethane, organic layer was separated, dried over anhydrous Na_2SO_4 and the solvent was evaporated under reduced pressure. Yellow solid of 4-hydroxymethyl-2,1,3-benzoxadiazole was obtained (282 mg, 95% yield) and it was used in following steps without further purification. This reaction was then repeated starting from 2 g of 4-formyl-2,1,3-benzoxadiazole, which resulted in the same percentage yield. ^1H NMR (500 MHz, DMSO-d_6) δ 7.90 (d, J = 9.0 Hz, 1H), 7.61 (dd, J = 9.0, 6.5 Hz, 1H), 7.55–7.51 (m, 1H), 7.31–7.07 (m, 1H), 4.89 (s, 2H).

4-Formyl-7-nitro-2,1,3-benzoxadiazole (**1b**) was synthesised following modified literature procedure.[4] 264 mg (1.76 mmol) of 4-hydroxymethyl-2,1,3-benzoxadiazole was dissolved in 1 mL 98% $H_2SO_{4(aq)}$ and cooled down to 0°C (ice bath). Nitration mixture (160 µL HNO_3 and 210 µL H_2SO_4) was added dropwise. Ice bath was then removed and solution was stirred in ambient temperature for 90 min. During that time, reaction mixture changed colour from yellow to dark orange. The mixture was transferred to beaker with water and ice, which resulted in precipitation of yellow solid, filtered off under reduced pressure. The precipitation was washed several times using water, until the pH of the filtrate raised to 7. Obtained precipitate was then purified on dry column vacuum chromatography, using dichloromethane as eluent, then gradually mixing it with methanol, up to 2% methanol in dichloromethane. Synthesis was then repeated starting from 1 g of 4-hydroxymethyl-2,1,3-benzoxadiazole. Instead of pouring the reaction mixture into the beaker with ice, water was added to the mixture and extraction with ethyl acetate was conducted. Estimated yield: 436 mg (34%). Dark yellow solid. The presence of an aldehyde as the only visible compound was confirmed by Brady's test on TLC plate. **1b** was used as crude for the next step.

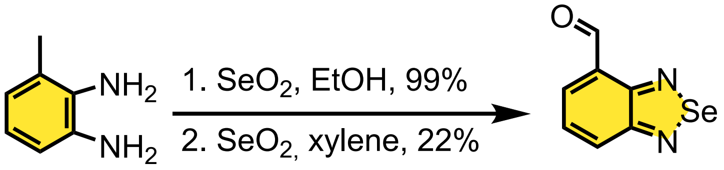

Scheme S5. Synthesis of **1f**.

4-Methyl-2,1,3-benzoselenadiazole (**S2**) was synthesized following modified literature procedure.[5] 3 g (24.5 mmol) of 2,3-diaminotoluene was placed in a 100 mL round-bottom flask equipped with a magnetic stir bar and 30 mL anhydrous ethanol was added. Then, 3 g (1.1 eq., 27 mmol) of SeO_2 was added in one portion. The reaction mixture was refluxed for 30 minutes. After completion of the reaction (checked by TLC), product was extracted with dichloromethane, organic layer was separated, dried over anhydrous Na_2SO_4 and the solvent was evaporated under reduced pressure. Off-white solid of 4-methyl-2,1,3-benzoselenadiazole was obtained with almost quantitative amount (4.82 g, 99% yield) and it was used in following steps without further purification.

4-Formyl-2,1,3-benzselenadiazole (**1f**) was synthesised following modified literature procedure.[6] 1 g (5 mmol) of 4-methyl-2,1,3-benzoselenadiazole was dissolved in 30 mL of anhydrous *m*-xylene and three drops of water were added. Then, 800 mg (1.4 eq., 7 mmol) of SeO_2 was added and the reaction mixture was refluxed for 6 hours. The selenium precipitate was filtered off. From the supernatant, the organic layer was extracted using dichloromethane. Then, the crude was purified by dry vacuum column chromatography using 1:1 dichloromethane/hexanes mixture as eluent. Yield: 230 mg (22%). Dark yellow solid. The presence of an aldehyde as the only visible compound was confirmed by Brady's test on TLC plate. **1f** was used as crude for the next step.

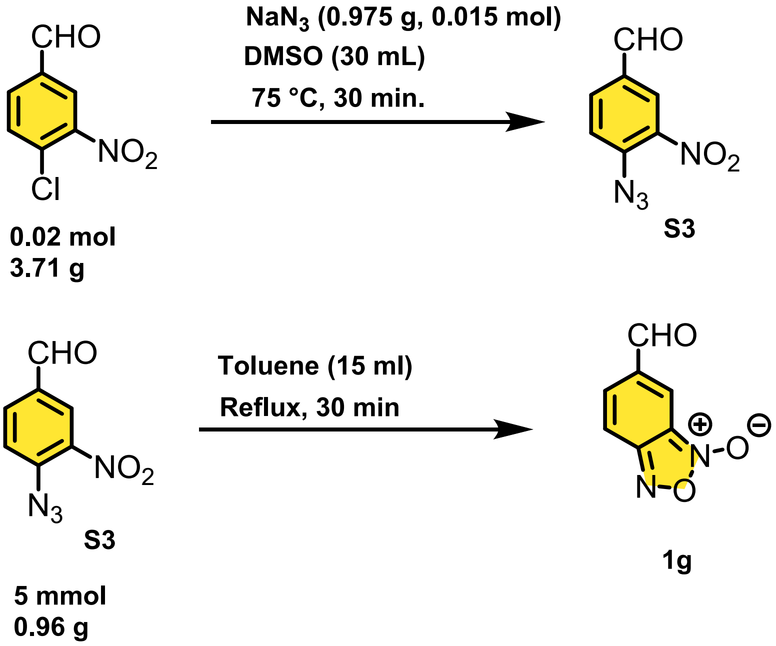

Scheme S6. A two-step synthesis of aldehyde **1g** according to the literature.[7]

6-Formylbenzo[*c*][1,2,5]oxadiazole 1-oxide (**1g**): A mixture of 4-chloro-3-nitrobenzaldehyde (3.71 g, 0.020 mol) and sodium azide (0.975 g, 0.015 mol) in 30.0 mL of dimethylsulfoxide was heated at 75°C during 30 min. The solution was cooled, poured into 100 mL of water, and extracted with ether. After drying with $MgSO_4$ and evaporating the solvent a yellow oil, which solidified at 0°C, was obtained. It was crystallized from ethanol to give 4-azido-3-nitrobenzaldehyde **S3**. Pale yellow plates (75%); m.p. 74–75°C. The azide **S3** (5 mmol) was refluxed for 30 min in 15 mL of toluene. The solvent was evaporated and the remaining oil was redissolved in 5.0 mL of boiling EtOAc. Petroleum ether (b.p. 60–80°C) (20.0 mL) was added and the solution was cooled to give **1g** (80%).

2. ^{1}H and ^{13}C NMR spectra for synthesised compounds

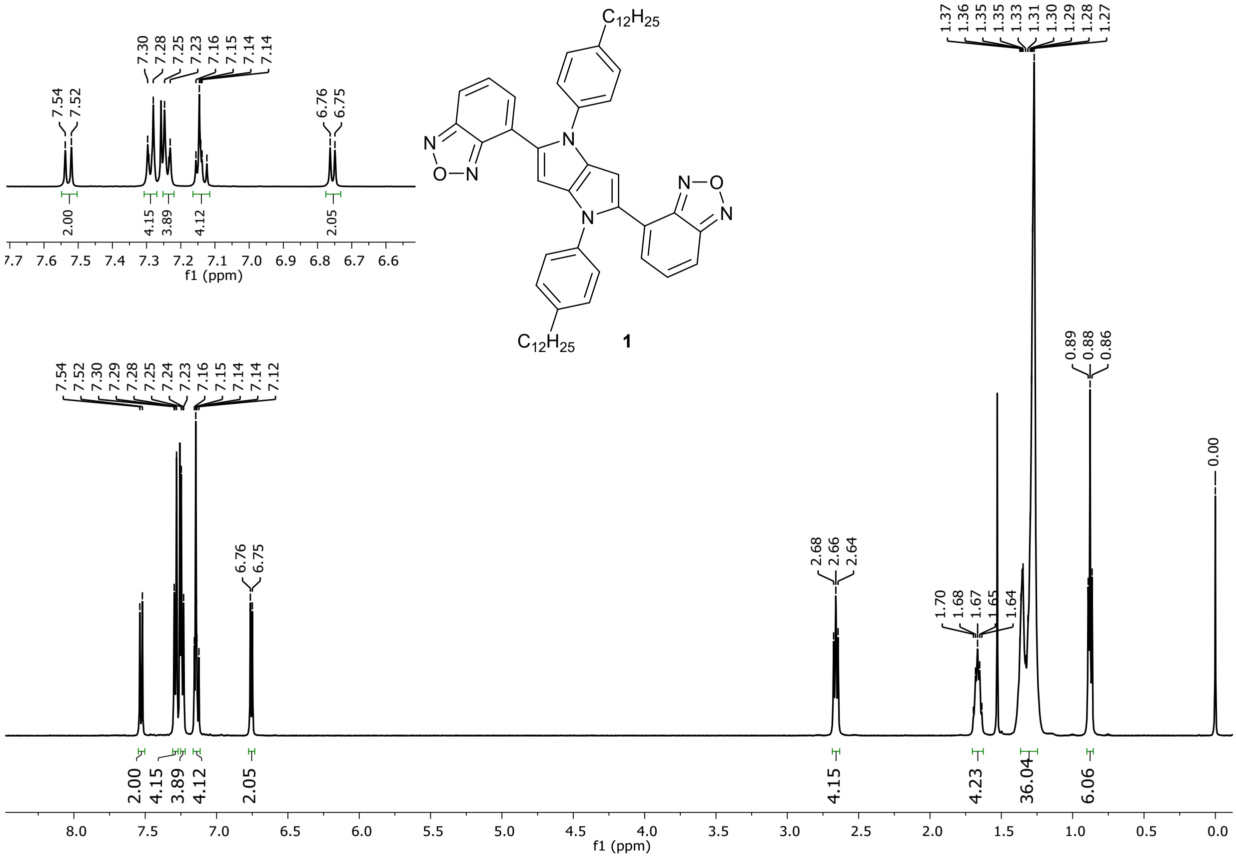

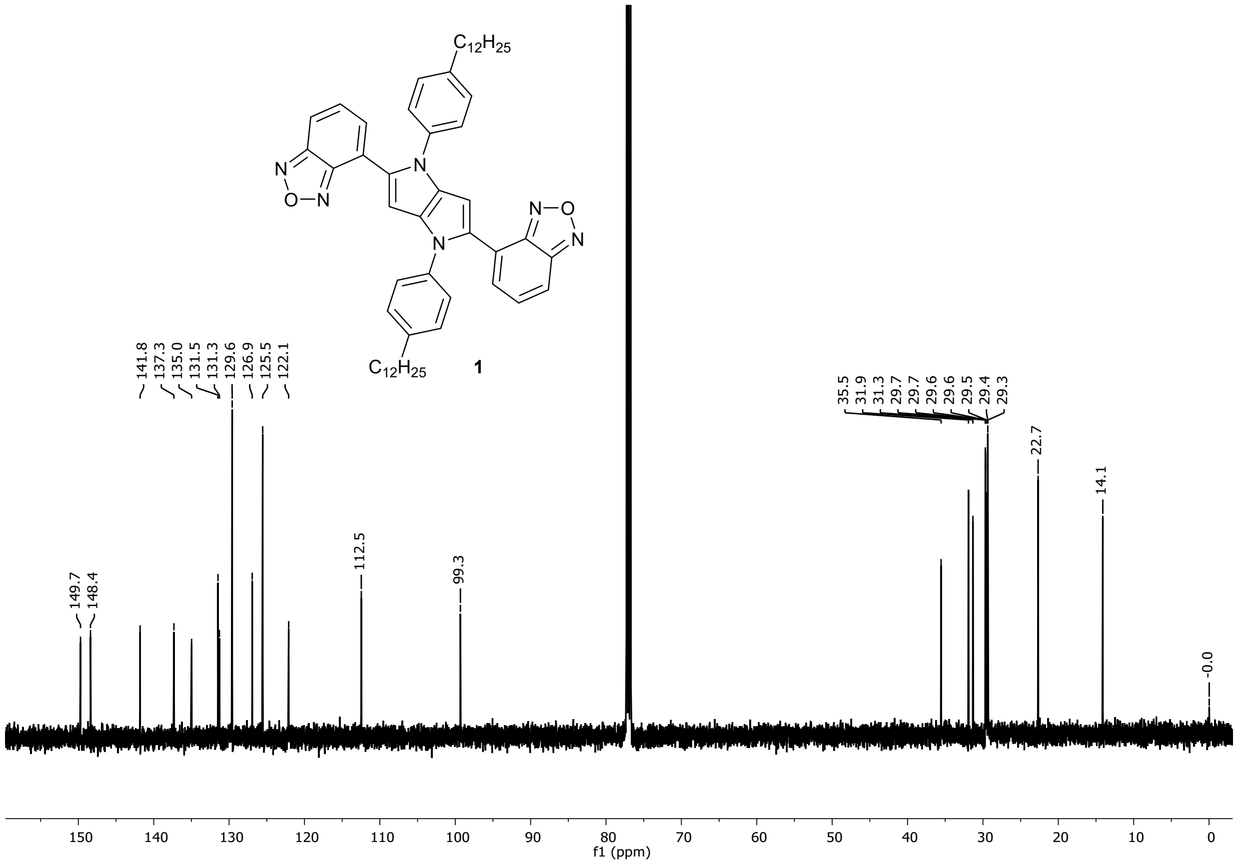

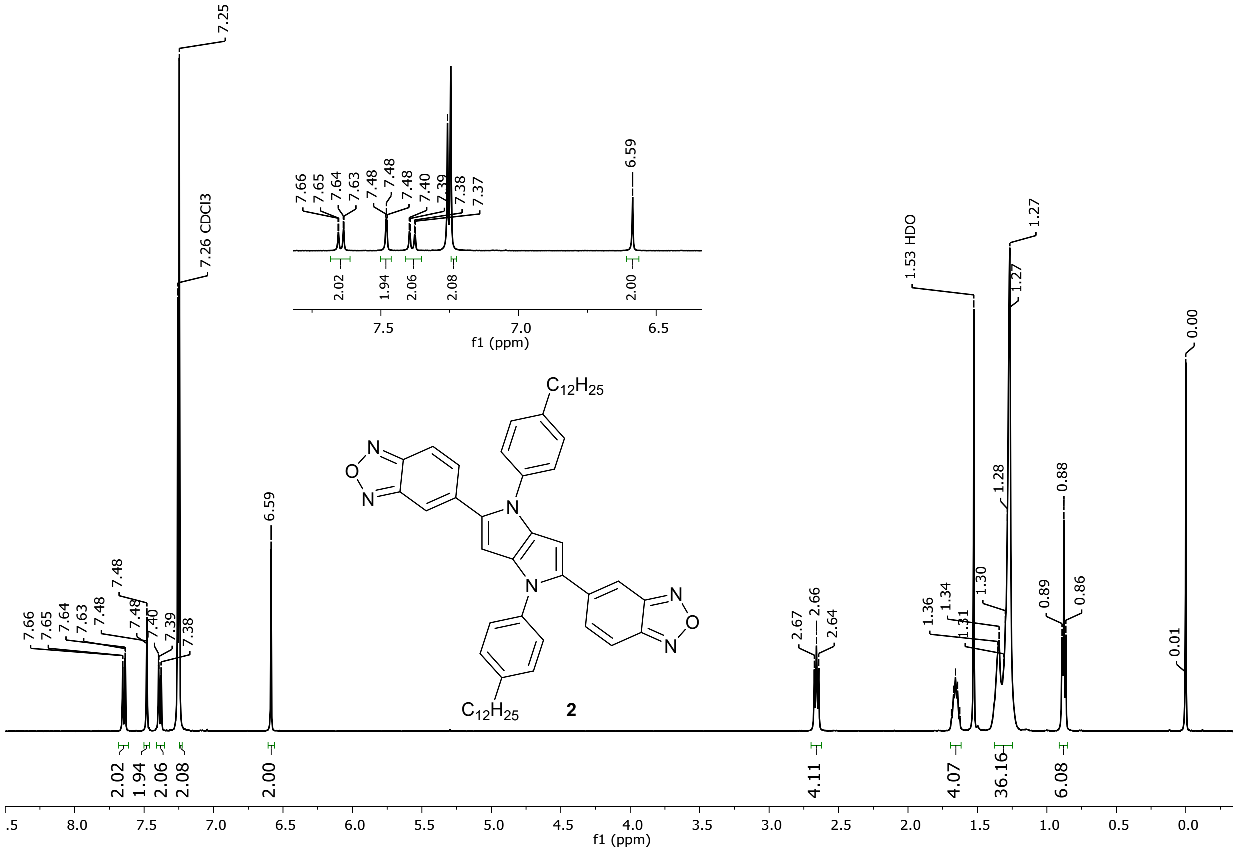
7.66
7.65
7.64
7.63
7.48
7.48
7.48
7.40
7.39
7.38
7.37
7.25
7.26 CDCl3
6.59
2.67
2.66
2.64
1.36
1.34
1.31
1.30
1.28
1.27
1.27
1.53 HDO
0.89
0.88
0.86
0.01
0.00
2.02
1.94
2.06
2.08
2.00
4.11
4.07
36.16
6.08
f1 (ppm)
C12H25
N
O
2

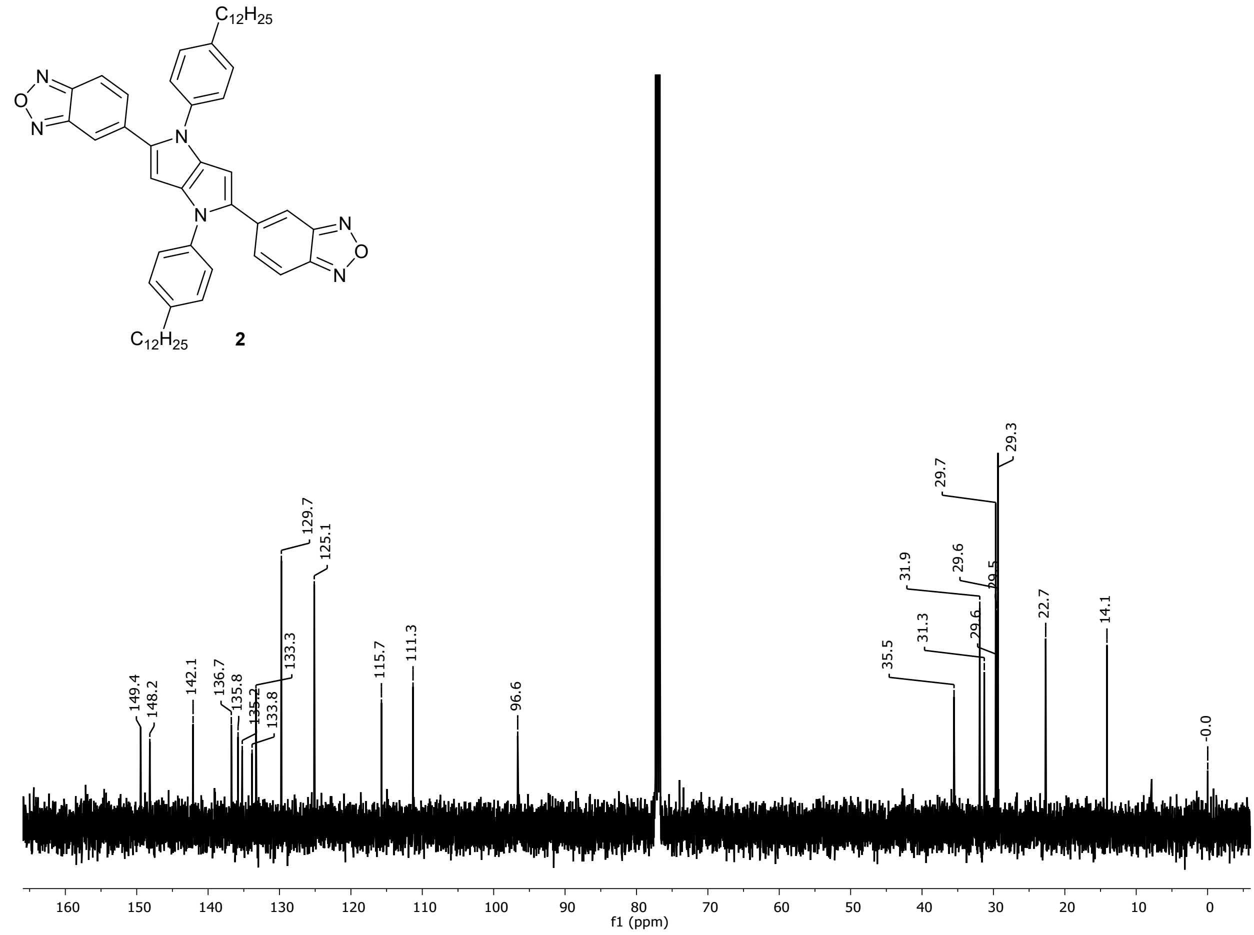
149.4
148.2
142.1
136.7
135.8
135.2
133.8
133.3
129.7
125.1
115.7
111.3
96.6
35.5
31.9
31.3
29.7
29.6
29.6
29.5
29.3
22.7
14.1
-0.0
f1 (ppm)
C12H25
N
O
2

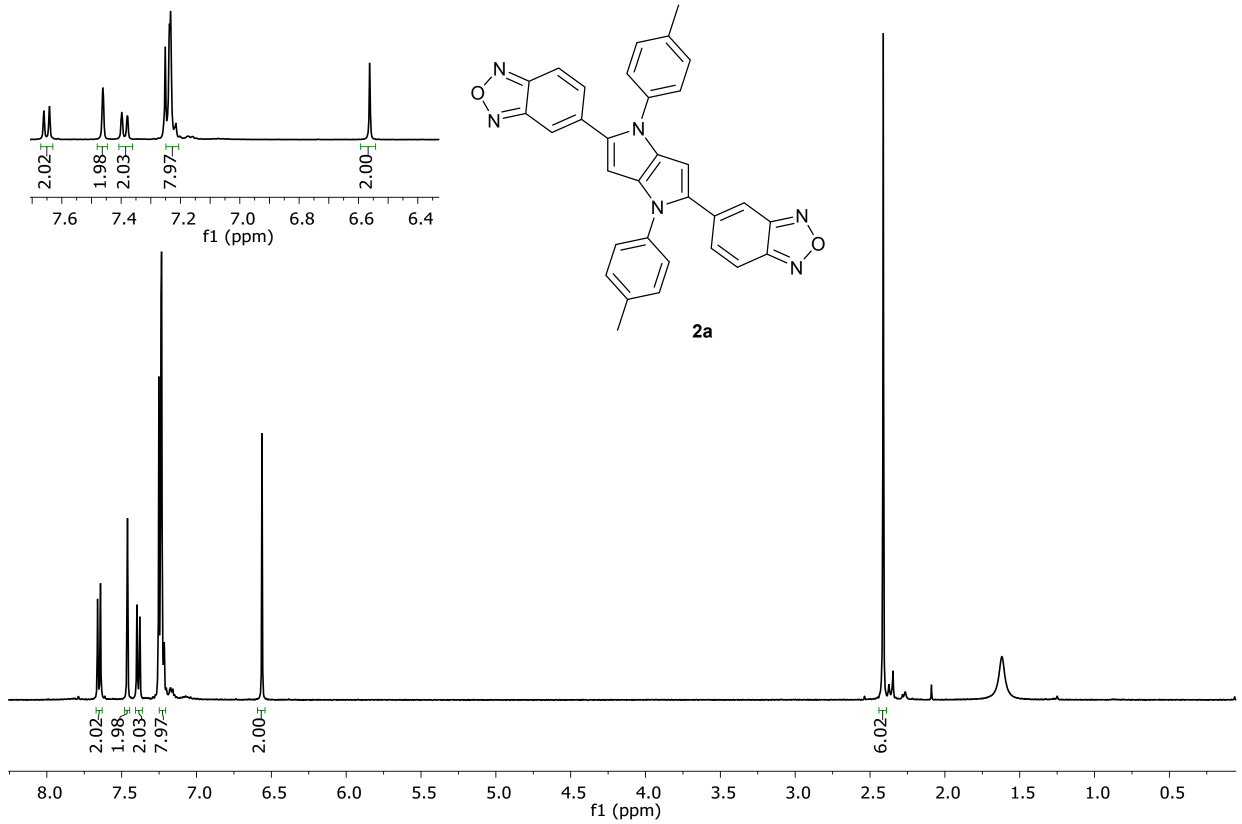
2.02
1.98
2.03
7.97
2.00
7.6 7.4 7.2 7.0 6.8 6.6 6.4
f1 (ppm)
N
O
N
N
N
N
O
N
2.02
1.98
2.03
7.97
2.00
6.02
8.0 7.5 7.0 6.5 6.0 5.5 5.0 4.5 4.0 3.5 3.0 2.5 2.0 1.5 1.0 0.5
f1 (ppm)

2a

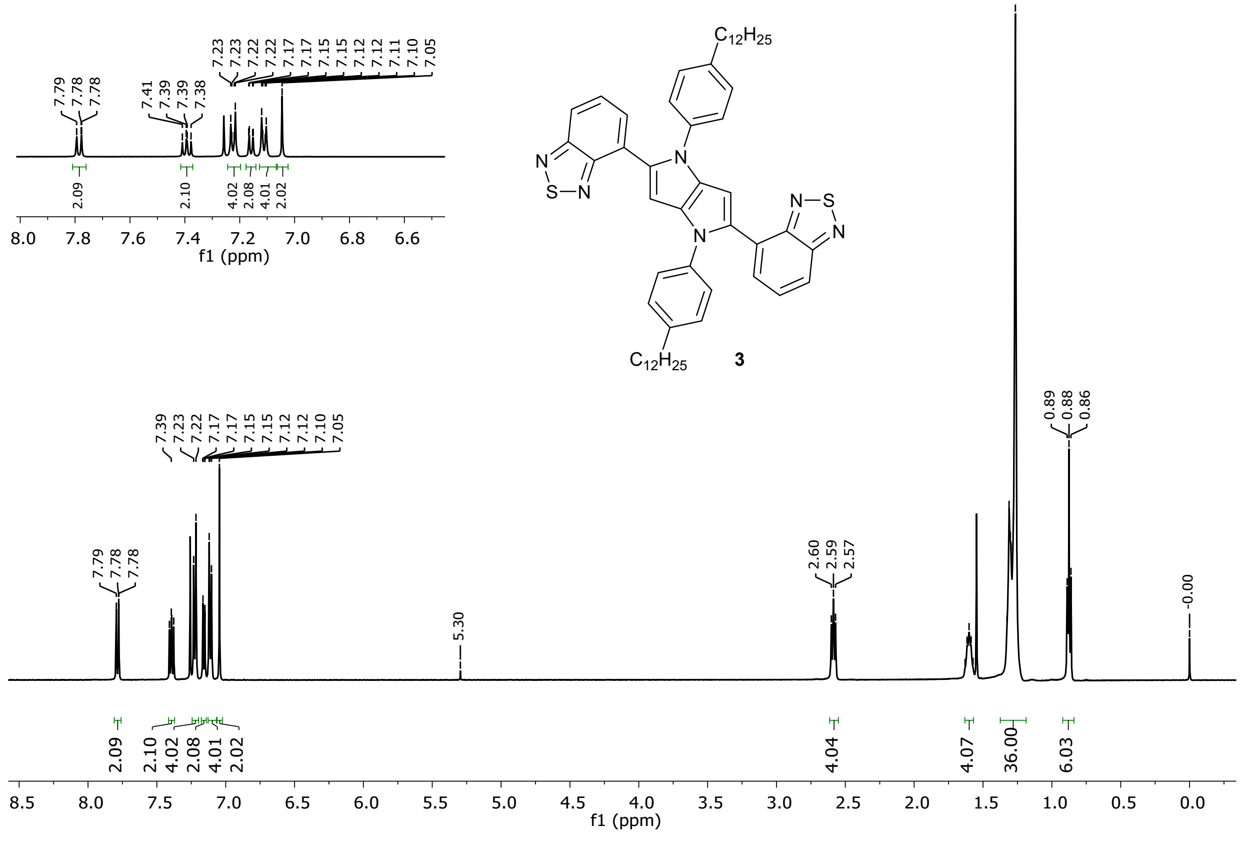
7.79
7.78
7.78
7.41
7.39
7.39
7.38
7.23
7.23
7.22
7.22
7.22
7.17
7.17
7.15
7.15
7.12
7.12
7.11
7.10
7.05
2.09
2.10
4.02
2.08
4.01
2.02
8.0 7.8 7.6 7.4 7.2 7.0 6.8 6.6
f1 (ppm)
$C_{12}H_{25}$
N
S
N
N
N
N
S
N
$C_{12}H_{25}$
7.39
7.23
7.22
7.17
7.17
7.15
7.15
7.12
7.12
7.10
7.05
7.79
7.78
7.78
5.30
2.60
2.59
2.57
0.89
0.88
0.86
-0.00
2.09
2.10
4.02
2.08
4.01
2.02
4.04
4.07
36.00
6.03
8.5 8.0 7.5 7.0 6.5 6.0 5.5 5.0 4.5 4.0 3.5 3.0 2.5 2.0 1.5 1.0 0.5 0.0
f1 (ppm)

3

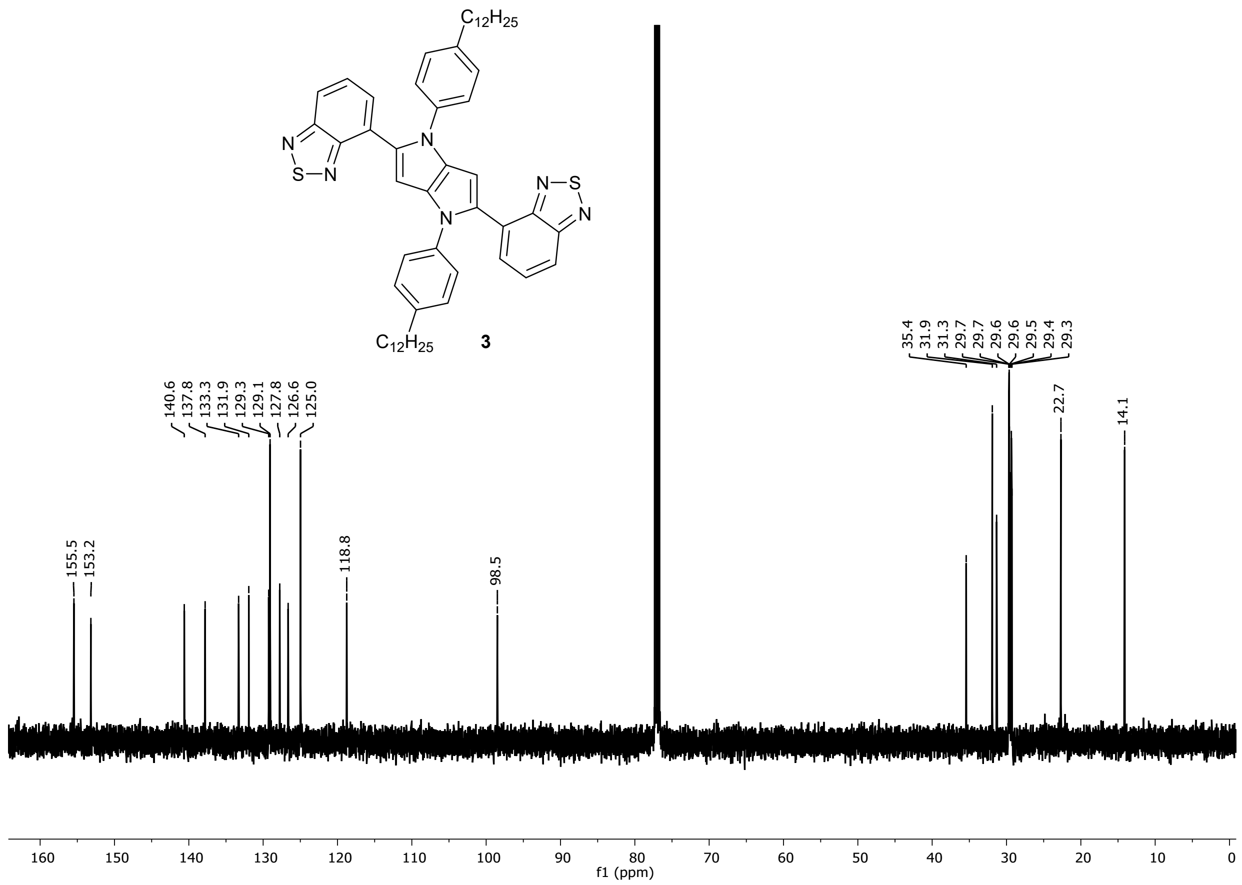

$C_{12}H_{25}$
N
S–N
N–S
$C_{12}H_{25}$
3
155.5
153.2
140.6
137.8
133.3
131.9
129.3
129.1
127.8
126.6
125.0
118.8
98.5
35.4
31.9
31.3
29.7
29.7
29.6
29.6
29.5
29.4
29.3
22.7
14.1
160 150 140 130 120 110 100 90 80 70 60 50 40 30 20 10 0
f1 (ppm)

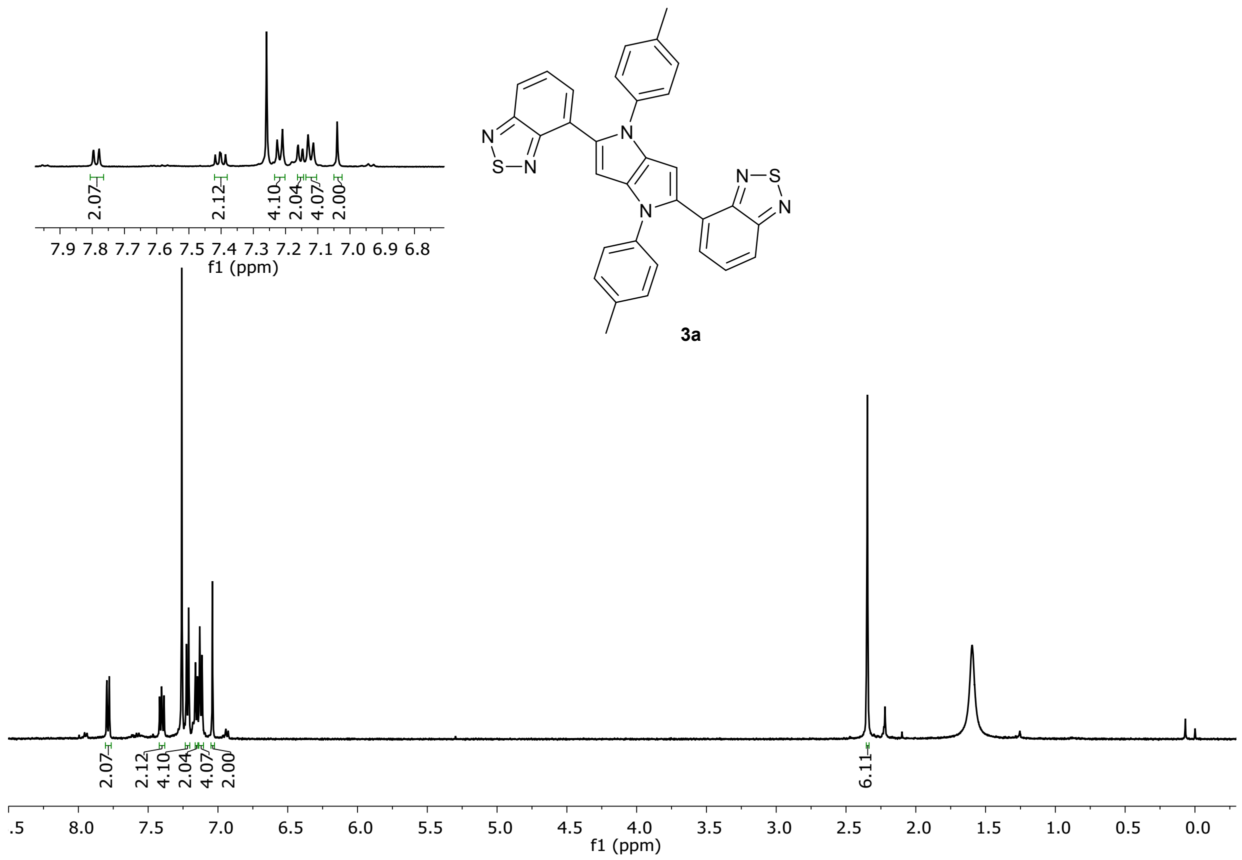

2.07
2.12
4.10
2.04
4.07
2.00
7.9 7.8 7.7 7.6 7.5 7.4 7.3 7.2 7.1 7.0 6.9 6.8
f1 (ppm)
N
S–N
N–S
3a
2.07
2.12
4.10
2.04
4.07
2.00
6.11
.5 8.0 7.5 7.0 6.5 6.0 5.5 5.0 4.5 4.0 3.5 3.0 2.5 2.0 1.5 1.0 0.5 0.0
f1 (ppm)

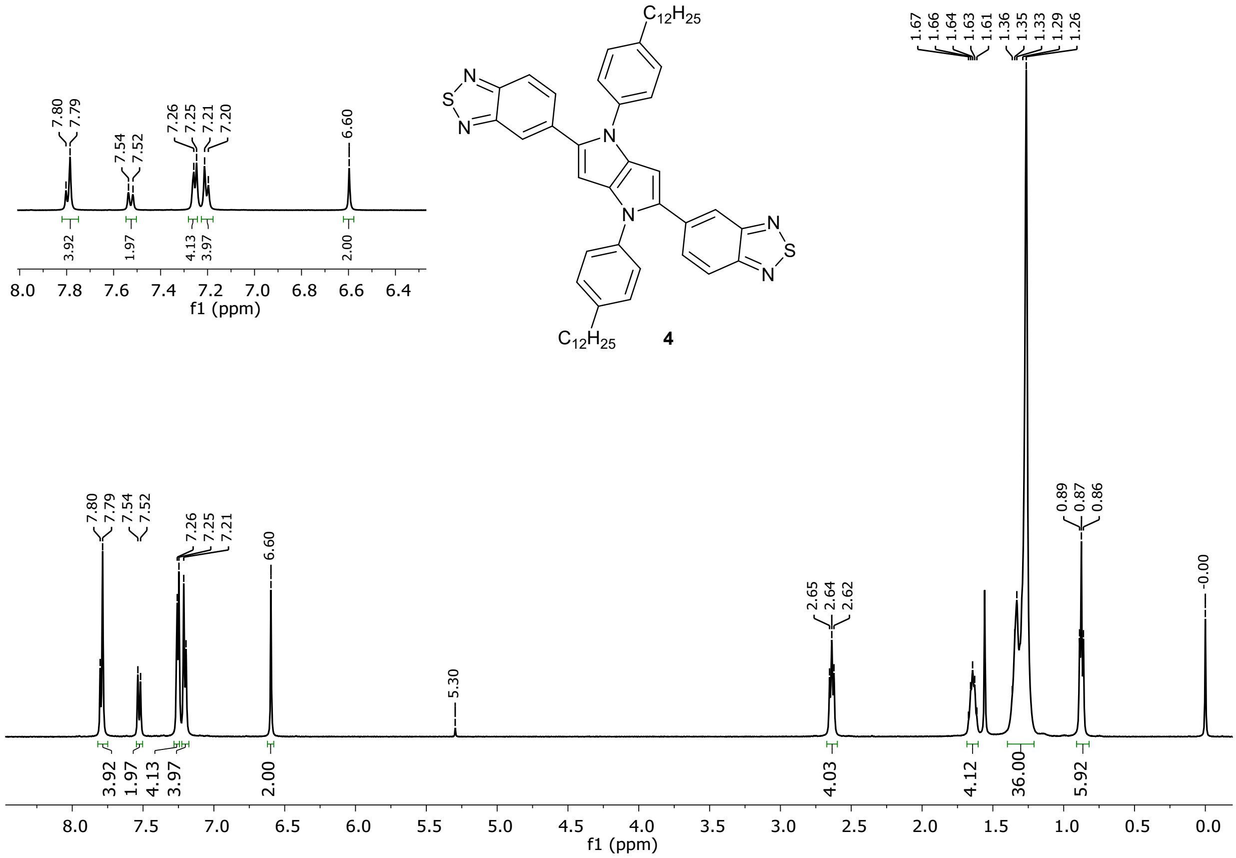
7.80
7.79
7.54
7.52
7.26
7.25
7.21
7.20
6.60
3.92
1.97
4.13
3.97
2.00
8.0 7.8 7.6 7.4 7.2 7.0 6.8 6.6 6.4
f1 (ppm)
$C_{12}H_{25}$
N
S
N
N
N
N
S
N
$C_{12}H_{25}$
1.67
1.66
1.64
1.63
1.61
1.36
1.35
1.33
1.29
1.26
0.89
0.87
0.86
-0.00
5.30
2.65
2.64
2.62
4.03
4.12
36.00
5.92
8.0 7.5 7.0 6.5 6.0 5.5 5.0 4.5 4.0 3.5 3.0 2.5 2.0 1.5 1.0 0.5 0.0
f1 (ppm)

4

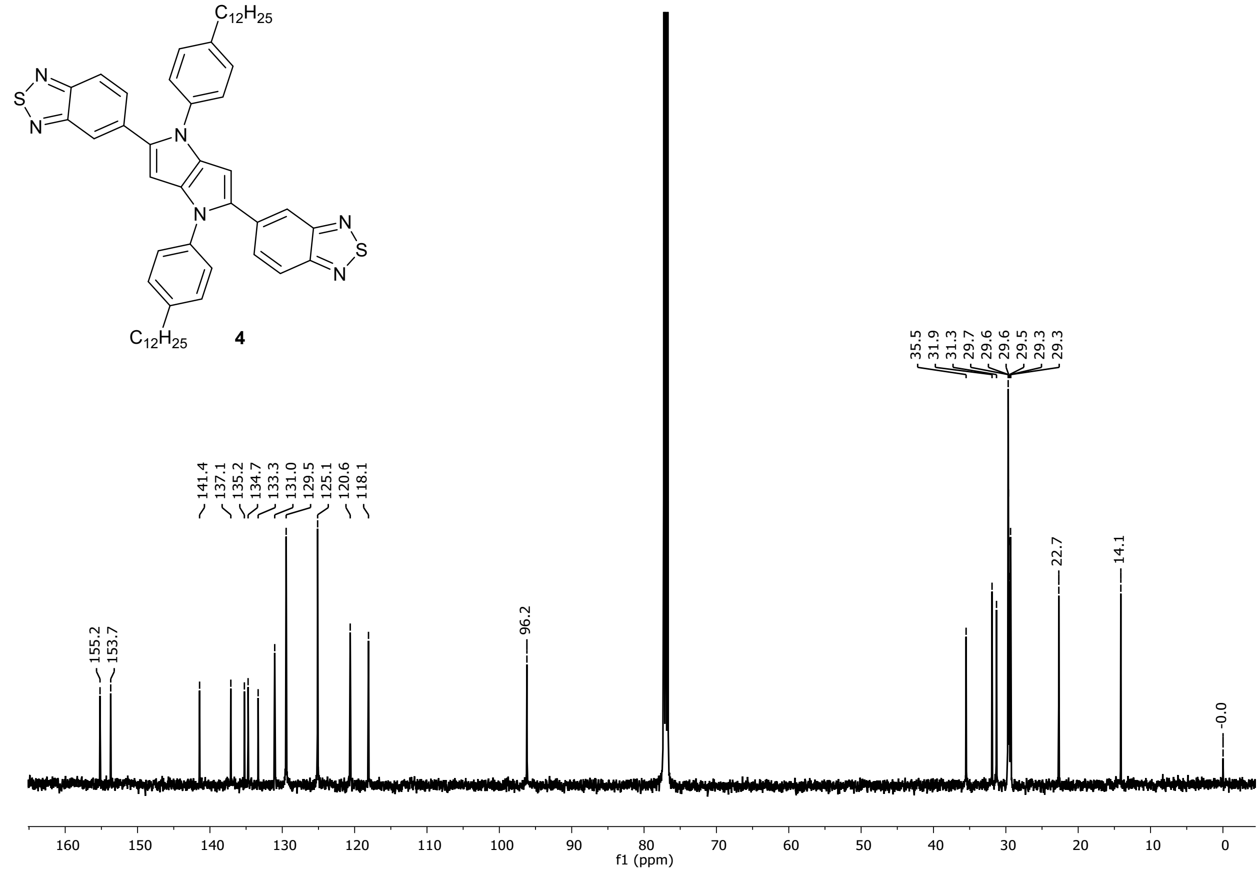
$C_{12}H_{25}$
N
S
N
N
N
N
S
N
$C_{12}H_{25}$
35.5
31.9
31.3
29.7
29.6
29.6
29.5
29.3
29.3
141.4
137.1
135.2
134.7
133.3
131.0
129.5
125.1
120.6
118.1
22.7
14.1
96.2
155.2
153.7
-0.0
160 150 140 130 120 110 100 90 80 70 60 50 40 30 20 10 0
f1 (ppm)

4

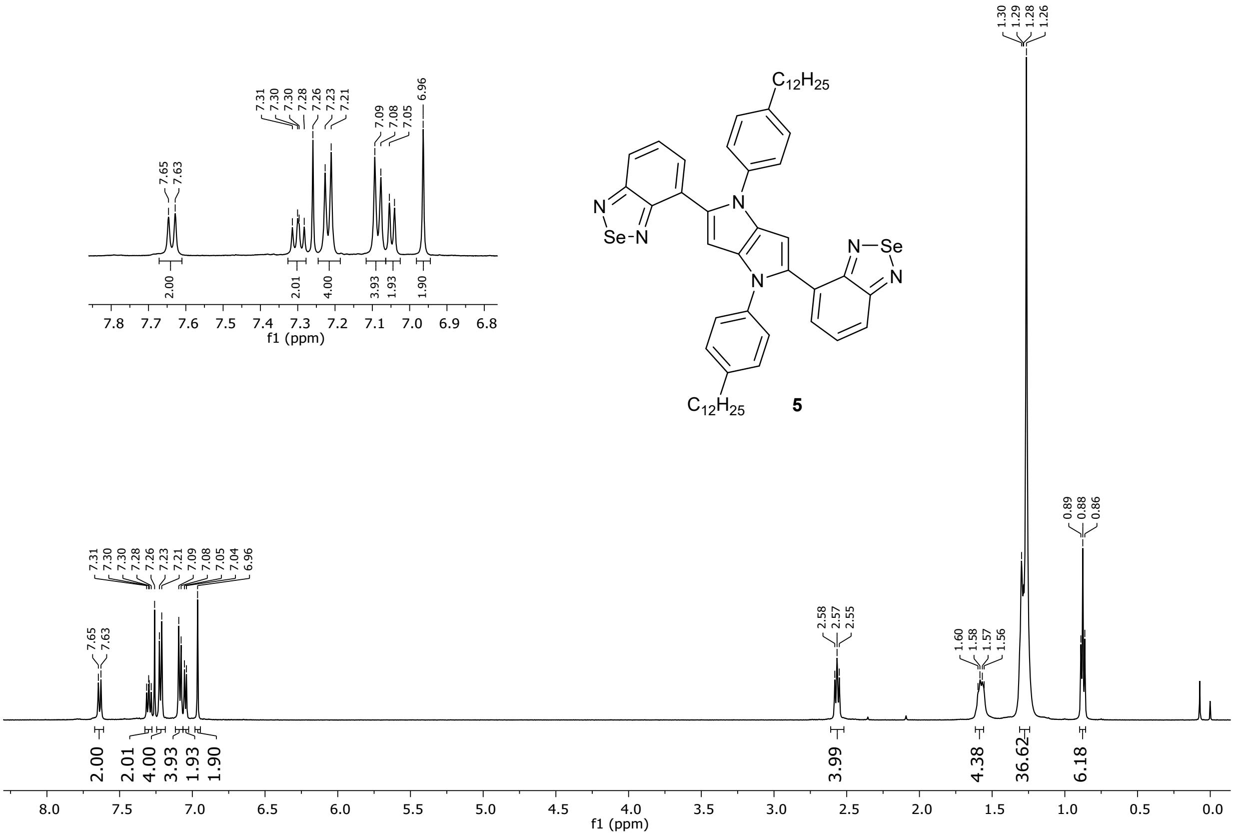
C12H25
N
Se-N
N
N
N-Se
N
C12H25
5
7.65
7.63
7.31
7.30
7.30
7.28
7.26
7.23
7.21
7.09
7.08
7.05
7.04
6.96
2.58
2.57
2.55
1.60
1.58
1.57
1.56
1.30
1.29
1.28
1.26
0.89
0.88
0.86
2.00
2.01
4.00
3.93
1.93
1.90
3.99
4.38
36.62
6.18
7.8 7.7 7.6 7.5 7.4 7.3 7.2 7.1 7.0 6.9 6.8
8.0 7.5 7.0 6.5 6.0 5.5 5.0 4.5 4.0 3.5 3.0 2.5 2.0 1.5 1.0 0.5 0.0
f1 (ppm)

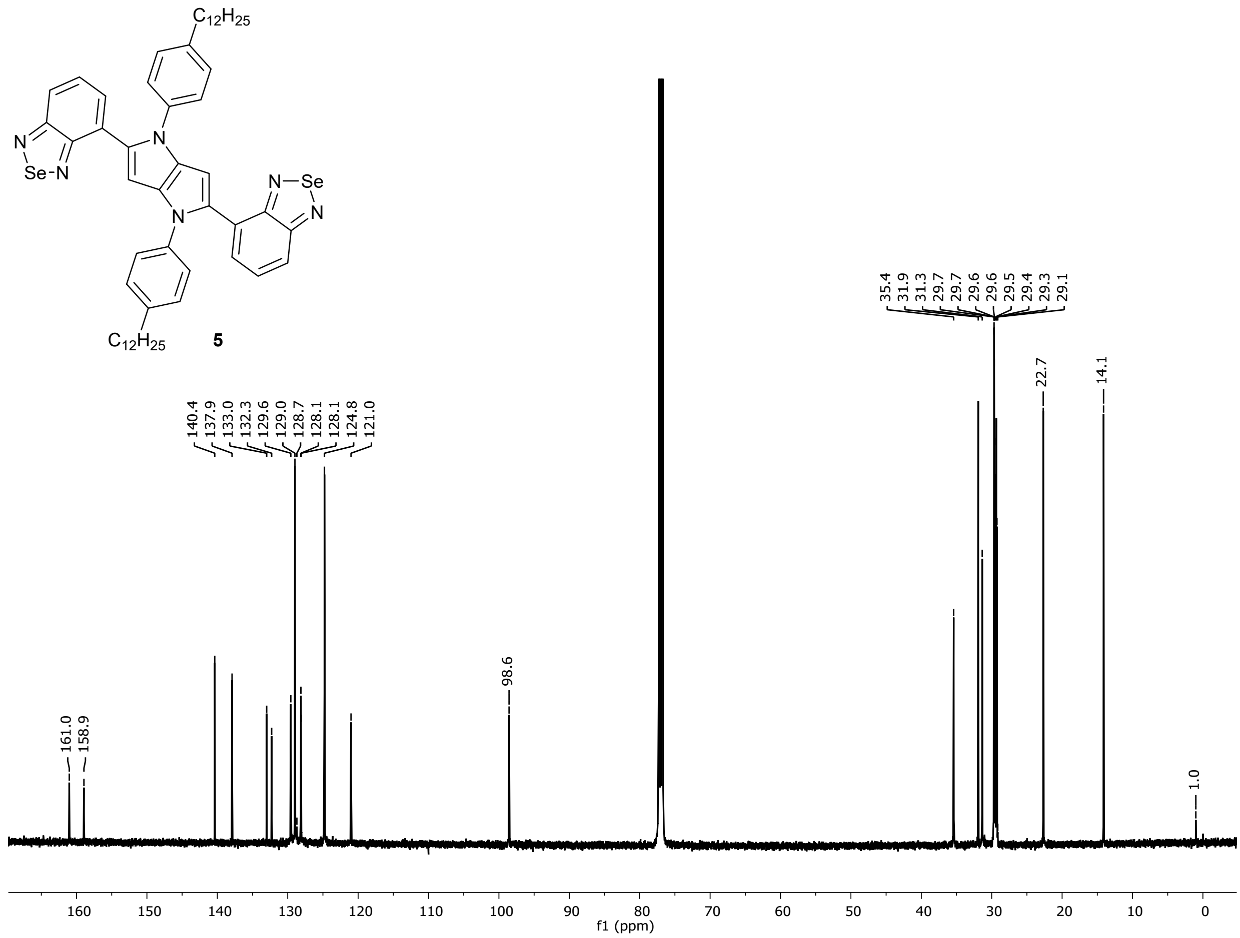
C12H25
N
Se-N
N
N
N-Se
N
C12H25
5
161.0
158.9
140.4
137.9
133.0
132.3
129.6
129.0
128.7
128.1
128.1
124.8
121.0
98.6
35.4
31.9
31.3
29.7
29.7
29.6
29.6
29.5
29.4
29.3
29.1
22.7
14.1
1.0
160 150 140 130 120 110 100 90 80 70 60 50 40 30 20 10 0
f1 (ppm)

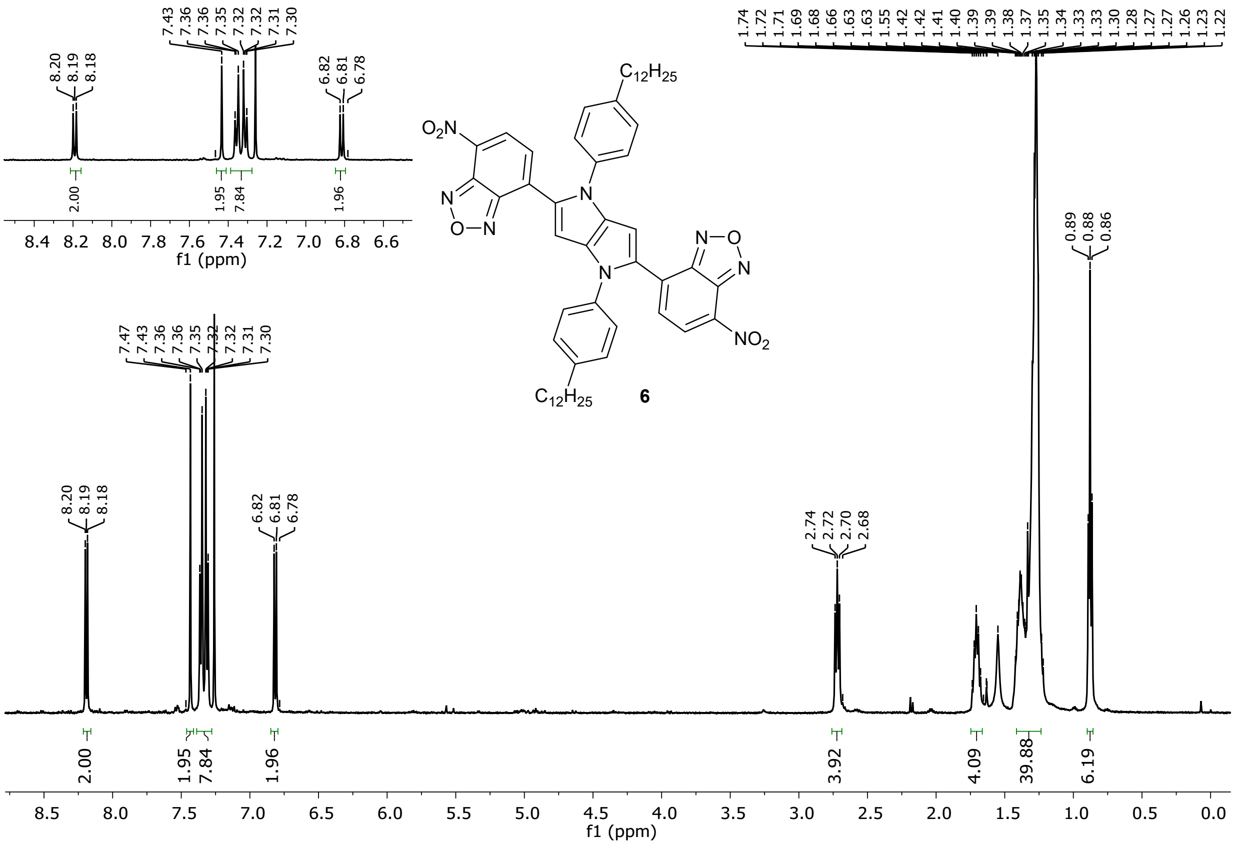
8.20
8.19
8.18
7.43
7.36
7.36
7.35
7.32
7.32
7.31
7.30
6.82
6.81
6.78
2.00
1.95
7.84
1.96
8.4 8.2 8.0 7.8 7.6 7.4 7.2 7.0 6.8 6.6
f1 (ppm)
$C_{12}H_{25}$
O_2N
N
O
N
N
N
N
O
N
NO_2
$C_{12}H_{25}$
6
1.74
1.72
1.71
1.69
1.68
1.66
1.63
1.63
1.55
1.42
1.42
1.41
1.40
1.39
1.39
1.38
1.37
1.35
1.34
1.33
1.33
1.30
1.28
1.27
1.26
1.23
1.22
0.89
0.88
0.86
7.47
7.43
7.36
7.36
7.35
7.32
7.32
7.31
7.30
8.20
8.19
8.18
6.82
6.81
6.78
2.74
2.72
2.70
2.68
2.00
1.95
7.84
1.96
3.92
4.09
39.88
6.19
8.5 8.0 7.5 7.0 6.5 6.0 5.5 5.0 4.5 4.0 3.5 3.0 2.5 2.0 1.5 1.0 0.5 0.0
f1 (ppm)

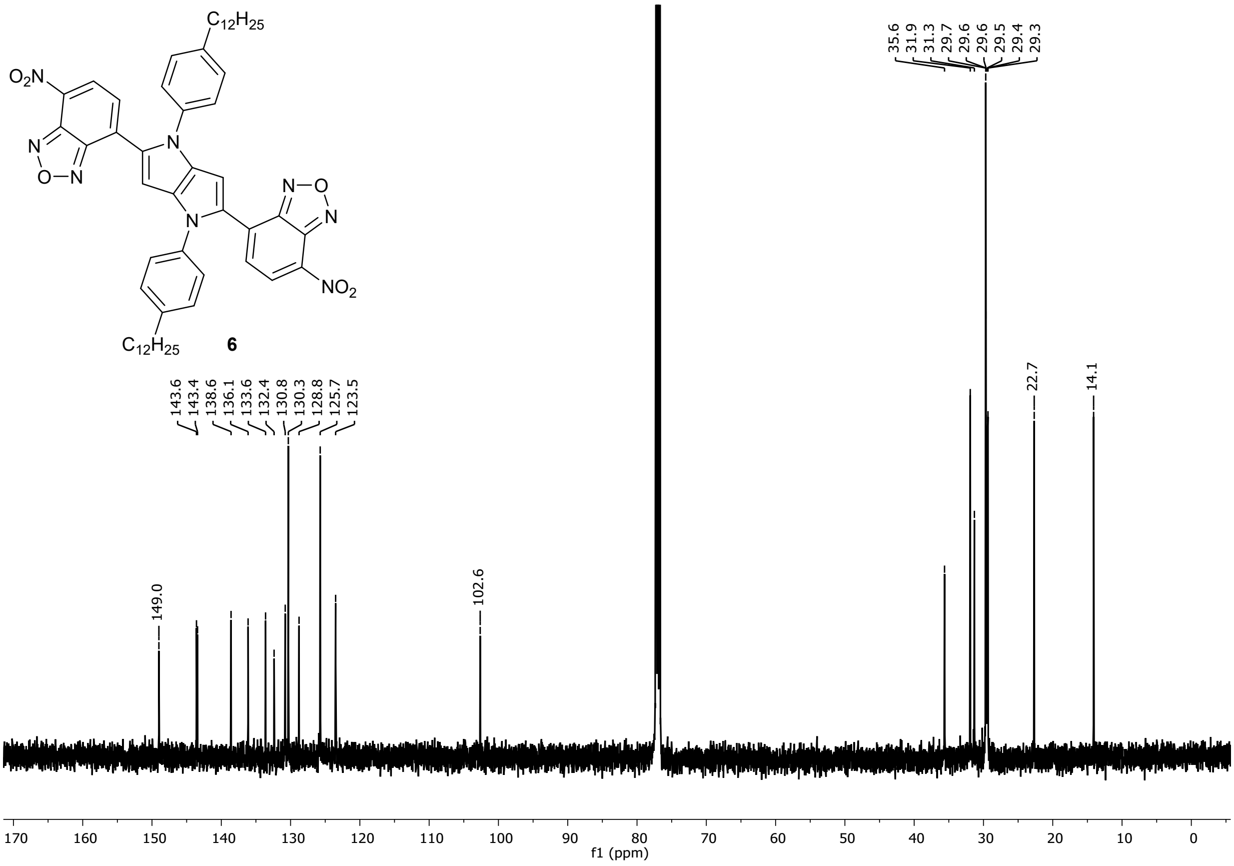
$C_{12}H_{25}$
O_2N
N
O
N
N
N
N
O
N
NO_2
$C_{12}H_{25}$
6
35.6
31.9
31.3
29.7
29.6
29.6
29.5
29.4
29.3
22.7
14.1
143.6
143.4
138.6
136.1
133.6
132.4
130.8
130.3
128.8
125.7
123.5
149.0
102.6
170 160 150 140 130 120 110 100 90 80 70 60 50 40 30 20 10 0
f1 (ppm)

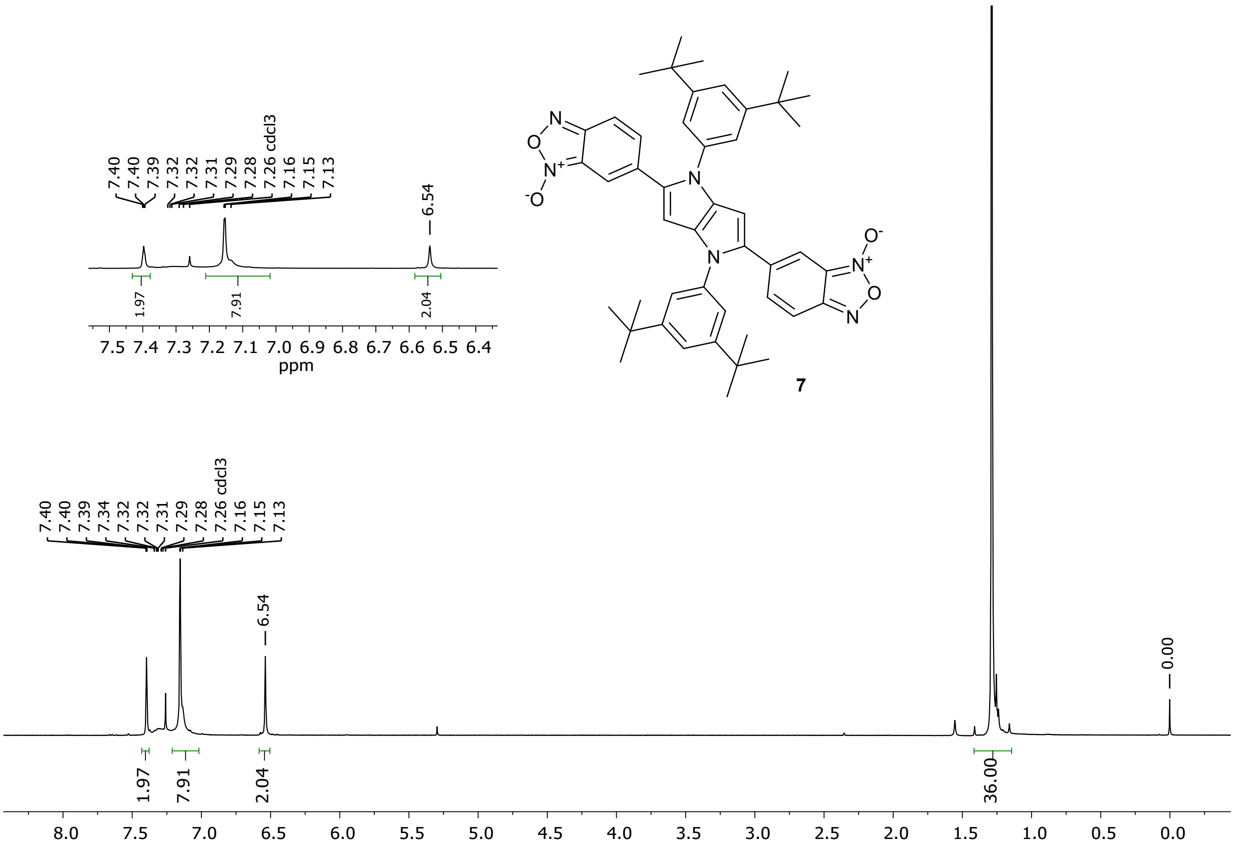
7.40
7.40
7.39
7.32
7.32
7.31
7.29
7.28
7.26 cdcl3
7.16
7.15
7.13
6.54
1.97
7.91
2.04
7.5 7.4 7.3 7.2 7.1 7.0 6.9 6.8 6.7 6.6 6.5 6.4
ppm
N
O
N+
O-
N
N
O-
N+
O
N
7.40
7.40
7.39
7.34
7.32
7.32
7.31
7.29
7.28
7.26 cdcl3
7.16
7.15
7.13
6.54
0.00
1.97
7.91
2.04
36.00
8.0 7.5 7.0 6.5 6.0 5.5 5.0 4.5 4.0 3.5 3.0 2.5 2.0 1.5 1.0 0.5 0.0
ppm

7

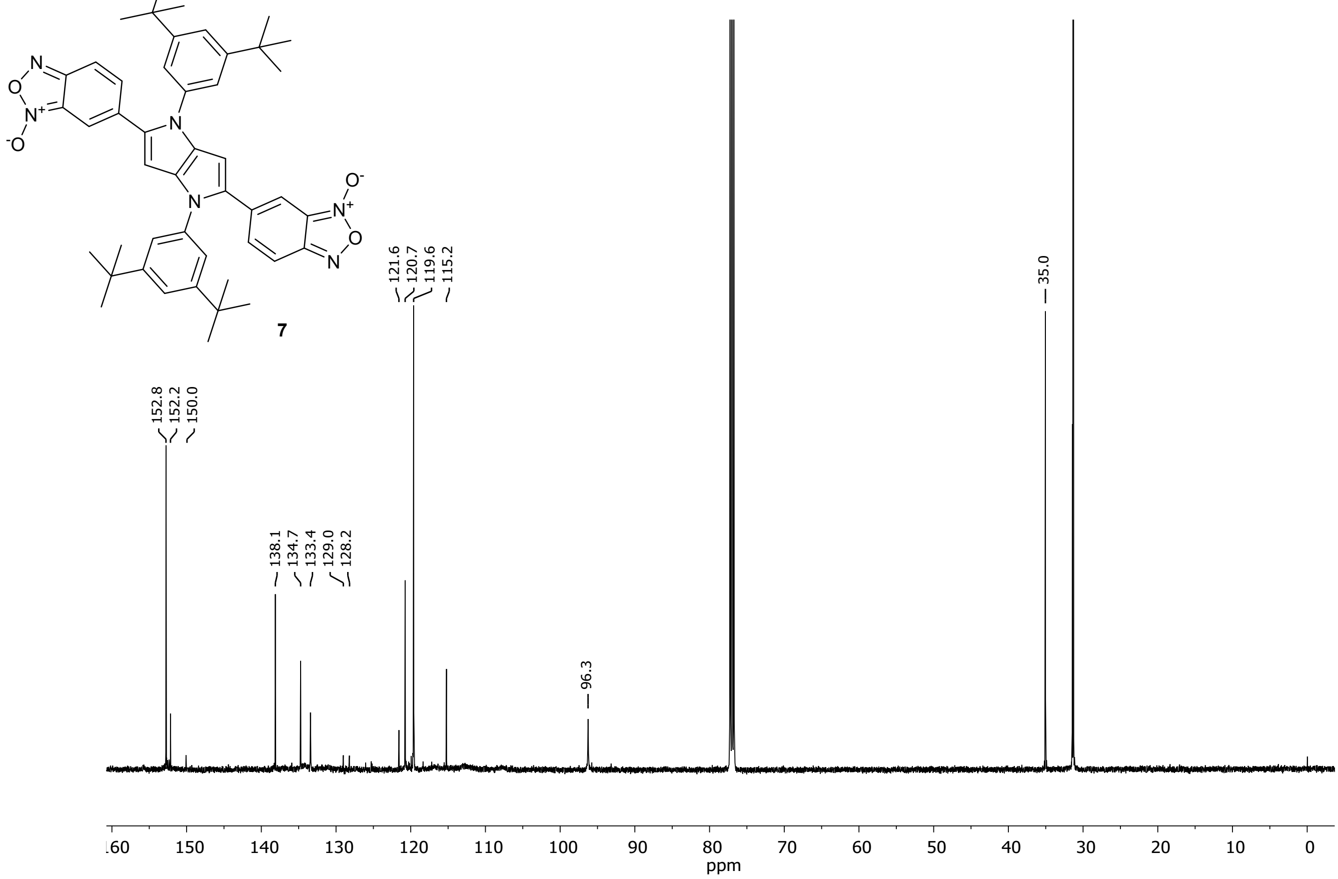
N
O
N+
O-
N
N
O-
N+
O
N
121.6
120.7
119.6
115.2
35.0
152.8
152.2
150.0
138.1
134.7
133.4
129.0
128.2
96.3
160 150 140 130 120 110 100 90 80 70 60 50 40 30 20 10 0
ppm

7

3. Optical properties in solution

Spectrophotometric grade solvents were used without further purification. All photophysical studies were performed with freshly-prepared, air-equilibrated solutions at room temperature. Steady-state fluorescence measurements were performed in standard 1 cm quartz cuvettes with dilute solutions (10^{-6} M, optical density <0.1) to minimize inner filter effects and/or aggregation. Absorption spectra were measured using UV-Vis Shimadzu UV-3600i Plus spectrophotometer. Lambert-Beer's law was used to calculate molar absorption coefficients. Emission spectra were measured using the Edinburgh Instruments FS5 spectrofluorometer equipped with the Hamamatsu R123456 photomultiplier. Fluorescence quantum yields (Φ_{fl}) were calculated from equation:

$$\Phi_{fl} = \Phi_{fl,st} \cdot \left(\frac{n^2 S}{n_{st}^2 S_{st}} \right) \cdot \frac{\left(1 - 10^{-A_{st}}\right)}{\left(1 - 10^{-A}\right)},$$

where subscript "st" denotes respective values for the reference ("standard" sample), A absorbance, n is a refractive index of a solvent and S is an integrated fluorescence intensity.

Table S1. Optical properties of **1** in solutions.

<table>
<tr><td colspan="6">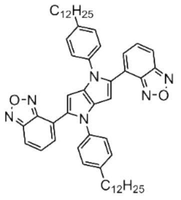
1</td></tr>
<tr><td>*Solvent*</td><td>λ_{abs}^{max} / nm</td><td>$\varepsilon \cdot 10^{-4}$ / $M^{-1} \cdot cm^{-1}$</td><td>λ_{em}^{max} / nm</td><td>Stokes' shift, $\Delta\tilde{\nu}$ / cm^{-1}</td><td>Φ_{fl} [a]</td></tr>
<tr><td>CCl_4</td><td>508</td><td>2.54</td><td>573</td><td>2 230</td><td>0.70</td></tr>
<tr><td>cyclohexane</td><td>499, 511</td><td>2.91, 2.91</td><td>553, 581 (shoulder)</td><td>1 490</td><td>0.77</td></tr>
<tr><td>EtOH</td><td>496</td><td>2.59</td><td>666</td><td>5 150</td><td>0.005</td></tr>
<tr><td>toluene</td><td>506</td><td>2.46</td><td>590</td><td>2 810</td><td>0.67</td></tr>
<tr><td>CH_2Cl_2</td><td>504</td><td>2.30</td><td>673</td><td>4 980</td><td>0.075</td></tr>
<tr><td>dioxane</td><td>502</td><td>2.55</td><td>617</td><td>3 710</td><td>0.59</td></tr>
<tr><td>DMF</td><td>498</td><td>2.25</td><td>688</td><td>5 550</td><td>0.020</td></tr>
<tr><td>DMSO</td><td>500</td><td>2.16</td><td>708</td><td>5 880</td><td>0.017</td></tr>
<tr><td>THF</td><td>501</td><td>2.48</td><td>620</td><td>3 910</td><td>0.44</td></tr>
</table>

[a] Relative Φ_{fl} were obtained using fluorescein in 0.1 M NaOH aqueous solution (λ_{exc} = 490 nm, Φ_{fl} = 0.9) as a reference.

Table S2. Optical properties of **2** in solutions.

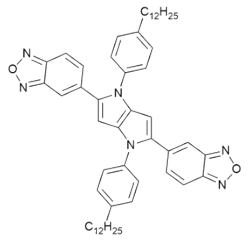

2

Solvent	λ_{abs}^{max} / nm	$\varepsilon \cdot 10^{-4}$ / $M^{-1} \cdot cm^{-1}$	λ_{em}^{max} / nm	Stokes' shift, $\Delta\tilde{\nu}$ / cm^{-1}	Φ_{fl} [a]
CCl_4	457	2.75	533	3 120	0.74
cyclohexane	448, 471	3.01, 2.95	499, 518 (shoulder)	1 190	0.88
EtOH	468	3.00	645	5 860	0.003
toluene	465	2.85	549	3 290	0.81
CH_2Cl_2	470	2.84	646	5 800	0.043
dioxane	464	2.97	583	4 400	0.74
DMF	475	2.54	682	6 390	0.005
DMSO	478	2.76	698	6 590	0.004
THF	469	2.89	609	4 900	0.35

[a] Relative Φ_{fl} were obtained using fluorescein in 0.1 M NaOH aqueous solution (λ_{exc} = 490 nm, Φ_{fl} = 0.9) as a reference.

Table S3. Optical properties of **3** in solutions.

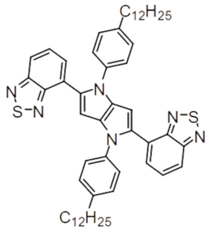

3

Solvent	λ_{abs}^{max} / nm	$\varepsilon \cdot 10^{-4}$ / $M^{-1} \cdot cm^{-1}$	λ_{em}^{max} / nm	Stokes' shift, $\Delta\tilde{\nu}$ / cm^{-1}	Φ_{fl} [a]
CCl_4	513	1.49	603	2 910	0.58
cyclohexane	506	1.75	572	2 280	0.52
toluene	510	1.73	625	3 610	0.36
CH_2Cl_2	498	1.72	716	6 110	0.030
dioxane	500	1.90	645	4 500	0.30
THF	507	1.44	657	4 500	0.25

[a] Relative Φ_{fl} were obtained using rhodamine 6G in EtOH (λ_{exc} = 510 nm, Φ_{fl} = 0.95) as a reference.

Table S4. Optical properties of **3a** in solutions.

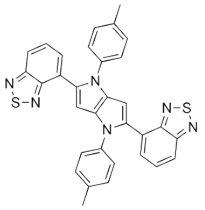

3a

Solvent	λ_{abs}^{max} / nm	$\varepsilon \cdot 10^{-4}$ / $M^{-1} \cdot cm^{-1}$	λ_{em}^{max} / nm	Stokes' shift, $\Delta\tilde{\nu}$ / cm^{-1}	Φ_{fl} [a]
cyclohexane	492	0.87	562	2 530	0.60
toluene	507	0.78	609	3 300	0.13
THF	501	2.29	633	4 160	0.29
CH_2Cl_2	505	2.00	672	4 920	0.10

[a] Relative Φ_{fl} were obtained using rhodamine 6G in EtOH (λ_{exc} = 510 nm, Φ_{fl} = 0.95) as a reference.

Table S5. Optical properties of **4** in solutions.

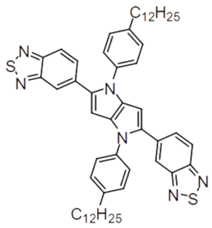

4

Solvent	λ_{abs}^{max} / nm	$\varepsilon \cdot 10^{-4}$ / $M^{-1} \cdot cm^{-1}$	λ_{em}^{max} / nm	Stokes' shift, $\Delta\tilde{\nu}$ / cm^{-1}	Φ_{fl} [a]
CCl_4	477	1.61	547	2 680	0.56
cyclohexane	464, 482	2.85, 2.91	519	1 480	0.78
toluene	477	3.22	564	3 230	0.57
CH_2Cl_2	476	3.03	661	5 880	0.12
dioxane	476	3.42	594	4 170	0.55
THF	479	2.96	620	4 750	0.45

[a] Relative Φ_{fl} were obtained using rhodamine 6G in EtOH (λ_{exc} = 510 nm, Φ_{fl} = 0.95) as a reference.

Table S6. Optical properties of **5** in solutions.

<table>
<tr><td colspan="6">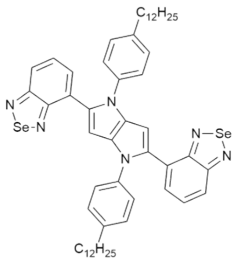
5</td></tr>
<tr><td>*Solvent*</td><td>λ_{abs}^{max} / nm</td><td>$\varepsilon \cdot 10^{-4}$ / $M^{-1} \cdot cm^{-1}$</td><td>λ_{em}^{max} / nm</td><td>Stokes' shift, $\Delta\tilde{\nu}$ / cm^{-1}</td><td>Φ_{fl} [a]</td></tr>
<tr><td>cyclohexane</td><td>544</td><td>1.31</td><td>622</td><td>2 310</td><td>0.081</td></tr>
<tr><td>toluene</td><td>544</td><td>1.30</td><td>675</td><td>3 570</td><td>0.040</td></tr>
<tr><td>CH_2Cl_2</td><td>532</td><td>1.93</td><td>879</td><td>7 420</td><td>0.018</td></tr>
<tr><td>dioxane</td><td>530</td><td>0.68</td><td>706</td><td>4 700</td><td>0.045</td></tr>
<tr><td>THF</td><td>536</td><td>1.40</td><td>726</td><td>4 880</td><td>0.034</td></tr>
</table>

[a] Relative Φ_{fl} were obtained using cresyl violet in EtOH (λ_{exc} = 610 nm, Φ_{fl} = 0.56) as a reference.

Table S7. Optical properties of **6** in solutions.

<table>
<tr><td colspan="6">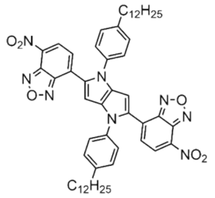
6</td></tr>
<tr><td>*Solvent*</td><td>λ_{abs}^{max} / nm</td><td>$\varepsilon \cdot 10^{-4}$ / $M^{-1} \cdot cm^{-1}$</td><td>λ_{em}^{max} / nm</td><td>Stokes' shift, $\Delta\tilde{\nu}$ / cm^{-1}</td><td>Φ_{fl} [a]</td></tr>
<tr><td>CCl_4</td><td>587, 624</td><td>3.88, 5.55</td><td>658, 703</td><td>830</td><td>0.70</td></tr>
<tr><td>cyclohexane</td><td>575, 618</td><td>3.62, 5.62</td><td>639, 691</td><td>530</td><td>0.79</td></tr>
<tr><td>toluene</td><td>620</td><td>5.05</td><td>679</td><td>1 400</td><td>0.45</td></tr>
<tr><td>CH_2Cl_2</td><td>648</td><td>4.13</td><td>737</td><td>1 860</td><td>0.004</td></tr>
<tr><td>dioxane</td><td>612</td><td>4.45</td><td>699</td><td>2030</td><td>0.051</td></tr>
<tr><td>THF</td><td>624</td><td>4.59</td><td>722</td><td>2 180</td><td>0.007</td></tr>
</table>

[a] Relative Φ_{fl} were obtained using cresyl violet in EtOH (λ_{exc} = 610 nm, Φ_{fl} = 0.56) as a reference.

Table S8. Optical properties of **7** in solutions.

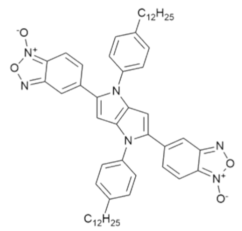

7

Solvent	λ_{abs}^{max} / nm	ε·10⁻⁴ / M⁻¹·cm⁻¹	λ_{em}^{max} / nm	Stokes' shift, $\Delta\tilde{\nu}$ / cm⁻¹	Φ_{fl} [a]
cyclohexane	494	1.62	542	1790	0.002
toluene	492	2.87	673	5 470	0.004
CH_2Cl_2	495	2.64	–	–	<0.001
dioxane	490	2.29	574	2 990	0.002
THF	497	2.72	586	3060	0.002

[a] Relative Φ_{fl} were obtained using fluorescein in 0.1 M NaOH aqueous solution (λ_{exc} = 490 nm, Φ_{fl} = 0.9) as a reference.

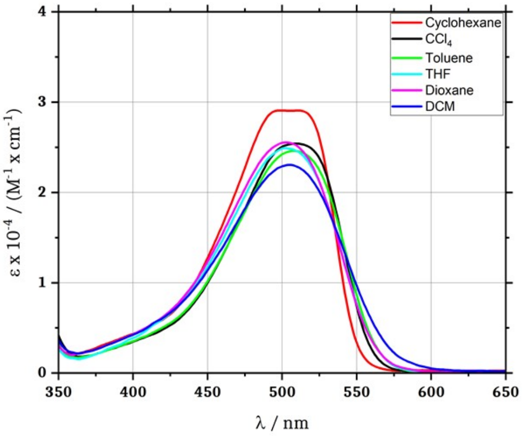

Figure S1. Absorption spectra of **1**.

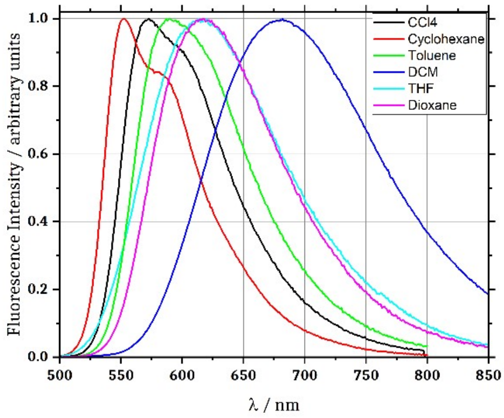

Figure S2. Emission spectra of **1**.

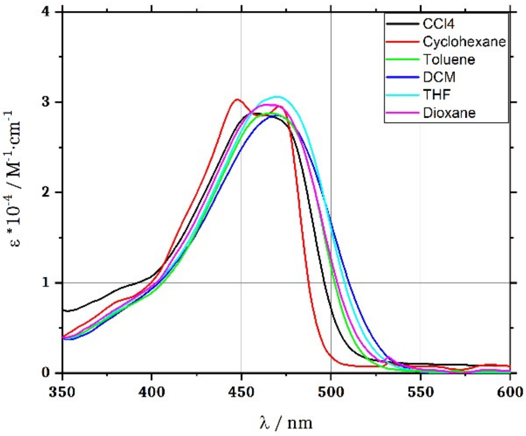

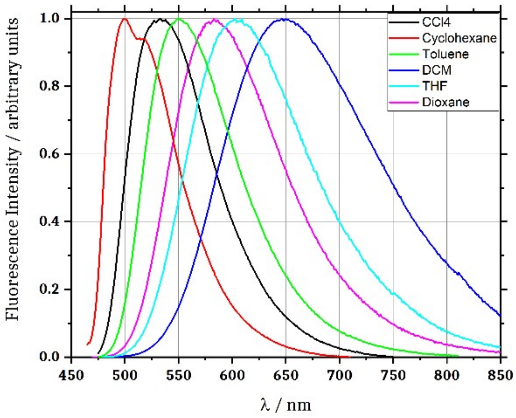

Figure S3. Absorption spectra of **2**.

Figure S4. Emission spectra of **2**.

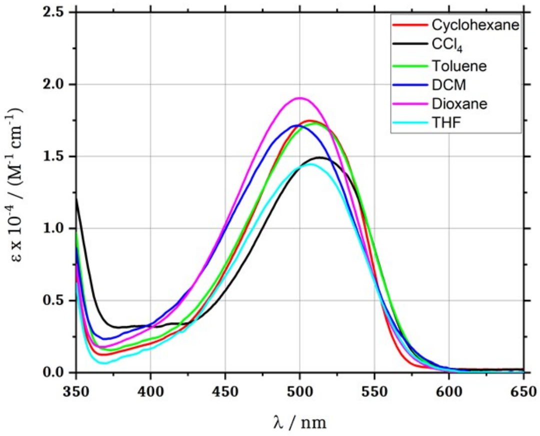

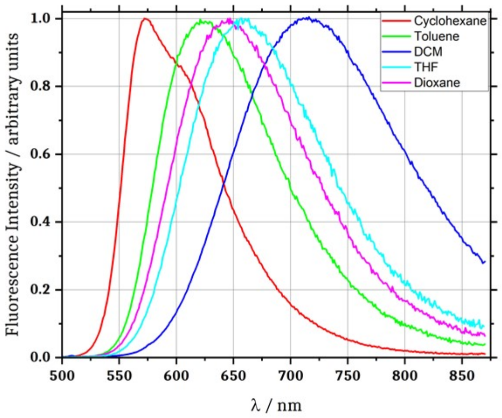

Figure .5. Absorption spectra of **3**.

Figure S6. Emission spectra of **3**.

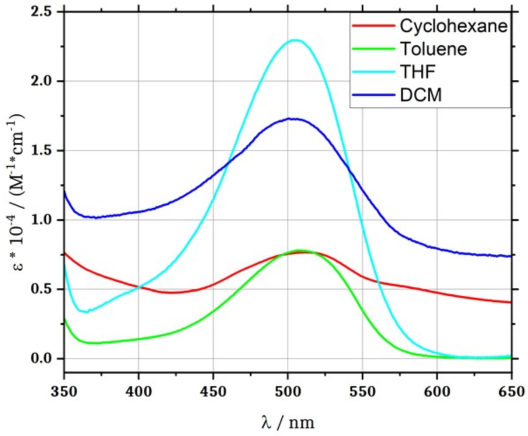

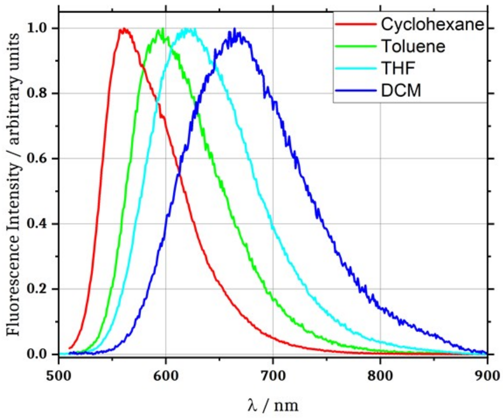

Figure S7. Absorption spectra of **3a**.

Figure S8. Emission spectra of **3a**.

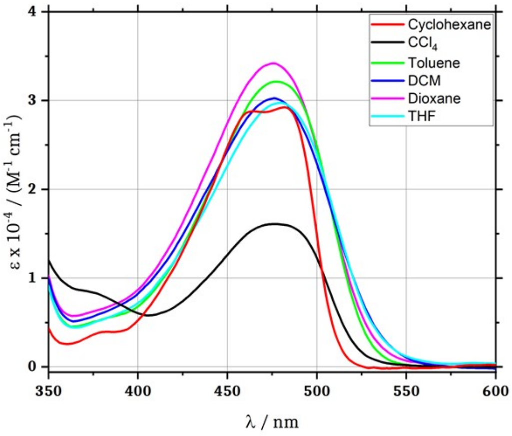

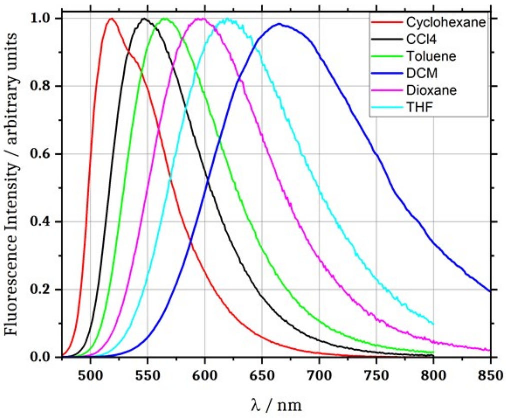

Figure S9. Absorption spectra of **4**.

Figure S10. Emission spectra of **4**.

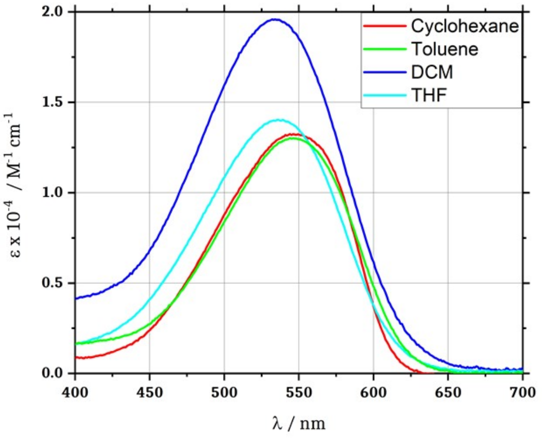

Figure S11. Absorption spectra of **5**.

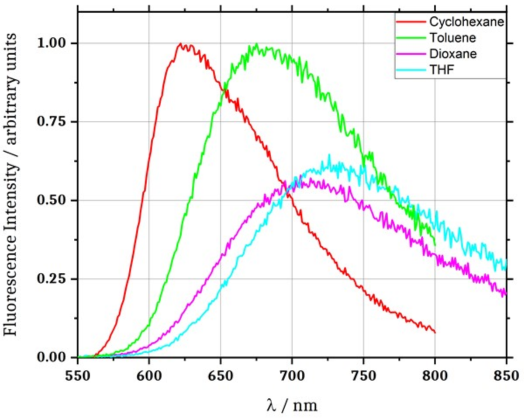

Figure S12. Emission spectra of **5**.

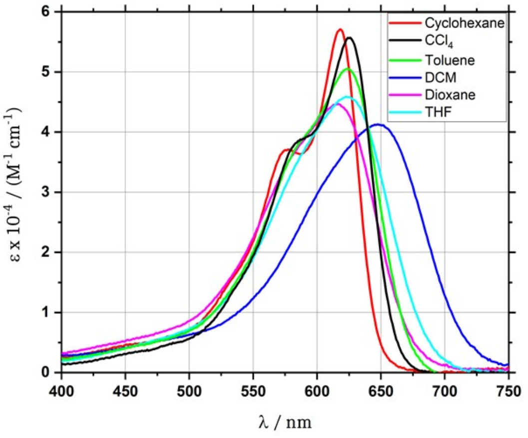

Figure S13. Absorption spectra of **6**.

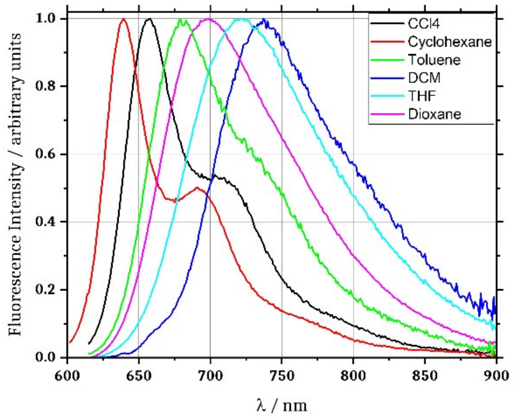

Figure S14. Emission spectra of **6**.

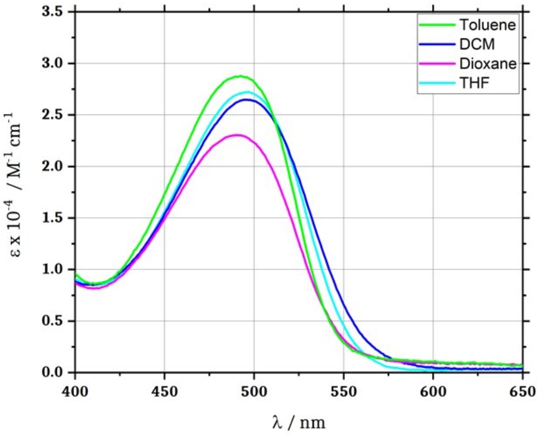

Figure S15. Absorption spectra of **7**.

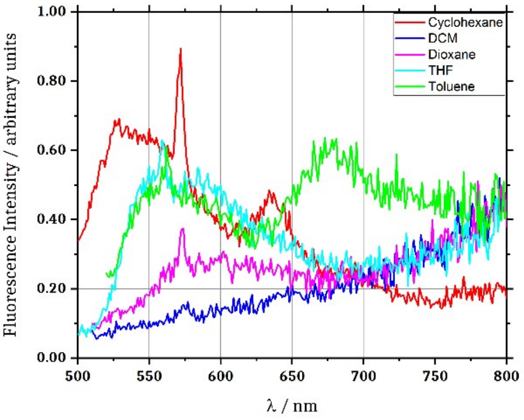

Figure S16. Emission spectra of **7**.

4. Solid-state spectroscopy

Absorption in the solid state was measured using powders of investigated substances, grinded in with a KBr in an agate mortar, followed by formation of a thin pellet on a hydraulic press. Absorption in pellets were measured in a transmission mode on the UV-Vis Shimadzu UV-3600i Plus spectrophotometer.

Time-resolved photoluminescence measurements were conducted on a custom-built setup at the Department Chemistry, University of Warsaw. Laser pulses generated by an Ekspla NT230 DPSS Nd:YAG laser were used to excite the samples (we have chosen 390 nm for compounds **2**–**4** and 470 nm for compound **6** as the excitation wavelength). The laser light was directed to the sample through the rear port of an Olympus IX73 inverted microscope, focused by a reflective objective. To prevent UV emission and backscattering from reaching the eye and detector, a dichroic mirror and a 395 nm long-pass filter were employed. Single-crystal samples were positioned on a thin quartz slide with a minimum amount of the non-luminescent Olympus Type-F immersion oil. The emitted light from the sample was collected through the reflective objective and directed to a spectrograph equipped with a time-gated intensified charge-coupled device (ICCD) camera (PI-MAX4, Princeton Instruments). The camera was triggered by each laser pulse, facilitating a precise control of the camera readout delay during the experiment. The LightField software (Princeton Instruments) was employed to control the camera's intensifier gating width and delay, enabling time-resolved measurements of the samples' emission. The luminescence lifetimes were determined by fitting the intensity decay data using the least-squares method.

Table S9. Optical properties of compounds **1**–**4** and **6**–**7** in the solid state.

Compound	λ_{abs}^{max} / nm	λ_{em}^{max} / nm	Stokes' shift, $\Delta\tilde{\nu}$ / cm^{-1}	Φ_{pl}
1	518	577	1 970	0.20
2a	478	582	3 740	0.06
3	463	564	3 870	0.43
4	489	563	2 690	0.05
6	681	737	1 120	0.02
7	539	789	5 880	<0.01

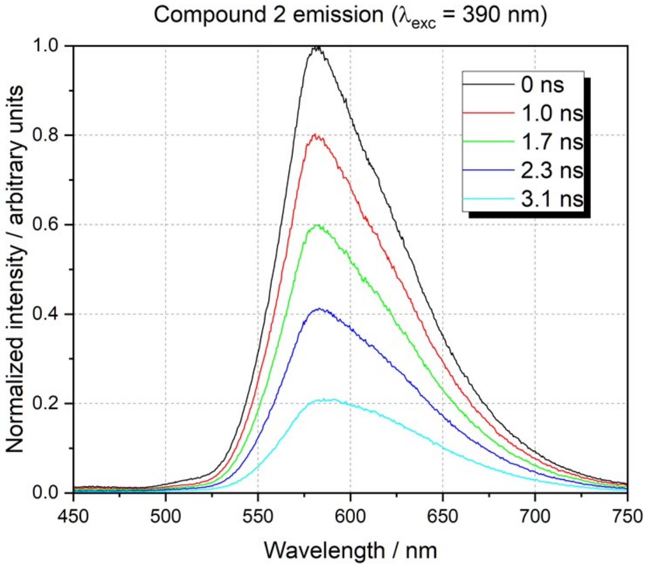

Figure S17. Time-resolved emission spectra of **2**.

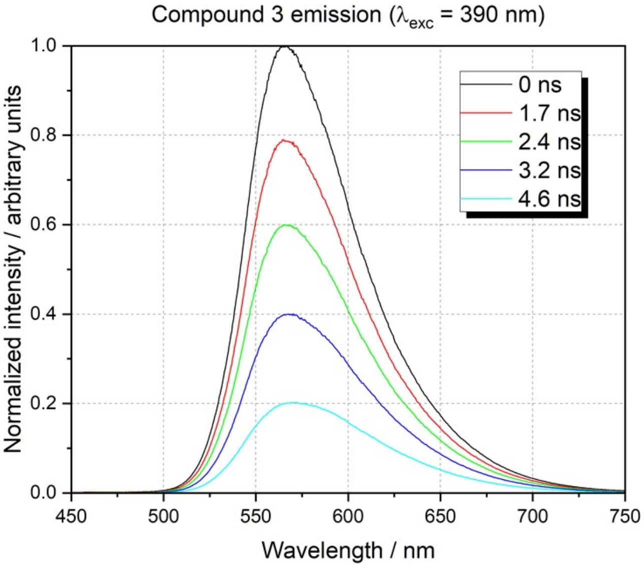

Figure S18. Time-resolved emission spectra of **3**.

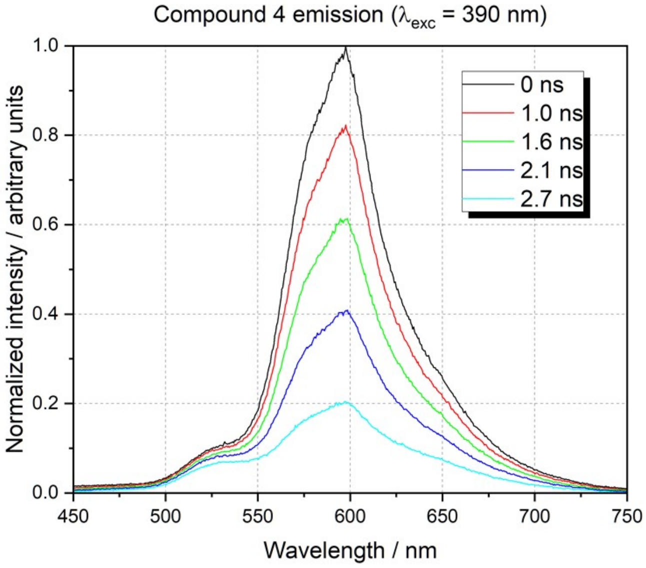

Figure S19 Time-resolved emission spectra of **4.**

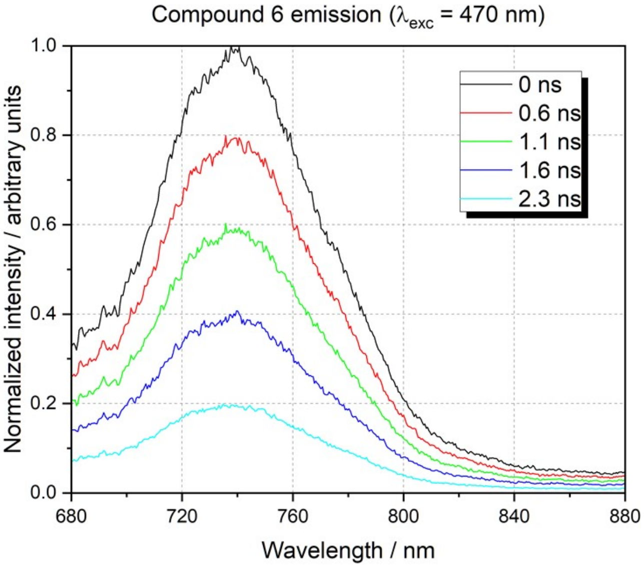

Figure S20. Time-resolved emission spectra of **6.**

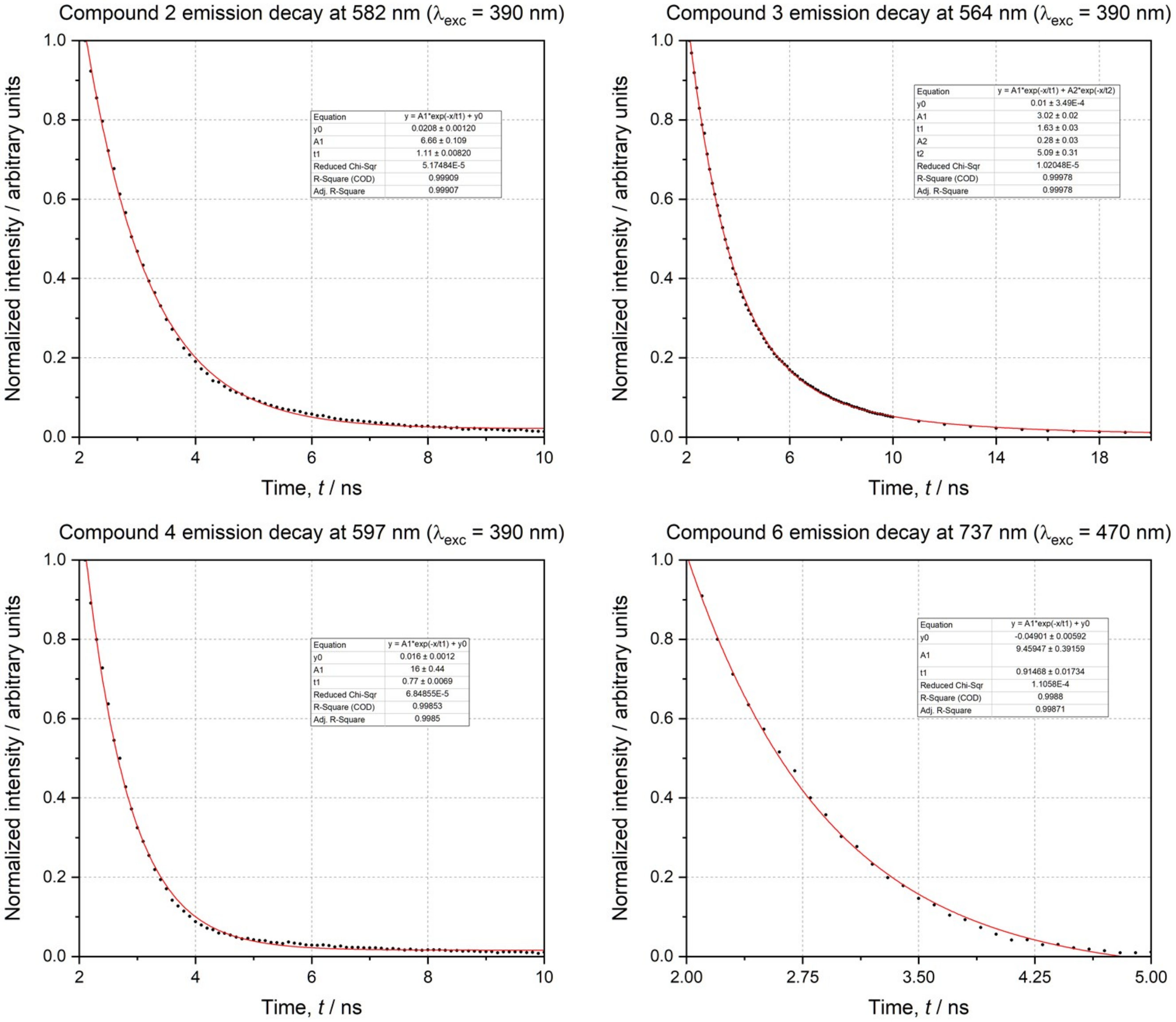

Equation	y = A1*exp(-x/t1) + y0
y0	0.0208 ± 0.00120
A1	6.66 ± 0.109
t1	1.11 ± 0.00820
Reduced Chi-Sqr	5.17484E-5
R-Square (COD)	0.99909
Adj. R-Square	0.99907

Equation	y = A1*exp(-x/t1) + A2*exp(-x/t2)
y0	0.01 ± 3.49E-4
A1	3.02 ± 0.02
t1	1.63 ± 0.03
A2	0.28 ± 0.03
t2	5.09 ± 0.31
Reduced Chi-Sqr	1.02048E-5
R-Square (COD)	0.99978
Adj. R-Square	0.99978

Equation	y = A1*exp(-x/t1) + y0
y0	0.016 ± 0.0012
A1	16 ± 0.44
t1	0.77 ± 0.0069
Reduced Chi-Sqr	6.84855E-5
R-Square (COD)	0.99853
Adj. R-Square	0.9985

Equation	y = A1*exp(-x/t1) + y0
y0	-0.04901 ± 0.00592
A1	9.45947 ± 0.39159
t1	0.91468 ± 0.01734
Reduced Chi-Sqr	1.1058E-4
R-Square (COD)	0.9988
Adj. R-Square	0.99871

Figure S21. Emission decays of compounds **2**–**4** and **6**.

5. Crystallographic data

Single-crystal X-ray diffraction measurements were performed on a Rigaku Oxford Diffraction SuperNova instrument equipped with a copper X-ray source (Cu K_α radiation, λ = 1.54184 Å). During the measurement crystal was maintained at 100 or 120 K with the use of an Oxford Cryosystems nitrogen gas-flow device. Unit-cell parameter determination and raw diffraction image processing were performed with the native diffractometer *CRYSALISPRO* software suite. Structures were solved using an intrinsic phasing method as implemented in the *SHELXT* program[8] and refined with the *SHELXL* program[9] within *OLEX2*[10] package using the independent atom model approximation. In all cases the riding model for the hydrogen thermal motion parameters was applied ($U_{iso}^{H} = x \cdot U_{eq}^{X}$, where x = 1.2 for X = C, and x = 1.5 for X = O). Structure of compound **1** was re-refined, and labels were changed to fit all other compounds reported here. Thus, slight changes to the previous refinement are observed, but without any change of the conclusions already published. Compound **7** contains voids, but unfortunately we were unable to find a reasonable structural model, thus only the dye molecules are taken into account. We presume some solvent molecules might be present in the structure, but the data quality does not allow to extract a meaningful information, even when the SQUEEZE[11] procedure was applied. Finally, the data set was refined on the original unmodified data. The CIF files are available from the Supporting Information, or can be retrieved from the Cambridge Structural Database[12,13] (deposition numbers: CCDC 2359982−7; compound **1** was previously deposited under the number CCDC 2288872 [2] and it is now revised under new number CCDC 2360191).

Table S10. Selected X-ray data collection, processing and refinement parameters for studied compounds. For more details see the CIF files.

Data set	**1** (revised)	**2a**	**3**	**3a**	**4**	**6**	**7**
Moiety formula	$C_{54}H_{66}N_6O_2$ + 0.82 CH_2Cl_2	$C_{32}H_{22}N_6O_2$	$C_{54}H_{66}N_6S_2$	$C_{32}H_{22}N_6S_2$	$C_{54}H_{66}N_6S_2$	$C_{54}H_{64}N_8O_6$	$C_{46}H_{50}N_6O_4$
Moiety formula mass, M_r / a.u.	901.11	522.56	863.24	554.67	863.24	921.13	750.92
Crystal system	triclinic	monoclinic	triclinic	monoclinic	monoclinic	monoclinic	monoclinic
Space group	$P\bar{1}$ (No. 2)	$C2/c$ (No. 15)	$P\bar{1}$ (No. 2)	$P2_1/c$ (No. 14)	$P2_1/c$ (No. 14)	$C2/c$ (No. 15)	$P2_1/n$ (No. 14)
Z	2	4	2	2	2	4	4
F_{000}	965	1088	464	576	928	1968	1600
Crystal colour & shape	clear red needle	orange block	yellow needle	dark orange needle	light orange block	clear dark violet plate	orange block
Crystal size / mm^3	0.09×0.16×0.20	0.09×0.11×0.24	0.09×0.12×0.42	0.05×0.05×0.05	0.03×0.07×0.14	0.11×0.26×0.41	0.05×0.06×0.31
T / K	100	100	100	100	100	120	100
a / Å	8.0413(5)	23.4345(4)	6.81179(12)	6.73075(18)	26.3539(14)	47.3727(18)	12.6530(2)
b / Å	14.3206(8)	7.9786(2)	8.26449(16)	13.0685(4)	5.7949(2)	10.9462(5)	17.7756(3)
c / Å	21.6156(8)	13.6019(2)	20.8251(4)	14.6429(4)	16.2792(11)	9.5717(4)	18.8818(4)
α / °	78.691(4)	90	92.8453(16)	90	90	90	90
β / °	88.151(4)	105.599(2)	96.3218(15)	91.099(3)	106.857(7)	90.519(4)	102.848(2)
γ / °	87.222(5)	90	95.0155(15)	90	90	90	90
V / Å^3	2437.3(2)	2449.53(9)	1158.70(4)	1287.76(6)	2379.3(2)	4963.2(4)	4140.47(13)
d_{calc} / g·cm^{-3}	1.228	1.417	1.237	1.430	1.205	1.233	1.205
θ range	2.085–75.726°	3.917–76.075°	2.138–76.140°	4.535–76.134°	3.505–77.736°	3.732–73.429°	3.456–76.403°
Absorption coefficient, μ / mm^{-1}	1.388	0.741	1.370	2.154	1.335	0.653	0.620
No. of reflections collected / unique	38160 / 9943	7892 / 2530	4819 / 28235	10207 / 2667	19841 / 4943	53952 / 4929	34642 / 8612
R_{int}	6.45%	2.05%	4.01%	4.29%	8.45%	15.13%	7.53%
No. of reflections with $I > 2\sigma(I)$	7145	2312	4411	2311	3337	2975	6035
No. of parameters / restraints	589 / 0	182 / 0	281 / 0	182 / 0	281 / 0	308 / 0	639 / 78
$R[F]$ $(I > 2\sigma(I))$	7.32%	3.58%	345%	4.72%	6.34%	5.61%	5.48%
$wR[F^2]$ (all data)	22.61%	9.69%	10.64%	13.29%	19.72%	15.79%	15.91%
$\varrho_{res}^{min/max}$ / e·Å^{-3}	−0.84 / +1.27	−0.22 / +0.24	−0.39 / +0.09	− 0.31 / +0.54	−0.41 / +0.35	−0.18 / +0.23	−0.27 / +0.37
CCDC code	2360191 (new)	2359982	2359985	2359983	2359984	2359986	2359987

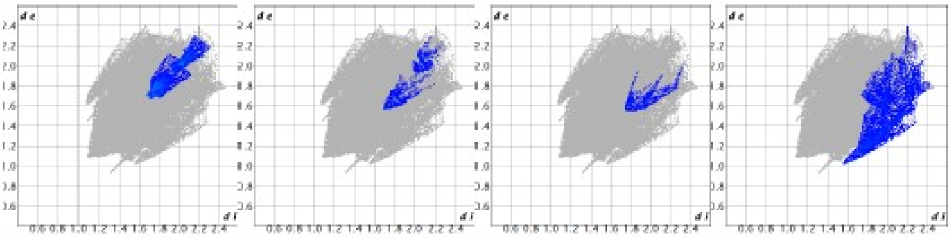

(a) Fingerprint of C-C interaction
(b) Fingerprint of C-N interaction
(c) Fingerprint of C-O interaction
(d) Fingerprint of C-H interaction

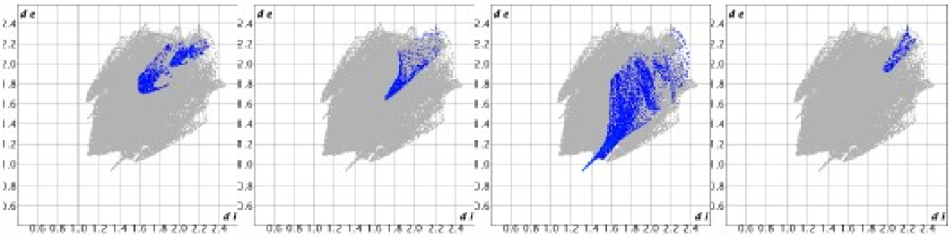

(e) Fingerprint of N-C interaction
(f) Fingerprint of N-O interaction
(g) Fingerprint of N-H interaction
(h) Fingerprint of C-Cl interaction

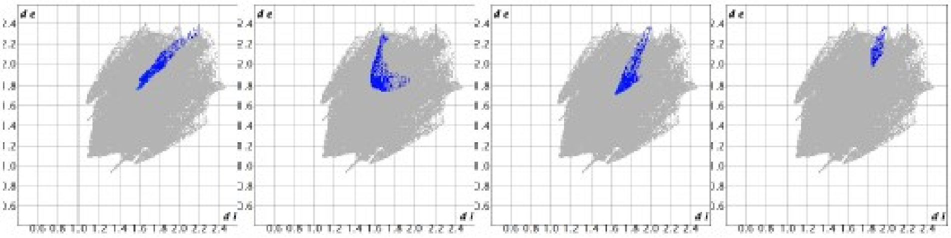

(i) Fingerprint of N-Cl interaction
(j) Fingerprint of O-C interaction
(k) Fingerprint of O-N interaction
(l) Fingerprint of O-Cl interaction

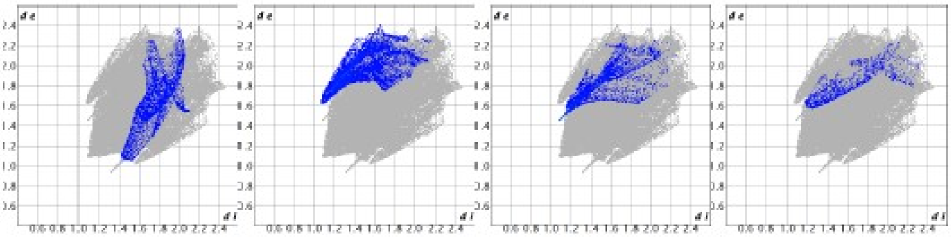

(m) Fingerprint of O-H interaction
(n) Fingerprint of H-C interaction
(o) Fingerprint of H-N interaction
(p) Fingerprint of H-O interaction

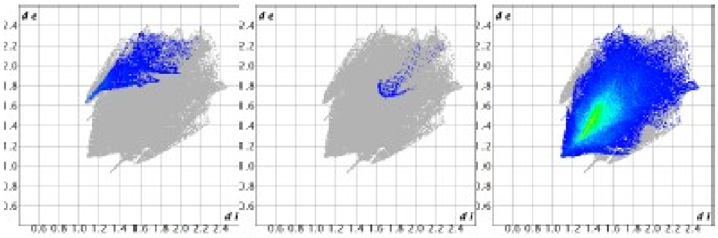

(q) Fingerprint of H-Cl interaction
(r) Fingerprint of N-N interaction
(s) Fingerprint of H-H interaction

Figure S22. Fingerprints of intermolecular interactions of **2**.

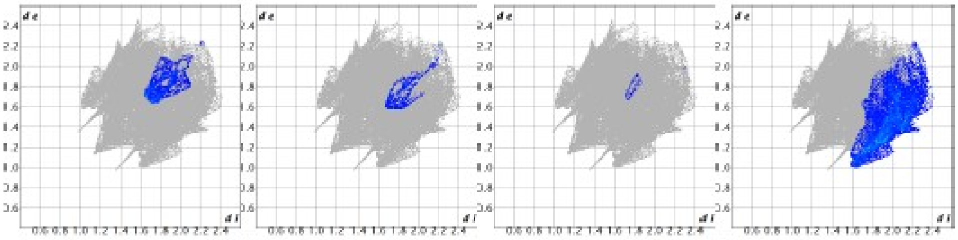

(a) Fingerprint of C-C interaction

(b) Fingerprint of C-N interaction

(c) Fingerprint of C-O interaction

(d) Fingerprint of C-H interaction

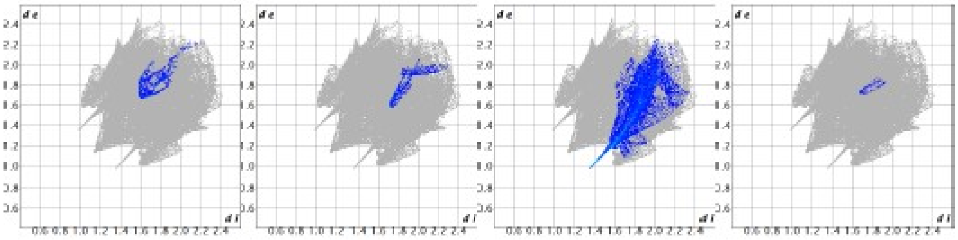

(e) Fingerprint of N-C interaction

(f) Fingerprint of N-O interaction

(g) Fingerprint of N-H interaction

(h) Fingerprint of O-C interaction

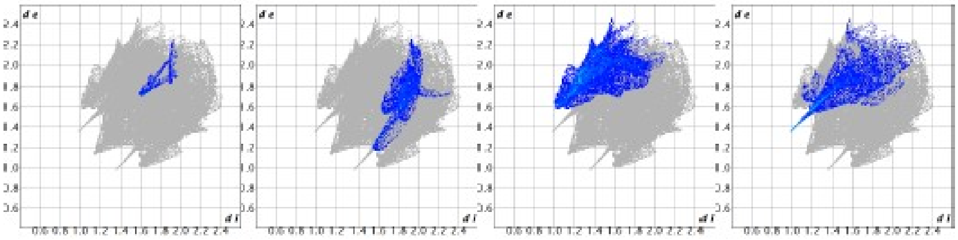

(i) Fingerprint of O-N interaction

(j) Fingerprint of O-H interaction

(k) Fingerprint of H-C interaction

(l) Fingerprint of H-N interaction

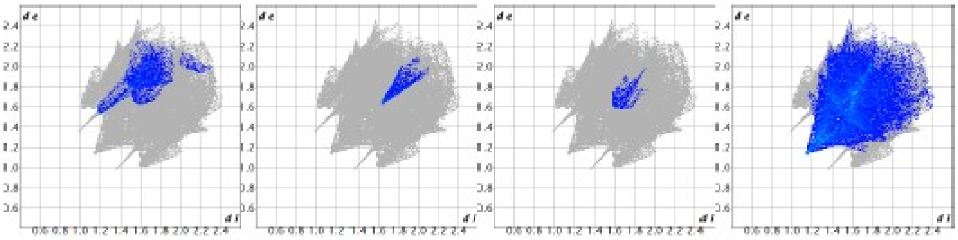

(m) Fingerprint of H-O interaction

(n) Fingerprint of N-N interaction

(o) Fingerprint of O-O interaction

(p) Fingerprint of H-H interaction

Figure S23. Fingerprints of intermolecular interactions of **3a**.

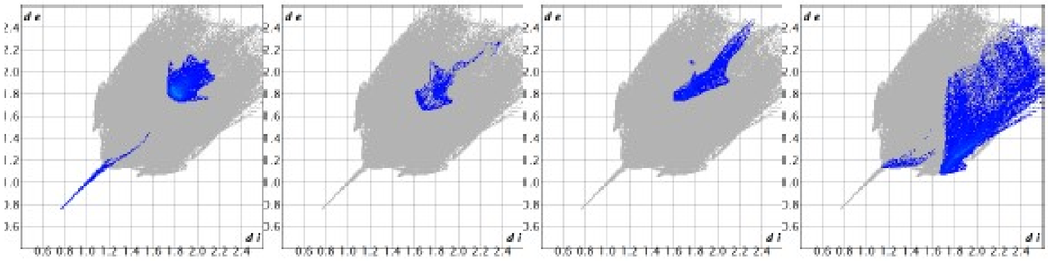

(a) Fingerprint of C-C interaction

(b) Fingerprint of C-N interaction

(c) Fingerprint of C-S interaction

(d) Fingerprint of C-H interaction

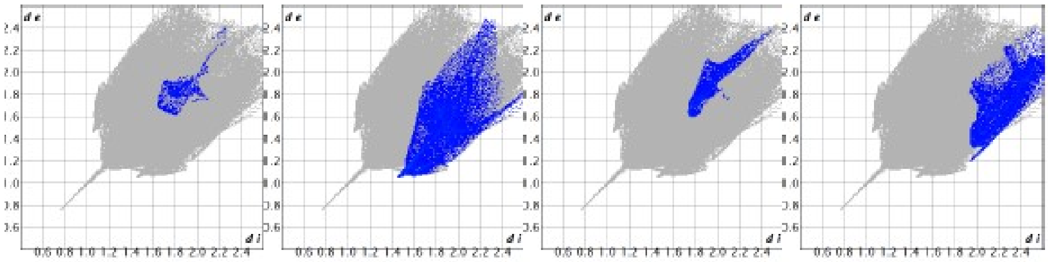

(e) Fingerprint of N-C interaction

(f) Fingerprint of N-H interaction

(g) Fingerprint of S-C interaction

(h) Fingerprint of S-H interaction

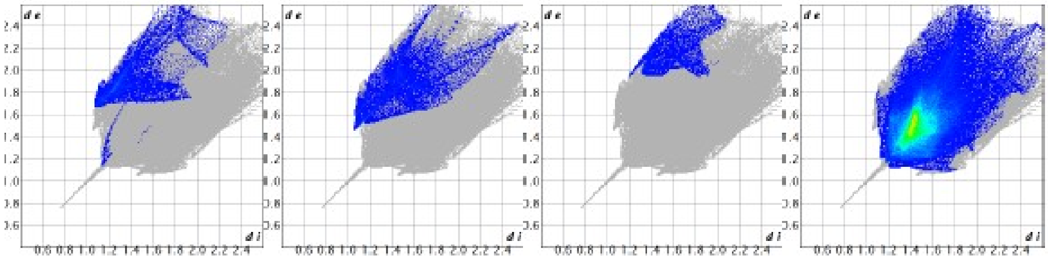

(i) Fingerprint of H-C interaction

(j) Fingerprint of H-N interaction

(k) Fingerprint of H-S interaction

(l) Fingerprint of H-H interaction

Figure S24. Fingerprints of intermolecular interactions of **4**.

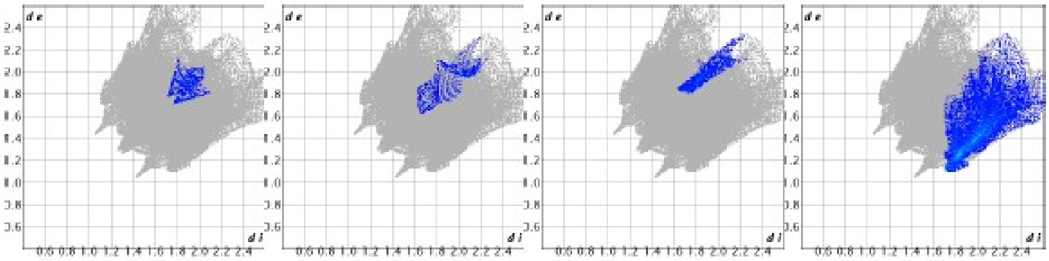

(a) Fingerprint of C-C interaction

(b) Fingerprint of C-N interaction

(c) Fingerprint of C-S interaction

(d) Fingerprint of C-H interaction

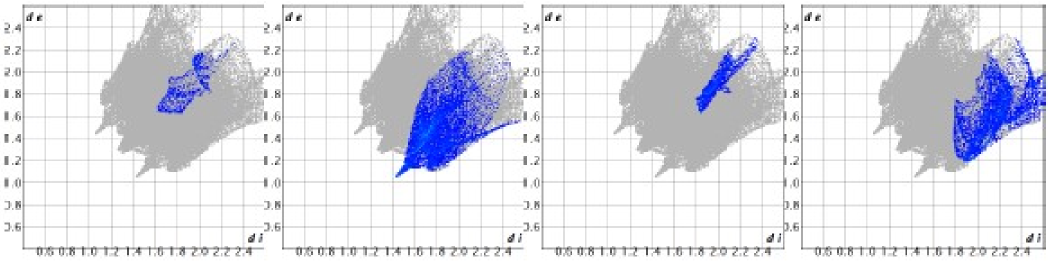

(e) Fingerprint of N-C interaction

(f) Fingerprint of N-H interaction

(g) Fingerprint of S-C interaction

(h) Fingerprint of S-H interaction

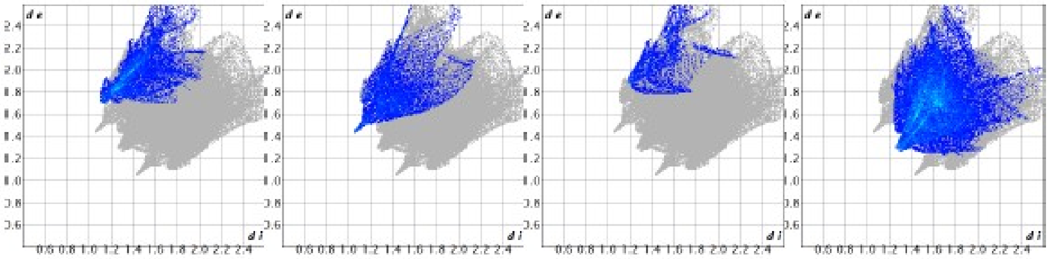

(i) Fingerprint of H-C interaction

(j) Fingerprint of H-N interaction

(k) Fingerprint of H-S interaction

(l) Fingerprint of H-H interaction

Figure S25. Fingerprints of intermolecular interactions of **4a**.

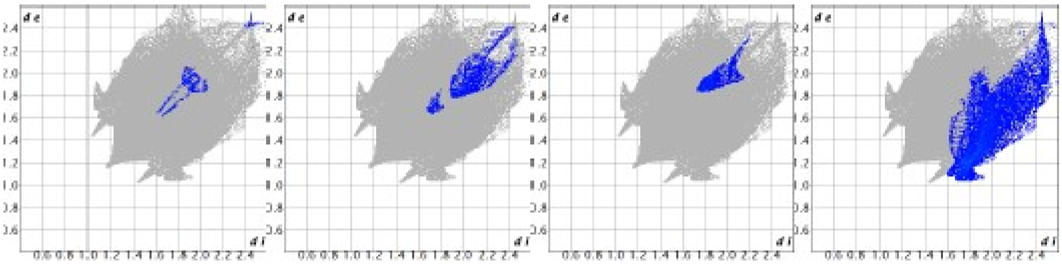

(a) Fingerprint of C-C interaction (b) Fingerprint of C-N interaction (c) Fingerprint of C-S interaction (d) Fingerprint of C-H interaction

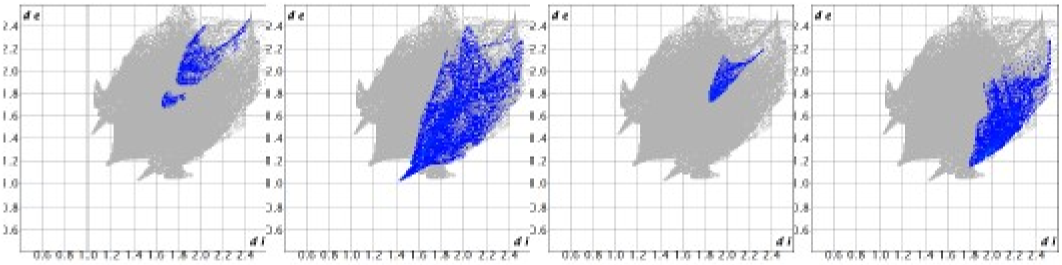

(e) Fingerprint of N-C interaction (f) Fingerprint of N-H interaction (g) Fingerprint of S-C interaction (h) Fingerprint of S-H interaction

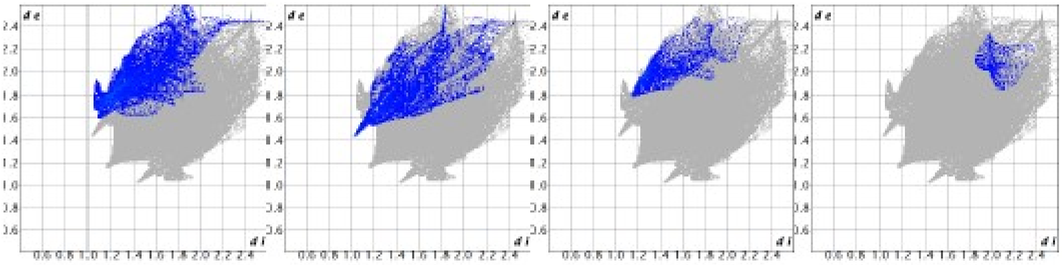

(i) Fingerprint of H-C interaction (j) Fingerprint of H-N interaction (k) Fingerprint of H-S interaction (l) Fingerprint of N-N interaction

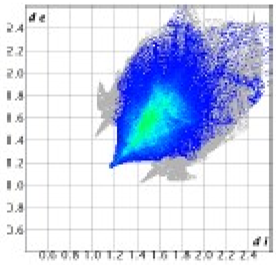

(m) Fingerprint of H-H interaction

Figure S26. Fingerprints of intermolecular interactions of **5**.

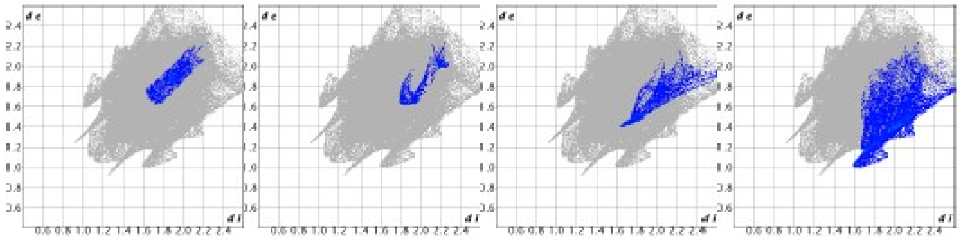

(a) Fingerprint of C-C interaction (b) Fingerprint of C-N interaction (c) Fingerprint of C-O interaction (d) Fingerprint of C-H interaction

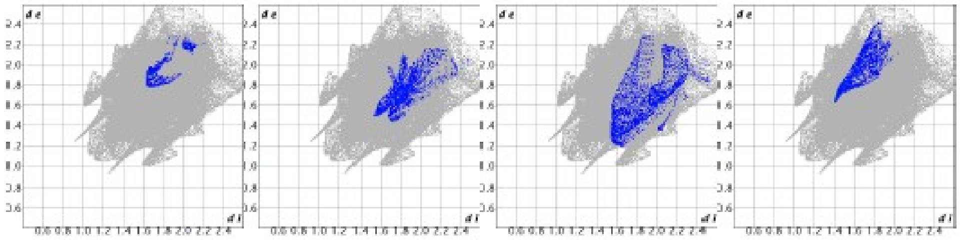

(e) Fingerprint of N-C interaction (f) Fingerprint of N-O interaction (g) Fingerprint of N-H interaction (h) Fingerprint of O-C interaction

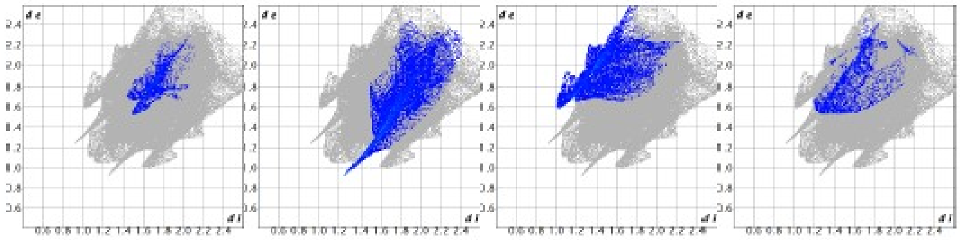

(i) Fingerprint of O-N interaction (j) Fingerprint of O-H interaction (k) Fingerprint of H-C interaction (l) Fingerprint of H-N interaction

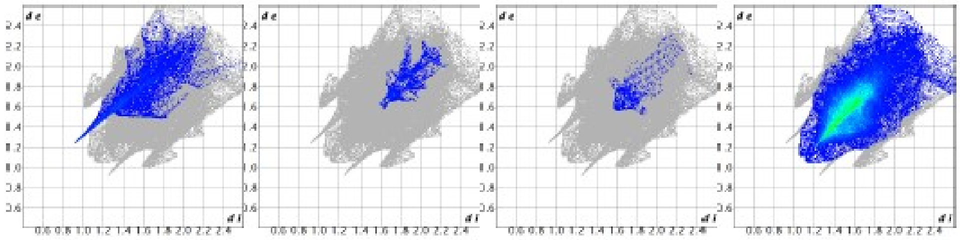

(m) Fingerprint of H-O interaction (n) Fingerprint of N-N interaction (o) Fingerprint of O-O interaction (p) Fingerprint of H-H interaction

Figure S27. Fingerprints of intermolecular interactions of **6**.

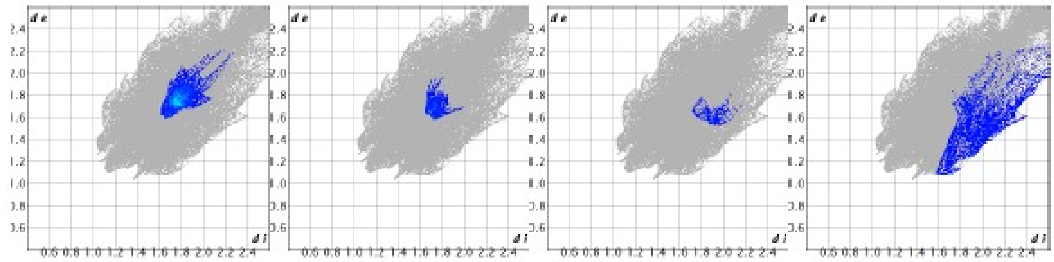

(a) Fingerprint of C-C interaction (b) Fingerprint of C-N interaction (c) Fingerprint of C-O interaction (d) Fingerprint of C-H interaction

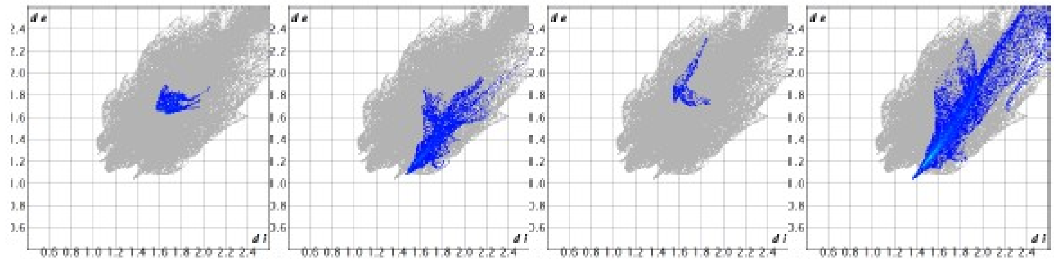

(e) Fingerprint of N-C interaction (f) Fingerprint of N-H interaction (g) Fingerprint of O-C interaction (h) Fingerprint of O-H interaction

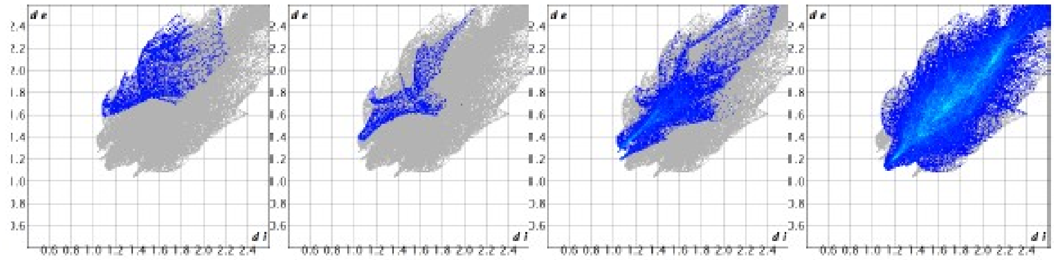

(i) Fingerprint of H-C interaction (j) Fingerprint of H-N interaction (k) Fingerprint of H-O interaction (l) Fingerprint of H-H interaction

Figure S28. Fingerprints of intermolecular interactions of **7**.

Powder X-ray diffraction (PXRD) measurements were carried out on a Bruker AXS D8 Discover powder diffractometer equipped with a VÅNTEC detector and a copper X-ray tube. All data were collected in a parallel-beam geometry (locked-couple experiment mode) in the 2θ range from 3 to 60°. In all cases the Le Bail refinement show a good correspondence between the bulk phase used for the fluorescence quantum yield determination (powder) and the single-crystal structure as determined via X-ray diffraction. *Remark:* Some more deviations were observed for the sample of **1** (our previous contribution, not shown here), which we ascribe to the presence of the labile solvent in the crystal. The DCM can evaporate readily during the sample preparation for the PXRD experiments. We note that higher residuals in some cases result from limited resolution of our in-house PXRD data collections. One could observe the highest-intensity peaks are rather asymmetric, which could not be taken into account in our modelling. This would require better resolution data, preferably collected on a synchrotron source where one has a better control over the beam size and divergence.

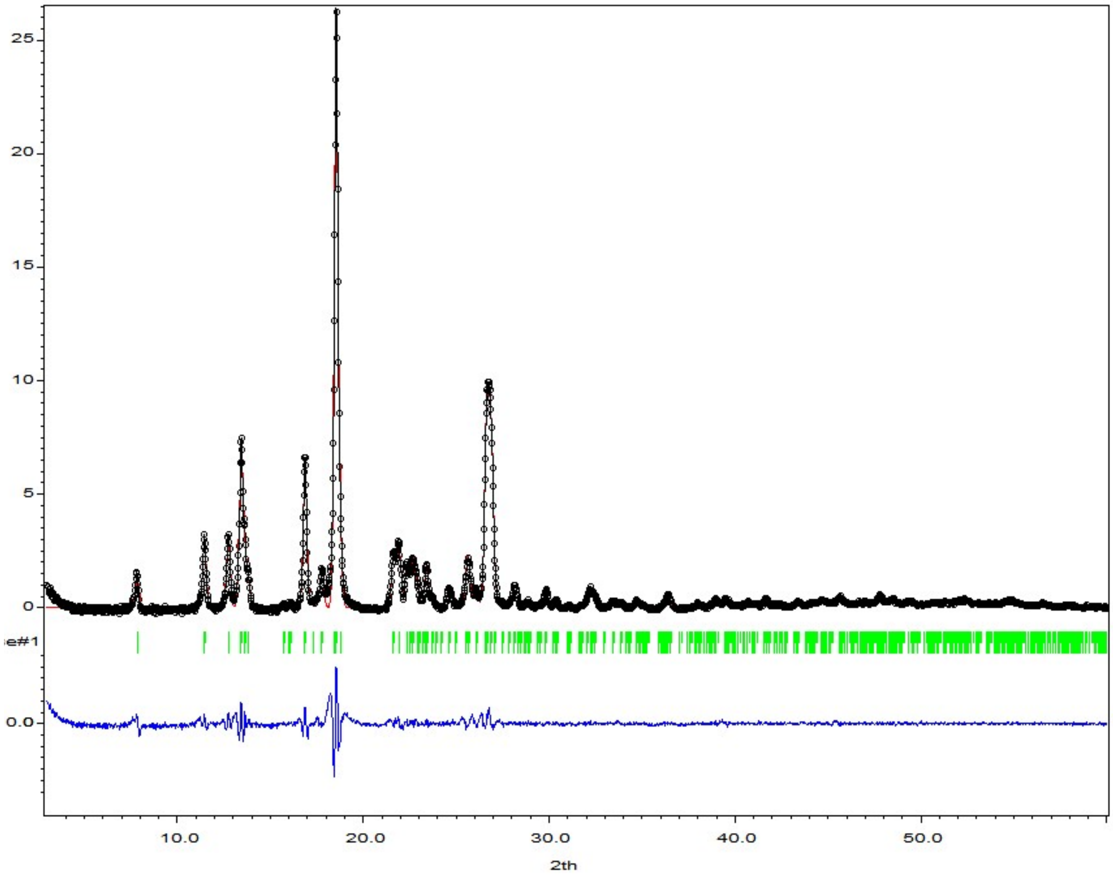

Figure S29. PXRD pattern obtained for the bulk sample of **2a**. Vertical axis – intensity, black curve – experimental pattern, red – Le Bail-fitted model, green bars – reflection positions (taking into account both $K_{\alpha1}$-$K_{\alpha2}$ splitting), blue – residual.

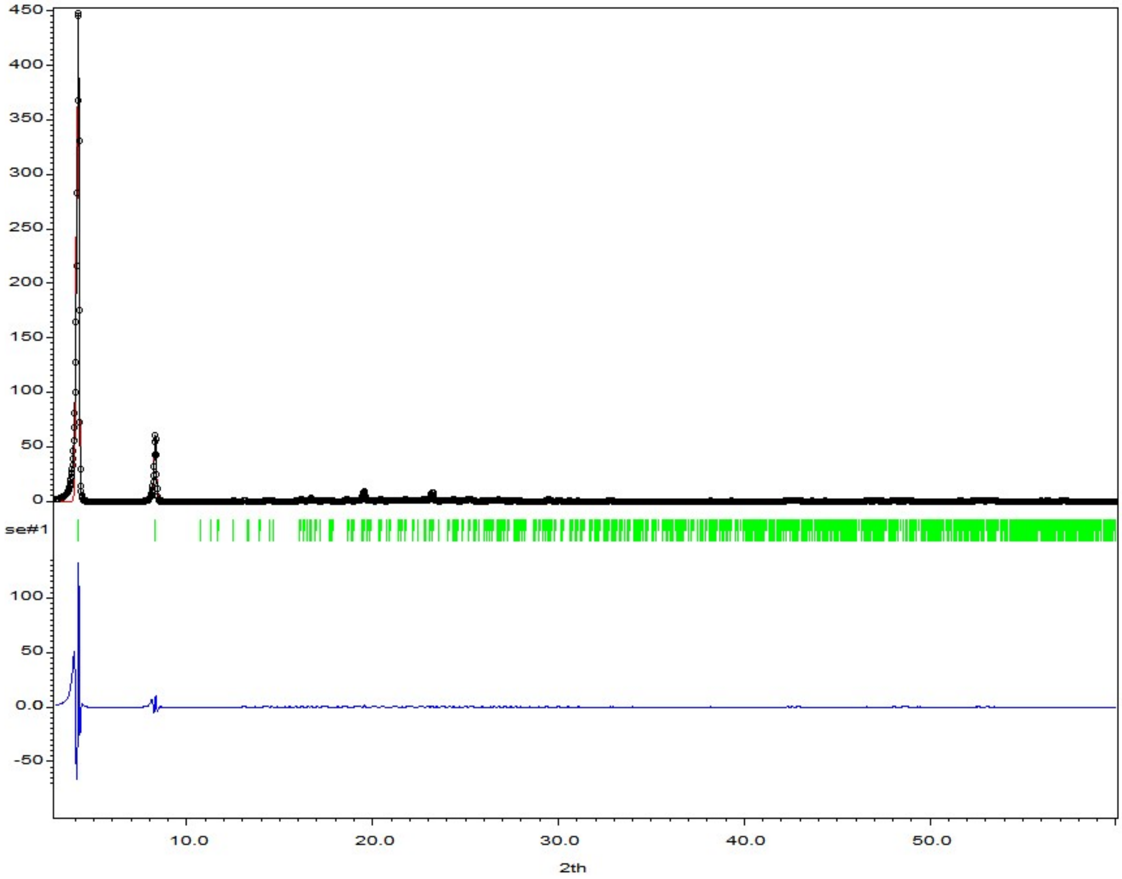

Figure S30. PXRD pattern obtained for the bulk sample of **3**. Vertical axis – intensity, black curve – experimental pattern, red – Le Bail-fitted model, green bars – reflection positions (taking into account both $K_{\alpha1}$-$K_{\alpha2}$ splitting), blue – residual.

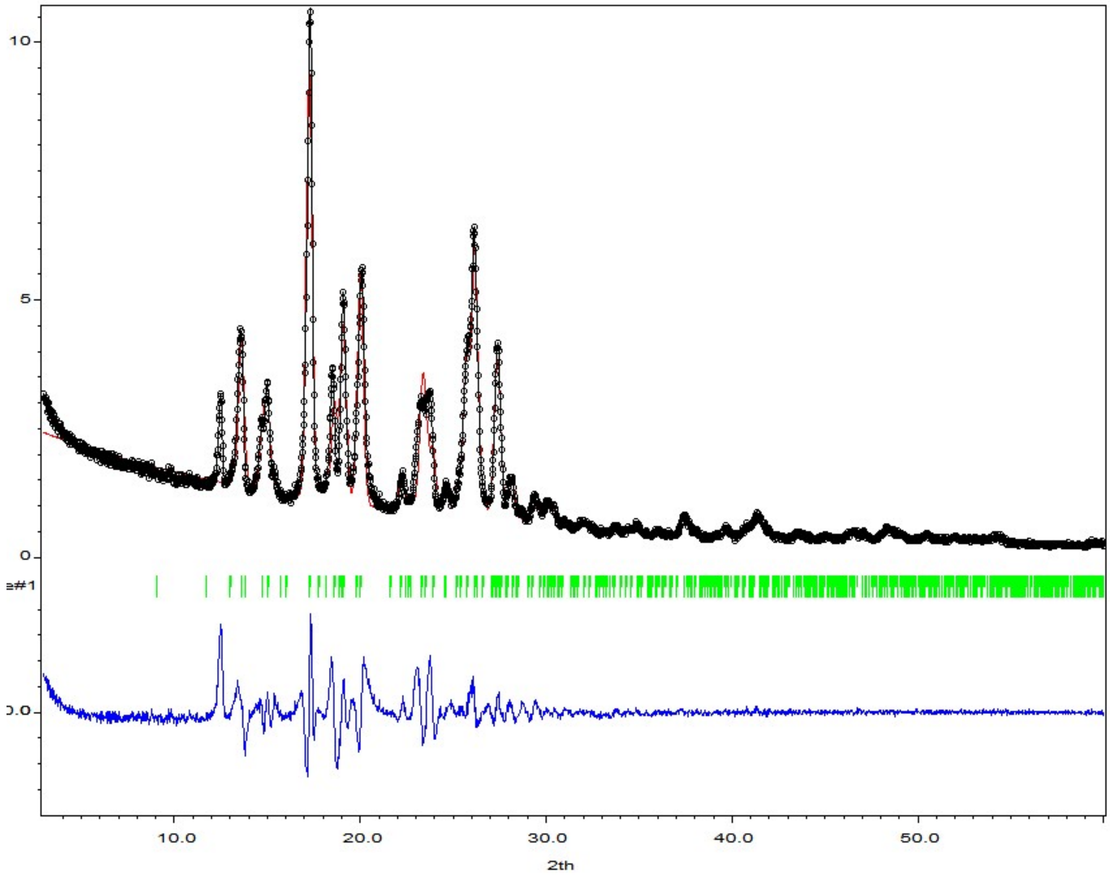

Figure S31. PXRD pattern obtained for the bulk sample of **3a**. Vertical axis – intensity, black curve – experimental pattern, red – Le Bail-fitted model, green bars – reflection positions (taking into account both $K_{\alpha1}$-$K_{\alpha2}$ splitting), blue – residual.

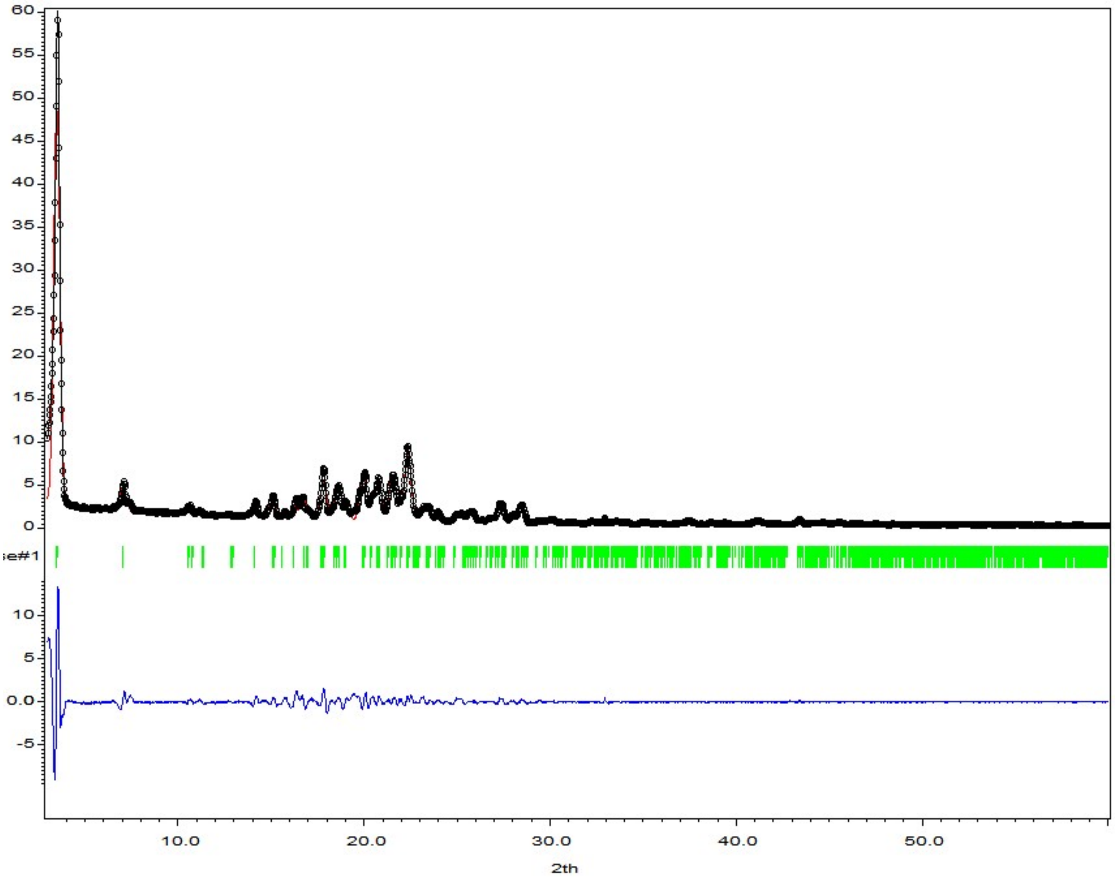

Figure S32. PXRD pattern obtained for the bulk sample of **4**. Vertical axis – intensity, black curve – experimental pattern, red – Le Bail-fitted model, green bars – reflection positions (taking into account both $K_{\alpha 1}$-$K_{\alpha 2}$ splitting), blue – residual.

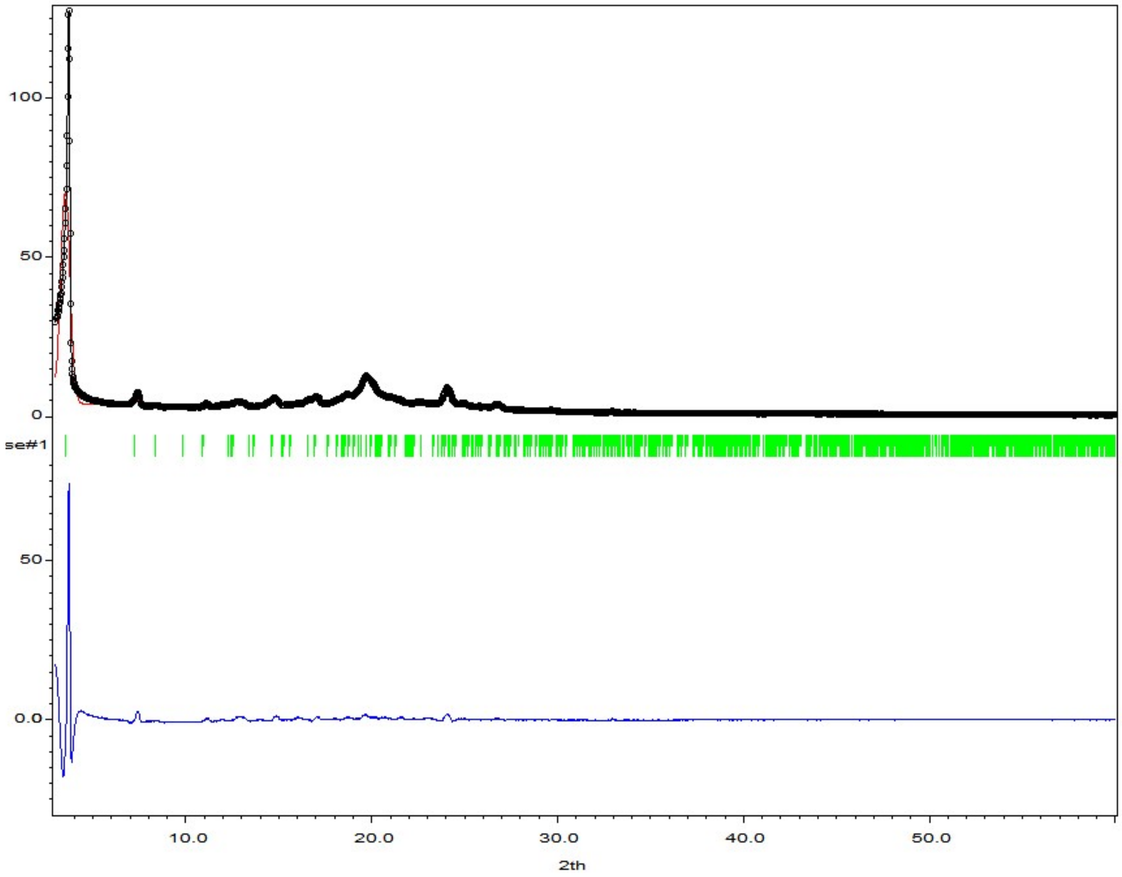

Figure S33. PXRD pattern obtained for the bulk sample of **6**. Vertical axis – intensity, black curve – experimental pattern, red – Le Bail-fitted model, green bars – reflection positions (taking into account both $K_{\alpha1}$-$K_{\alpha2}$ splitting), blue – residual.

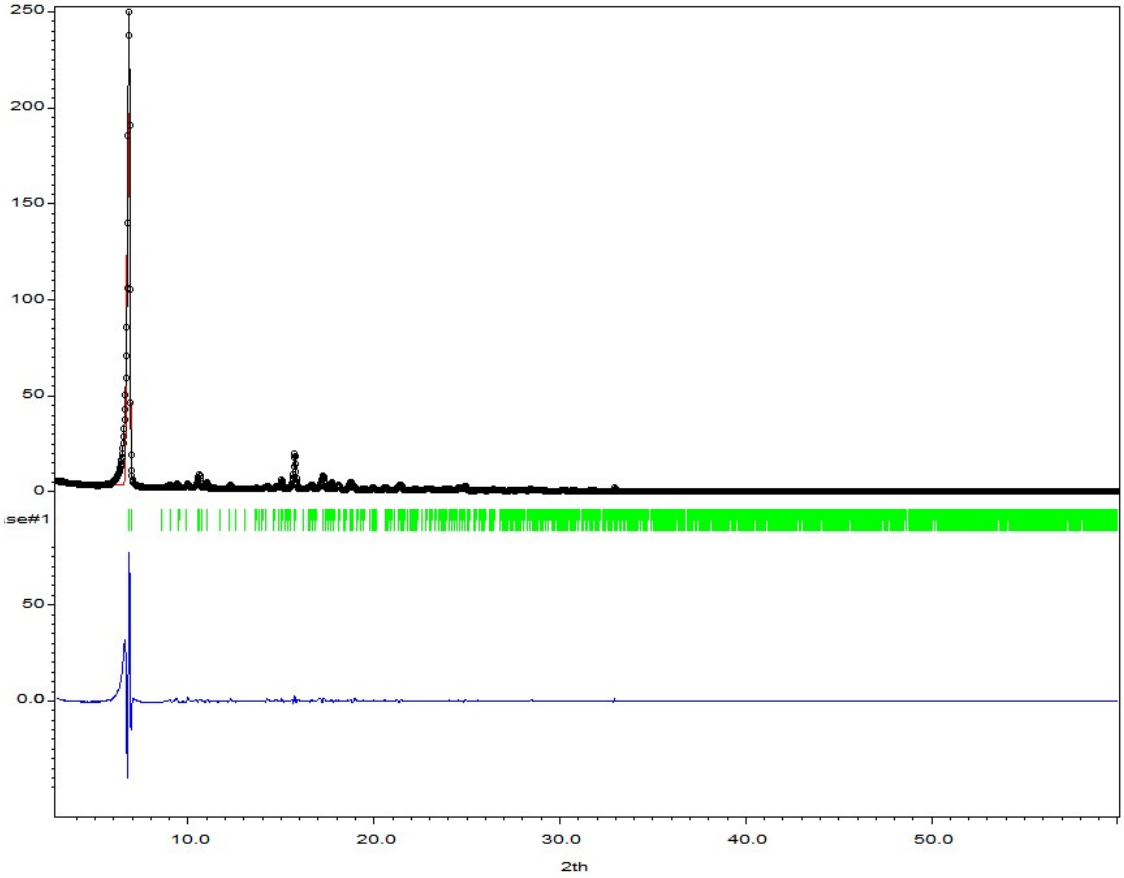

Figure S34. PXRD pattern obtained for the bulk sample of **7**. Vertical axis – intensity, black curve – experimental pattern, red – Le Bail-fitted model, green bars – reflection positions (taking into account both $K_{\alpha1}$-$K_{\alpha2}$ splitting), blue – residual.

6. Structural remarks and conjugation effects

The conjugation effects between donor (core) and acceptors may have a profound influence on the spectroscopic properties. Therefore, while looking at the molecular structures we analysed the C3–C2–C5–C13 torsion angles which describe the relative rotation of the acceptor in relation to the donor core. The results are summarised in **Table S11**. The rotation angle varies in the series of the compounds, but not very significantly. The lowest value (*ca*. 17°) is for the compound **6**, for majority of the complexes it is about 30° (compounds **1**, **2a**, **4** and **7**), whereas is reaches *ca.* 50° for complexes **3** and **3a**. Importantly, the compound **6**, in which the angle indicates the most flat conformation and best aromatic rings' conjugation, shows the largest emission red-shift when compared to the remaining examined compounds in cyclohexane solution and in the solid-state. Nevertheless, the conjunction effect results also in the emission quenching observed for the solid-state sample, which is in agreement with our previous contribution.[2]

Table S11. Torsion angles for compounds **1–4** and **6–7** indicating the rotation between the donor (core) and the acceptor part of the molecule. Experimental values are from the crystal structures, theoretical are from optimized isolated-molecule geometries.

Dye	*Torsion angle, $\tau_{C3-C2-C5-C6/13}$ / °* [a]	
	Experiment	*Theory (B3LYP/6-31G**)*
1	31.4(4) [b] / 31.7(5) [c]	27.8
2a	30.6(2) [d]	33.0
3	55.8(1) [b]	45.6
3a	50.1(4) [d]	45.7
4	30.4(4) [d]	33.7
6	17.3(4) [b]	25.3
7	35(2) [e] / 30.1(3) [f]	32.1

[a] Comment: this torsion angle represents, in each case, the angle between the donor (core) and the acceptor part of the molecule; all angles are given positive due to the fact that all molecules lie on the inversion centre. [b] C3–C2–C5–C6 angle. [c] C34–C33–C36–C37 angle (2nd molecule, only in 1). [d] C3–C2–C5–C13 angle. [e] C3–C2–C5A–C13A angle (more occupied disordered part 'A'). [f] C32–C31–C34–C42 angle (2nd molecule, only in 7).

Interesting observations regarding the supramolecular arrangement of molecules in crystals can be made based on the detailed analysis of the Hirshfeld surfaces and related fingerprint plots. To compare all structures we computed the ratios of percentage contributions of various interactions – both inside and outside of the Hirshfeld surface, and both X⋯Y and the reciprocal ones. The results for the H⋯X / H⋯H (X = C, O, N, S) ratios are shown in Figure S35. The most significant differences are visible for the compounds **2a** and **3a** when compared to the other ones. Clearly, large H···C / H···H ratios (reaching almost 1.0 in the case of **2a**) indicate that the smaller molecules exhibit larger variety of intermolecular interactions than the ones with long alkyl chains. These chains in compounds **1**, **3**, **4** and **6** are always in a straight conformation in the crystal structure (*i.e.* the chains do not tend to bend or fold up). Thus, as such they support the packing of these molecules where the 'hydrophobic' parts interact mainly one with another via weak dispersive H···H forces. This is best visible in compounds **4** and **6**, where even the interpenetration of long chains between neighbouring layers can be seen (Figure S36). Note the long chains were introduced in these systems to increase their solubility in a larger variety of organic solvents.

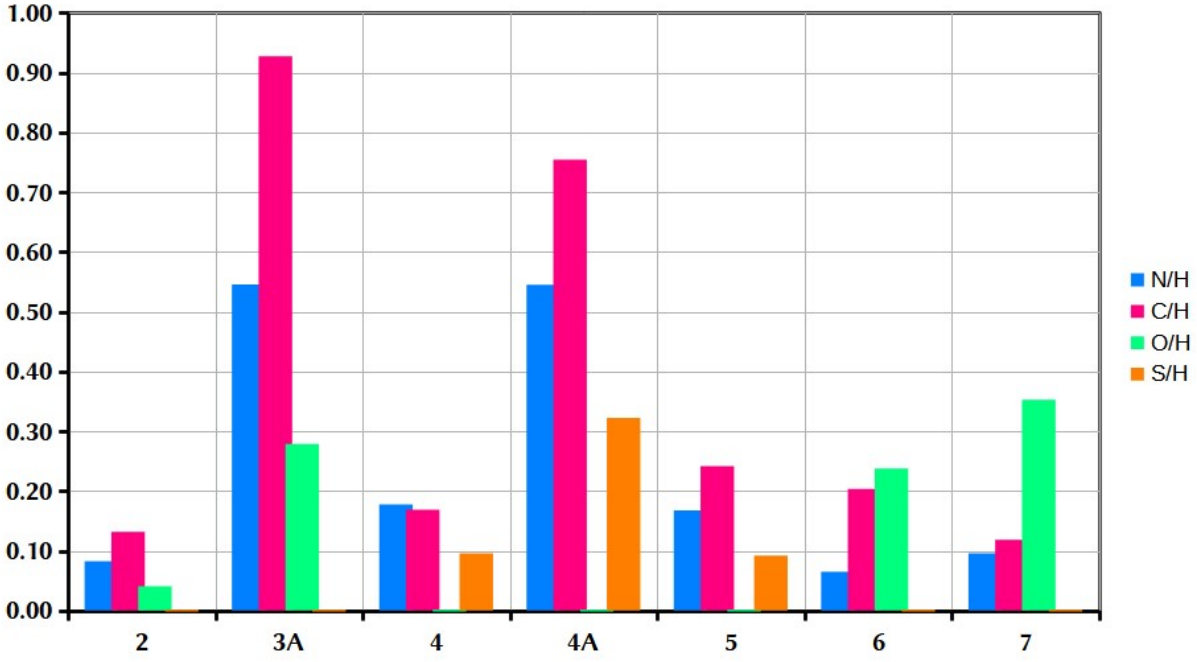

Figure S35. Ratio of interactions based on Hirshfeld surface analysis. X/N (X = N – blue, C – red, O – green, S – sulphur) in legend means the ratio of percentage contributions of N···H + H···N interactions over the percentage contribution of H···H interactions.

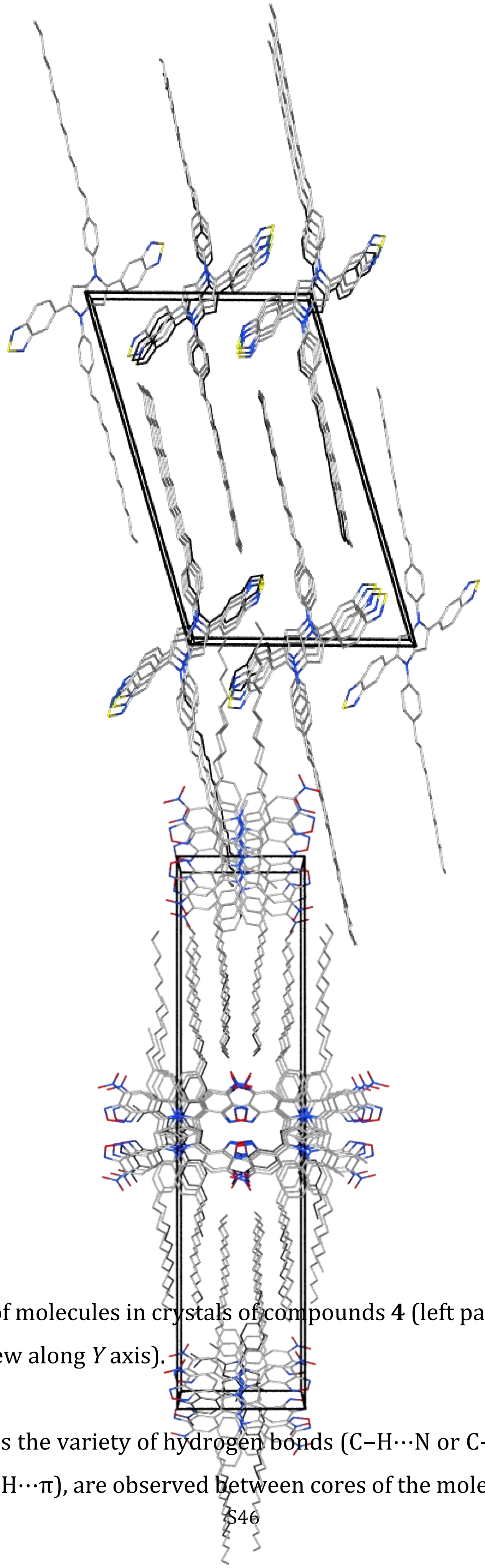

Figure S36. Packing of molecules in crystals of compounds **4** (left panel; view along *Z* axis) and **6** (right panel; view along *Y* axis).

For all compounds the variety of hydrogen bonds (C−H···N or C−H···O), or other weak interactions (π···π, C−H···π), are observed between cores of the molecules. In the structure

6, also some O⋯N intermolecular interactions are present, namely the two benzoxadiazole units interact with each other, contributing to the overall stability of the crystal. Similar observation can be made for the structures **2a**, **3** and **4**, where the sulphur atoms are present. Here, some extra C–H⋯S and possibly S⋯π interactions can be established – the latter ones are formed presumably due to the larger size of the sulphur atom when compared to the oxygen one (similar interactions with oxygens from the heterocyclic rings are not observed here). In compound **1** also interactions with the solvent are present (*e.g.* C–H⋯N or C–H⋯Cl), as described previously.[2] Among intermolecular interactions of investigated compounds a possible explanation of unusual θ angle (which is the angle between donor and acceptor moiety) can be found. The hydrogen bond between N9 and H3 atoms in the structure of **3**, **3a** and **4** are special for compounds containing sulphur, as N9 atom is the one from the acceptor moiety. This hydrogen bond can force a twist of molecule, which in case of **4** is not so large due to the connection through position 5 of the acceptor, while for both **3** and **3a** the presence of the hydrogen bond forces twist resulting in large θ value. This hydrogen bond can be the cause, as the crystal structure is thermodynamically stable, and the hydrogen bond has energy of several kcal/mol (around 6 kcal/mol), what is the difference between conformation of **1** with 55.77° θ angle and optimized **1** as well as around the difference between conformation of **3** with 26.38° θ and optimized structure of **3**.

The hydrogen bond between N9 and H3 atoms form exclusively for containing-sulphur compounds. It is possible due to the opposite character of the nitrogen atom in 2,1,3-benzoxadiazole and 2,1,3-benzothiadiazole causes by polarization in the diazole ring. Due to the distance between N9 and H3 atoms (*ca.* 2.65 Å) the assumption that electrostatic potential drives the hydrogen bond formation can be made.[14] In case of 2,1,3-benzothiadiazole there is slightly higher electrostatic potential around nitrogen atoms, which can enable formation of N9–H3 hydrogen bond (Figure S37).

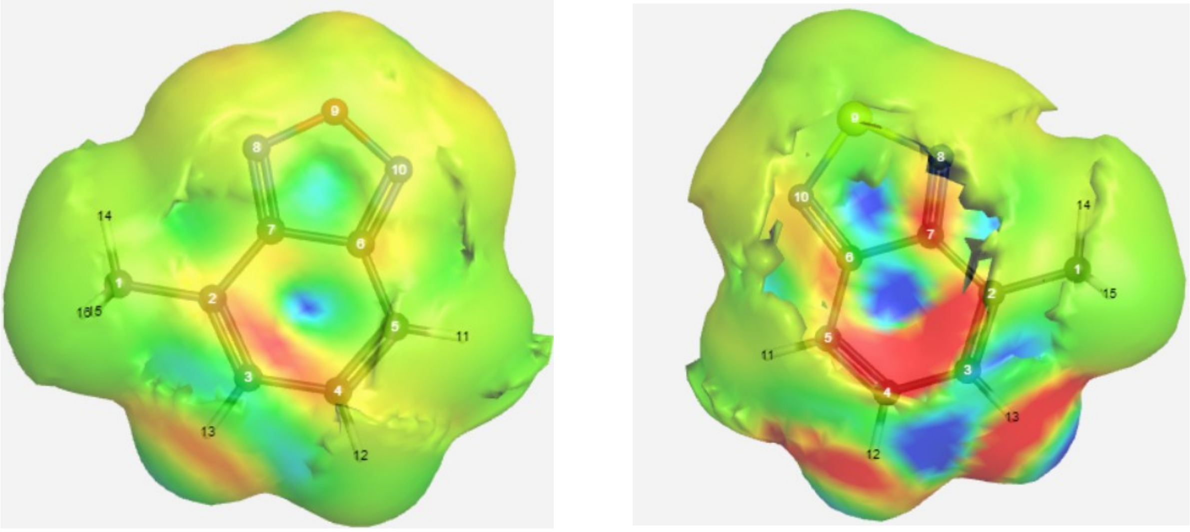

(a) (b)

Figure S37. Electrostatic potential surfaces of 4-methyl-2,1,3-benzoxadiazole (a) and 4-methyl-2,1,3-benzothiadiazole (b). Colour scale from −0.193 au (red) to +0.336 au (blue).

We found an interesting dependence of the absorption maximum shift in the solid state on cosine of the C3−C2−C5−C6/C13 dihedral angle, θ. This dled us to investigate the dependence of the absorption maximum shift between the solid state and solution on θ. In our example, we have non-zero θ values, which breaks the one-dimensional quantum well model, but leads to the 2-dimensional one. The explanation behind the application of this model, could be that there is a similar conformation that is the most stable for all compounds studied in solution, while in the solid state θ values are different due to packing and intra- and intermolecular interactions.

We performed a two-dimensional geometry scan changing θ angles by 10° in range of 0–90° for compounds **1, 2a, 3, 3a, 4, 6** and **7**, using Gaussian 16 program[15]. Then we calculated optimized geometry for each compound, with relaxed dihedral angles and with θ fixed to 38.48°. We used DFT(B3LYP) level of theory for geometry optimization in 6-31G(2d,2p) basis set. Then we calculated UV-Vis spectra to investigate the dependence of absorption maxima on θ. We used TD-DFT(CAM-B3LYP)[16] level of theory for UV-Vis spectra calculations in 6-31G(2d,2p) basis set. The change of functional is due to charge transfer excited state type for investigated molecules. During the analysis we have taken into consideration only HOMO → LUMO transition, which is involved in the lowest singlet-singlet transition in terms of energy. Furthermore we visualised molecular orbitals and check the dependence of HOMO-LUMO gap in nanometers on $\cos^2\theta$. The dependence of maximum of absorption in nanometers on $\cos^2\theta$ is almost linear (Figure S38).

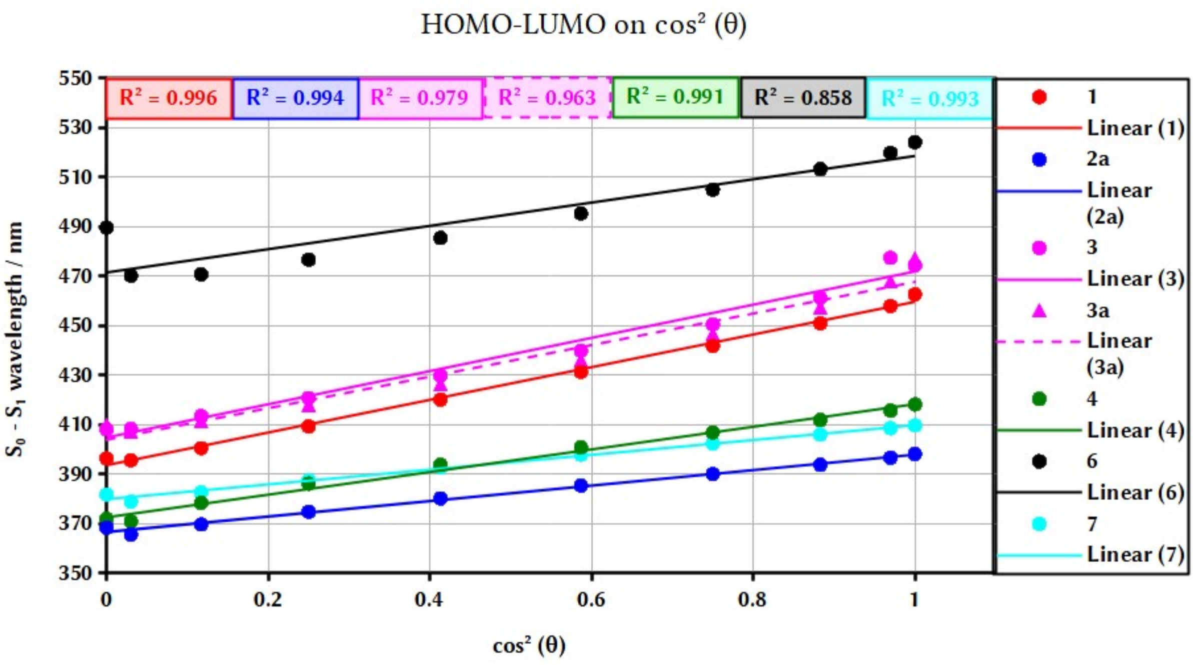

Figure S38. HOMO-LUMO gap in nm *vs.* $\cos^2\theta$.

The most promising aspect is that the linear dependence can be fitted for all examined compounds. The deviation of compound **6** for large θ angles can be explained by the steric hindrance or some intramolecular interactions as π···π stacking. Nevertheless, it is also possible that the charge transfer effect is so strong, that it is not probably approximated even using CAM-B3LYP functional. What is worth noting, the HOMO-LUMO gap is the lowest for **6**, which exhibits red-shifted absorption maximum comparing to the rest of the investigated compounds. Compounds **1** and **3** are similar to each other and exhibit red-shifted absorption maxima comparing to the compounds **2a, 4** and **7.** Moreover, compound **7** possess maximum of absorption nearly 10 nm above its analogue, **2a**, which differs by two oxygen atoms in acceptors moieties. The theoretical calculations results corresponds to experimental data, however the energies are much higher for theoretical calculations, with around 100 nm error. Nonetheless, the tendencies are the same for both datasets. Then we performed detailed analysis of the dependence of oscillator strength on $\cos\theta$, trying to fit a linear model (Figure S39).

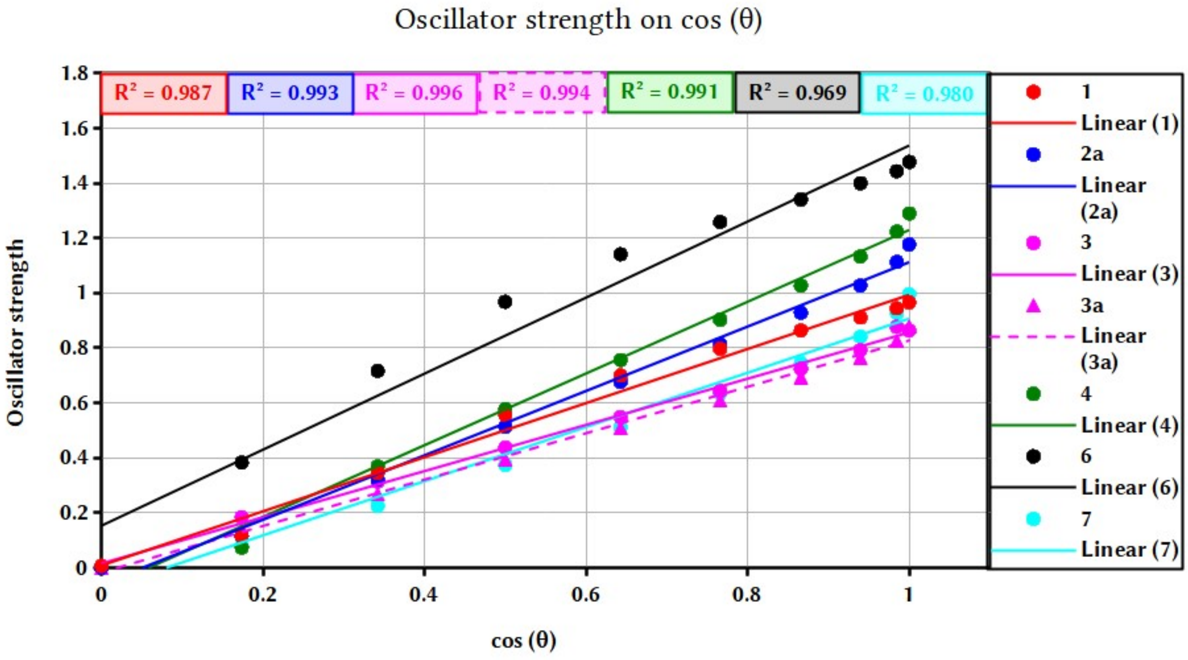

Figure S39. Oscillator strength *vs.* $\cos \theta$.

A linear dependence of oscillator strength on $\cos \theta$ was fitted, with R^2 coefficient as high as 0.96. A linear model would be supported by the fact that an oscillator strength is proportional to the overlap integral, which is proportional to the cosine of the angle between orbitals, in our example it should be proportional to the cosine of the θ. Compound **6** exhibits extremely large oscillator strength. If we have a closer look, we will notice that there is a dependence between an oscillator strength from the theoretical calculations and molar absorption coefficient from the experiment – **4** and **7** which exhibit the lowest ε value, exhibit also the lowest f value for each θ angle. We also performed also molecular orbitals analysis to check, if they are consistent with the proposed model. We have used B3LYP functional in DFT theory level and 6-31G** basis set to calculate molecular orbitals. For each compound we calculated HOMO and LUMO energy, and the difference – HOMO-LUMO gap (Table S12).

Table S12. HOMO-LUMO energy gap on dihedral angle θ in eV.

θ	1	**2a**	**3**	**3a**	**4**	**6**	**7**
0	-2.400	-2.687	2.331	-2.315	-2.550	-2.108	-2.634
10	-2.431	-2.709	-2.313	-2.364	-2.573	-2.133	-2.632
20	-2.475	-2.732	-2.397	-2.417	-2.595	-2.168	-2.651

30	-2.532	-2.759	-2.450	-2.470	-2.623	-2.209	-2.675
40	-2.595	-2.790	-2.501	-2.519	-2.655	-2.256	-2.702
50	-2.657	-2.819	-2.548	-2.563	-2.685	-2.299	-2.726
60	-2.704	-2.839	-2.585	-2.595	-2.708	-2.325	-2.742
70	-2.712	-2.844	-2.608	-2.612	-2.717	-2.317	-2.739
80	-2.650	-2.826	-2.650	-2.610	-2.699	-2.250	-2.713
90	-2.612	-2.784	-2.582	-2.565	-2.672	-2.052	-2.664

Despite HOMO-LUMO gap values are quite similar for all compounds besides **6** (which is consistent with earlier analysis), the HOMO and LUMO energies are quite different (Figure S40). The HOMO energies varies significantly for the investigated compounds. Compound **6** has the lowest HOMO energy, then the **2a** and **7** exhibit almost the same value of HOMO energy, which is also quite low. Another pair, **4** and **1** possess similar HOMO energy, despite being definitely different in terms of structure. Finally compound **3** (and **3a**) have the highest from HOMOs. It is worth mentioning that the HOMO orbital is localized mainly on the donor core, independently on the θ value.

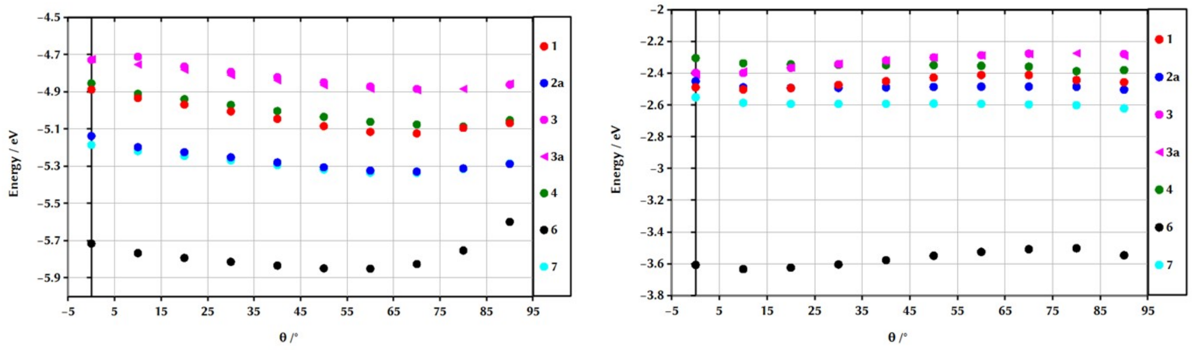

Figure S40. HOMO (left) and LUMO (right) energies as functions of θ.

The LUMO energy values are almost the same for all examined compounds, besides **6**, which exhibits over 1 eV lower LUMO than its non-nitro analogue, **1**. What is interesting, **7** is the second one with low LUMO energy, which slightly supports its quasi-nitro properties. The dependence on θ are various and for HOMO, LUMO and LUMO+1 it was unclear, which function could be fitted. However for HOMO-LUMO gap dependence on $\cos\theta$ a linear dependence can be fitted for all examined compounds. Also a linear dependence on $\cos^2\theta$ can be fitted (Figure S41).

Both linear dependence on $\cos\theta$ and $\cos^2\theta$ can be fitted, with the R^2 as high as 0.95 and 0.97 respectively. However, a linear dependence on $\cos\theta$ is not in agreement with the quantum well model, moreover for the dependence on $\cos^2\theta$ the parameters of fit are better.

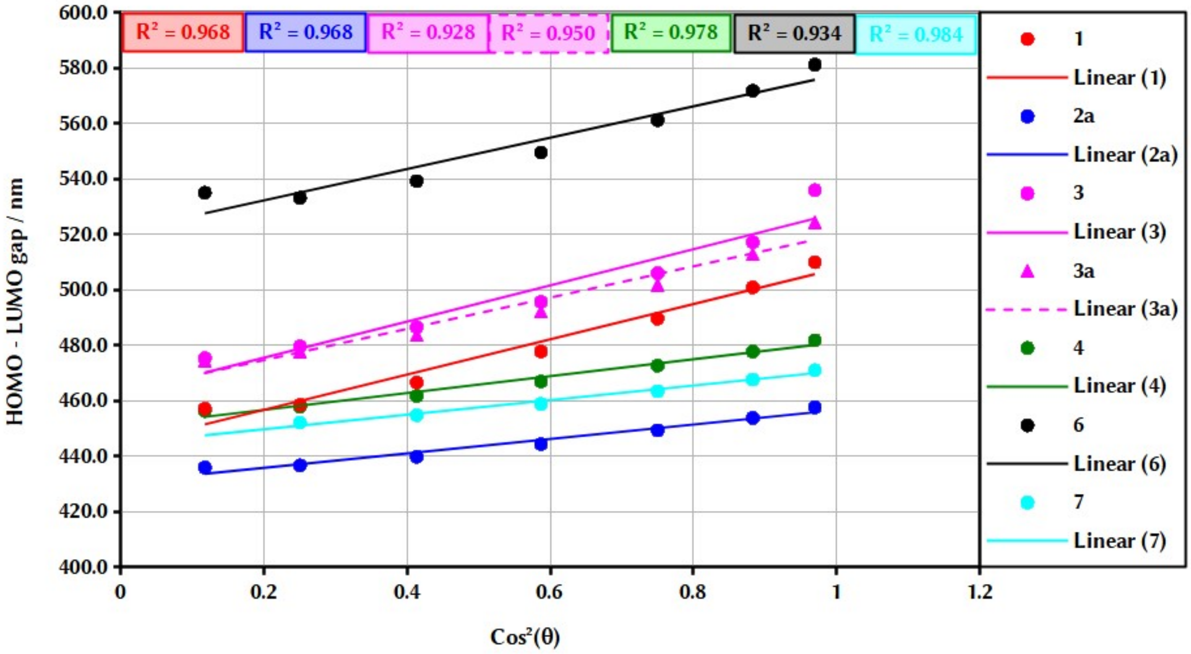

Figure S41. Relation of HOMO-LUMO gap *vs.* $\cos^2\theta$ in the range 10–70°.

What is interesting, on Figure S41 the θ range is not full. For the dependence on $\cos^2\theta$ the range was narrowed to the 10–70°. The main deviation out of the range is the mixing of LUMO and LUMO+1 orbitals and the charge transfer to only one acceptor moiety which is possibly a demonstration of the ground state-symmetry breaking for A–D–A systems with extremely large θ angles.

There are two groups of compounds presented on Figure S6.7, as compounds **1, 3** and **6** exhibit almost identical slope in the dependence of HOMO-LUMO gap on $\cos^2(\theta)$ and compounds **2, 4** and **7** exhibit almost identical slope also. The differences within group are below 15%, while between groups the slopes differs by the factor of 2. These differences indicate changes in coupling while bridging by position 4 (compounds **1, 3** and **6**) in comparison to bridging by position 5 (compounds **2**, **4** and **7**). Indeed, from the spectroscopic studies we know that there is a stronger conjugation between donor and acceptor parts when they are bridged by position 4, which reveals as higher slope's value on Figure S41.

7. Theoretical calculations

We used density functional theory (DFT) level with the hybridization of exchange-correlation functional BLYP with the 37% of Hartree-Fock (HF) or exact exchange and a 63% scaling factor for Slater exchange (so the hybrid functional is B3LYP-37)[17–20] for the ground state (S_0) molecular optimization for TAPP dyes **6–8**. Using the ground state minimum geometry, we then carried out time-dependent density functional theory (TDDFT) calculations for the singlet molecular excitation (absorption) up to five excited states and lowest singlet excited state (S_1) geometry relaxation (emission) as well with same 6-31G(d,p) basis function and B3LYP-37 functional.[21] Polarizable continuum model (PCM)[19] with various solvents (same as investigated in experiment) was applied in the TDDFT[22–25] formalism to study the solvent effects on the optical absorption and emission properties of the studied dyes. The spin–orbit coupling matrix elements $\langle S_1 | H_{SO} | T_n \rangle$ between the singlet (S_1) state and the relevant triplet states T_n (below the S_1 level) were calculated at the TDDFT/B3LYP/6-31G(d,p) level using *MOLSOC* program.[26]

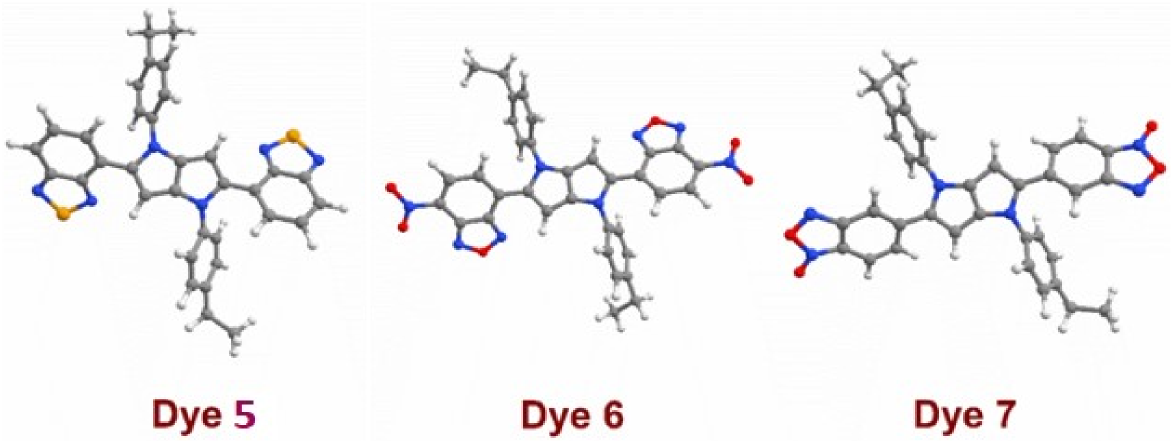

Figure S42. Optimized geometries for investigated dyes **5–7** in the gas phase.

The k_{IC}, k_r rate constants and fluorescence quantum yield (Φ_{fl}) were calculated using the algorithm described in references 27–29.[27–29] This algorithm uses the quantum chemical computed matrix elements, energies such as the non-adiabatic coupling matrix elements (NACME), between the S_1 and S_0 states, the spin-orbit coupling matrix elements (SOCME) between S_1 and energy lower triplet electronic states, and the transition electric dipole moment between the S_1 and S_0 states as the input parameters. These input data were obtained using the DFT and at the TDDFT level for the ground and excited states using the

B3LYP functional and the 6-31G** basis set. Most of the quantum chemical calculations were performed with Gaussian 16.[15]

The non-radiative rate constants for internal conversion (k_{IC}) and the intersystem crossing rate constants were calculated using Plotnikov's formula[30] within Herzberg-Teller (HT) and anharmonic, the Dushinsky effect approximations using the Morse oscillator model as[27]

$$k_{nr} = \sum_{n} \left|V_{i0,fn}\right|^2 \Gamma_{fn} \left(\Delta_{if}^2 + \frac{\Gamma_{fn}^2}{4}\right)^{-1} \tag{E4}$$

where i is the initial electronic state, f is the final electronic state, n is a vibrational level of f state, Γ_{fn} is the relaxation width of the vibrational level $|fn\rangle$, $\Delta_{if} = |E_{i0} - E_{fn}|$ is the energy difference between the initial and final vibrational states, and $V_{i0,fn}$ is the matrix element of a perturbation operator. The perturbation operator is the spin-orbit coupling interaction for ISC transitions and the non-adiabatic coupling interaction for IC processes. Usually Γ_{fn} is about 10^{14} s^{-1} and does not depend strongly on n, and Δ_{if} is about 100 cm^{-1} and we can assume[30]

$$k_{nr} = \frac{4}{\Gamma_f}\sum_{n}\left|V_{i0,fn}\right|^2.$$

The k_{IC} was calculated as

$$k_{IC-HT} = \frac{4}{\Gamma_f}\left[D^2\left(\sum_{n}\prod_{k} g_k^2\right) + \sum_{i} P_i^2 t_i^2 \left(\sum_{n}\prod_{k \neq i} g_k^2\right) + \sum_{i,j \neq i} W_{ij}^2 t_i^2 b_{ij}^2 \left(\sum_{n}\prod_{\substack{k \neq i \\ k \neq j}} g_k^2\right)\right]. \tag{E5}$$

Here,

$$g_j = \frac{N_0 N_n \Delta^{\frac{b_0}{2}}}{\alpha} I_n\left(\frac{\Delta + 1}{2}, \frac{b_n + b_0}{2} - 1, b_n\right), \tag{E6}$$

$$t_j = N_0 N_n \Delta^{\frac{b_0}{2}} \left[\frac{1}{2} I_n\left(\frac{\Delta + 1}{2}, \frac{b_n + b_0}{2}, b_n\right) - \frac{1}{2} b_n I_n\left(\frac{\Delta + 1}{2}, \frac{b}{\,}\right.\right. \tag{E7}$$

,

$$b_j = \left[K + \ln\left(\frac{2\beta}{\alpha}\right)\right] g_j - \frac{N_0 N_n \Delta^{\frac{b_0}{2}}}{\alpha^2} \left[\frac{dI_n\left(\frac{\Delta + 1}{2}, \frac{b_n + b_0}{2} - 1, b_n\right)}{d\left(\frac{b_n + b_0}{2} - 1\right)}\right]. \tag{E8}$$

The wave function of Morse oscillator is $\psi_n(R) = N_n \exp(-z/2) z^{b_n/2} L_n^{b_n}(z)$, where $z = 2\beta \exp\left[-\alpha\left(R - R_e\right)\right]$, $b_n = 2\beta - 2n$, $\beta = \alpha^{-1}\sqrt{2D_e}$. The D_e value is the dissociation energy, α is an anharmonicity constant, R_e is the equilibrium distance,

$$N_n = \left[\frac{\alpha b_n n!}{\Gamma\left(b_n + n + 1\right)}\right]^{1/2},$$

$L_n^{b_n}(z)$ is the n-th Laguerre polynomial, and $\Gamma\left(b_n + n + 1\right)$ is the Gamma function. Parameters D_e and α can be obtained from the anharmonicity parameter χ and the energy ω as $D_e = \omega/4\chi$ and $\alpha = \sqrt{2\omega\chi}$. We used 0.02 for χ. Here, $\Delta = \exp(-\alpha K)$,

$$I_n(A,B,C) = \int_0^\infty \exp(-Az)\, z^B L_n^C(z)\, dz,$$

K is the displacement of oscillator in equilibrium position. In eq. (E8)

$$\frac{dI_n\left(\frac{\Delta + 1}{2}, \frac{b_n + b_0}{2} - 1, b_n\right)}{d\left(\frac{b_n + b_0}{2} - 1\right)} = \frac{dI_n(A,B,C)}{dB}$$

and can be estimated numerically. The $I_n(A,B,C)$ can be written analytically as:

$$I_n(A,B,C) = \frac{\Gamma(1 + B)\Gamma(C + n + 1)}{\Gamma(n + 1)\Gamma(C + 1)} A^{-1-B}{}_2F_1\left(1 + B,\ -n, 1 + C, \frac{1}{A}\right) \tag{E9}$$

The second term in eq. (E4) is the Franck-Condon (FC) one, the first and the third are the Herzberg-Teller terms. The D, $\bar{P}$ and W concern the non-adiabatic coupling matrix elements between the i-th and f-th electronic states and are expressed as

$$W_{jj'} = -\sum_v \sum_q \sum_{v'} \sum_{q'} \left\langle \varphi_i\left(\bar{r},\bar{s},\bar{R}\right) \frac{\partial \varphi_f\left(\bar{r},\bar{s},\bar{R}\right)}{\partial R_{vq}} \right\rangle \Bigg|_{\bar{R} = \bar{R}_0} M_v^{-\frac{1}{2}} M_{v'}^{-\frac{1}{2}} L_{vqj} L_{v'q'j'}, \tag{E10}$$

$$D = -\sum_v \sum_q (2M_v)^{-1} \left\langle \varphi_i\left(\bar{r},\bar{s},\bar{R}\right) \left| \frac{\partial^2}{\partial R_{vq}^2} \right| \varphi_f\left(\bar{r},\bar{s},\bar{R}\right) \right\rangle \Bigg|_{\bar{R} = \bar{R}_0}, \tag{E11}$$

$$P_j = -\sum \sum M_v^{-\frac{1}{2}} L_{vqj} \left\langle \varphi_i\left(\bar{r},\bar{s},\bar{R}\right) \frac{\partial \varphi_f\left(\bar{r},\bar{s},\bar{R}\right)}{\partial R_{vq}} \right\rangle \Bigg|_{\bar{R} = \bar{R}_0}. \tag{E12}$$

Here,

$$\left\langle \varphi_i\left(\bar{r},\bar{s},\bar{R}\right) \frac{\partial \varphi_f\left(\bar{r},\bar{s},\bar{R}\right)}{\partial R_{vq}} \right\rangle \Bigg|_{\bar{R} = \bar{R}_0}$$

and

$$\left\langle \varphi_i(\bar{r},\bar{s},\bar{R}) \left| \frac{\partial^2}{\partial R_{vq} \partial R_{v'q'}} \right| \varphi_f(\bar{r},\bar{s},\bar{R}) \right\rangle \Big|_{\bar{R} = \bar{R}_0}$$

are the non-adiabatic coupling matrix elements (NACMEs) of the first and second order, respectively. M_v is the mass of the v-th atom, L_{vqj} are coefficients of the linear relation between the Cartesian (R) and the normal coordinates (Q): $R_{vqj} - R_{vqj} = M_v^{-1/2} L_{vqj} Q_j$.

The Lagrange multiplier technique applies to

$$\prod_{\substack{k \neq i \\ k \neq j}} g_k^2$$

at HT approximation and to

$$\prod_{k \neq i} g_k^2$$

at FC approximation. The Lagrange function is

$$L = \ln \left[\prod_{k=1}^{3N-6} \left(\frac{e^{-y_k} y_k^{n_k}}{n_k!} \right) \right] - \lambda \left(\sum_{k=1}^{3N-6} n_k \omega_k + E_{if} \right),$$

and the solution of

$$\left[\sum_{k=1}^{3N-6} y_k \exp(-\omega_k \lambda) \omega_k \right] = E_{if}$$

leads to $n_k = y_k \exp(-\omega_k \lambda)$, where λ is the Lagrange multiplier. The Dushinsky effect was included in W and $\bar{P}$ matrix and vector as[27]

$$\tilde{P}_i = \sum_l P_{pq} J_{pq} + \sum_{l,m \neq l} K_l P_{lm} J_{mi}, \tag{E13}$$

$$\tilde{W}_{ij} = \sum_{l,m \neq l} P_{lm} J_{li} J_{mj}. \tag{E14}$$

Here J is Dushinsky matrix.

The radiative rate constants (k_r) are calculated as[31]

$$k_r(p \to q) = \frac{1}{1.5} f \cdot E_{pq}, \tag{E15}$$

where f is the oscillator strength.

The non-radiative rate constants for intersystem crossing k_{ISC} are calculated as[31]

$$k_{ISC} = \frac{4}{\Gamma_f} \left(H_{SO}^{if} \Big|_{\bar{R} = \bar{R}_0} \left[\prod_{k=1}^{3N-6} \left(\frac{e^{-y_k} y_k^{n_k}}{n_k!} \right)^{1/2} \right] + \sum_{j=1}^{3N-6} t_j W_j \left[\prod_{\substack{k=1 \\ k \neq j}}^{3N-6} \left(\frac{e^{-y_k} y_k^{n_k}}{n_k!} \right)^{1/2} \right] \right)^2, \tag{E16}$$

where the W_j is given by

$$W_j = \sum_v \sum_q \frac{\partial H_{SO}^{if}}{\partial R_{vq}}\bigg|_{\bar{R} = \bar{R}_0} M_v^{-1/2} L_{vqj}.$$

Here H_{SO}^{if} is matrix element of SOC-operator.

The fluorescence quantum yield from the S_1 state can be obtained as[32]

$$\Phi_{fl} = \frac{k_r}{k_r + k_{IC} + \sum_i k_{IST_i}}, \tag{E17}$$

where k_{IST_i} is a ISC rate constant between S_1 and energetically lower triplet states T_i, k_r and k_{IC} are radiative and IC rate constants of the electronic transition from S_1 to the ground state S_0, respectively.

Table S13. Computed absorption wavelengths (λ), energies (E), and oscillator strengths (f) for the studied dye **5** (with ethyl side chain) in different solvent states.

Solvent	Excited state	Wavelength (λ) (nm)	Energy (E) (eV)	Oscillator strength (f)	Exp. values (nm)
Cyclohexane (ε = 2.0165)	S_1	544	2.28	0.6221	544
	S_2	493	2.51	0.0000	
	S_3	392	3.16	0.0138	
	S_4	368	3.37	0.0005	
	S_5	328	3.78	0.0009	
Dioxane (ε = 2.2099)	S_1	544	2.28	0.6205	530
	S_2	493	2.52	0.0000	
	S_3	392	3.16	0.0138	
	S_4	368	3.37	0.0005	
	S_5	328	3.78	0.0009	
Toluene (ε = 2.3741)	S_1	545	2.27	0.6331	544
	S_2	493	2.51	0.0000	
	S_3	392	3.16	0.0141	
	S_4	368	3.37	0.0006	
	S_5	328	3.78	0.0009	
THF (ε = 7.4257)	S_1	538	2.30	0.6111	536
	S_2	489	2.54	0.0000	
	S_3	391	3.17	0.0132	
	S_4	367	3.38	0.0006	
	S_5	327	3.79	0.0008	
DCM (ε = 8.93)	S_1	538	2.30	0.6144	532
	S_2	489	2.54	0.0000	
	S_3	391	3.17	0.0133	
	S_4	367	3.38	0.0006	
	S_5	327	3.79	0.0008	

Table S14. Computed absorption wavelengths (λ), energies (E), and oscillator strengths (f) for the studied dye **6** (with ethyl side chain) in different solvent states.

Solvent	Excited state	Wavelength (λ) (nm)	Energy (E) (eV)	Oscillator strength (f)	Exp. values (nm)
Cyclohexane (ε = 2.0165)	S_1	572	2.17	1.4906	618
	S_2	452	2.74	0.0029	
	S_3	444	2.79	0.0375	
	S_4	380	3.26	0.0007	
	S_5	344	3.60	0.0024	
Dioxane (ε = 2.2099)	S_1	573	2.16	1.4899	612
	S_2	453	2.74	0.0029	
	S_3	446	2.78	0.0374	
	S_4	382	3.25	0.0007	
	S_5	345	3.60	0.0022	
Toluene (ε = 2.3741)	S_1	578	2.15	1.5101	620
	S_2	455	2.73	0.0030	
	S_3	447	2.77	0.0379	
	S_4	383	3.24	0.0007	
	S_5	346	3.59	0.0022	
THF (ε = 7.4257)	S_1	584	2.12	1.4889	624
	S_2	461	2.69	0.0030	
	S_3	460	2.69	0.0372	
	S_4	393	3.15	0.0007	
	S_5	354	3.50	0.0015	
DCM (ε = 8.93)	S_1	587	2.11	1.4947	648
	S_2	462	2.68	0.0030	
	S_3	462	2.69	0.0374	
	S_4	394	3.14	0.0007	
	S_5	355	3.49	0.0014	

Table S15. Computed absorption wavelengths (λ), energies (E), and oscillator strengths (f) for the studied dye **7** (with ethyl side chain) in different solvent states.

Solvent	Excited state	Wavelength (λ) (nm)	Energy (E) (eV)	Oscillator strength (f)	Exp. values (nm)
Cyclohexane (ε = 2.0165)	S_1	448	2.76	0.8885	494
	S_2	405	3.06	0.0167	
	S_3	365	3.40	0.0490	
	S_4	347	3.57	0.0153	
	S_5	343	3.62	0.5531	
Dioxane (ε = 2.2099)	S_1	449	2.76	0.8882	490
	S_2	405	3.06	0.0165	
	S_3	366	3.39	0.0450	
	S_4	347	3.57	0.0152	
	S_5	343	3.62	0.5563	
Toluene (ε = 2.3741)	S_1	451	2.75	0.9067	492
	S_2	407	3.05	0.0170	
	S_3	367	3.38	0.0448	
	S_4	348	3.56	0.0156	
	S_5	343	3.61	0.5686	
THF (ε = 7.4257)	S_1	457	2.71	0.8924	497
	S_2	412	3.01	0.0157	
	S_3	374	3.31	0.0264	
	S_4	348	3.56	0.0116	
	S_5	342	3.63	0.5700	
DCM (ε = 8.93)	S_1	459	2.70	0.8983	495
	S_2	413	3.00	0.0158	
	S_3	375	3.31	0.0258	
	S_4	349	3.55	0.0113	
	S_5	342	3.63	0.5736	

Table S16. Computed $S_1 \rightarrow S_0$ emission wavelengths (λ), energies (E), and oscillator strengths (f) for the studied dye **5** (with ethyl side chain) in different solvent states.

Solvent	Wavelength (λ) (nm)	Energy (E) (eV)	Oscillator strength (f)	Exp. values (nm)
Cyclohexane (ε = 2.0165)	648	1.91	0.6749	622
Dioxane (ε = 2.2099)	651	1.91	0.6992	706
Toluene (ε = 2.3741)	653	1.90	0.7121	675
THF (ε = 7.4257)	681	1.82	0.8544	726
DCM (ε = 8.93)	683	1.81	0.8685	879

Table S17. Computed $S_1 \rightarrow S_0$ emission wavelengths (λ), energies (E), and oscillator strengths (f) for the studied dye **6** (with ethyl side chain) in different solvent states.

Solvent	Wavelength (λ) (nm)	Energy (E) (eV)	Oscillator strength (f)	Exp. values (nm)
Cyclohexane (ε = 2.0165)	637	1.94	1.5674	639
Dioxane (ε = 2.2099)	645	1.92	1.5924	699
Toluene (ε = 2.3741)	651	1.91	1.6110	679
THF (ε = 7.4257)	724	1.71	1.8097	722
DCM (ε = 8.93)	732	1.69	1.8285	737

Table S18. Computed $S_1 \rightarrow S_0$ emission wavelengths (λ), energies (E), and oscillator strengths (f) for the studied dye **7** (with ethyl side chain) in different solvent states.

Solvent	Wavelength (λ) (nm)	Energy (E) (eV)	Oscillator strength (f)	Exp. values (nm)
Cyclohexane (ε = 2.0165)	609	2.03	0.0510	542
Dioxane (ε = 2.2099)	609	2.04	0.0604	574
Toluene (ε = 2.3741)	609	2.04	0.0693	673
THF (ε = 7.4257)	615	2.27	0.1485	586
DCM (ε = 8.93)	617	2.25	0.1613	--

9. References

1 M. Tasior, O. Vakuliuk, D. Koga, B. Koszarna, K. Górski, M. Grzybowski, Ł. Kielesiński, M. Krzeszewski and D. T. Gryko, *J. Org. Chem.*, 2020, **85**, 13529–13543.

2 B. Szymański, S. R. Sahoo, R. Valiev, O. Vakuliuk, P. Łaski, K. N. Jarzembska, R. Kamiński, G. Baryshnikov, M. B. Teimouri and D. T. Gryko, *New J. Chem.*, 2024, **48**, 2416–2420.

3 G. Rauhut, A. A. Jarzecki and P. Pulay, *J. Comput. Chem.*, 1997, **18**, 489–500.

4 F. Xie, B. X. Li, C. Broussard and X. Xiao, *Bioorg. Med. Chem. Lett.*, 2013, **23**, 5371–5375.

5 B. Gadakh, G. Vondenhoff, E. Lescrinier, J. Rozenski, M. Froeyen and A. Van Aerschot, *Bioorg. Med. Chem.*, 2014, **22**, 2875–2886.

6 R. Neidlein and D. Knecht, *Helv. Chim. Acta*, 1987, **70**, 997–1000.

7 P. B. Ghosh and M. W. Whitehouse, *J. Med. Chem.*, 1968, **11**, 305–311.

8 G. M. Sheldrick, *Acta Crystallogr. Sect. A Found. Adv.*, 2015, **71**, 3–8.

9 G. M. Sheldrick, *Acta Crystallogr. Sect. C*, 2015, **71**, 3–8.

10 O. V Dolomanov, L. J. Bourhis, R. J. Gildea, J. A. K. Howard and H. Puschmann, *J. Appl. Crystallogr.*, 2009, **42**, 339–341.

11 A. L. Spek, *Acta Crystallogr. Sect. C Struct. Chem.*, 2015, **71**, 9–18.

12 F. H. Allen, *Acta Crystallogr. Sect. B*, 2002, **58**, 380–388.

13 C. R. Groom, I. J. Bruno, M. P. Lightfoot and S. C. Ward, *Acta Crystallogr. Sect. B*, 2016, **72**, 171–179.

14 T. Steiner, *Angew. Chemie Int. Ed.*, 2002, **41**, 48–76.

15 M. J. Frisch, G. W. Trucks, H. B. Schlegel, G. E. Scuseria, M. a. Robb, J. R. Cheeseman, G. Scalmani, V. Barone, G. a. Petersson, H. Nakatsuji, X. Li, M. Caricato, a. V. Marenich, J. Bloino, B. G. Janesko, R. Gomperts, B. Mennucci, H. P. Hratchian, J. V. Ortiz, a. F. Izmaylov, J. L. Sonnenberg, Williams, F. Ding, F. Lipparini, F. Egidi, J. Goings, B. Peng, A. Petrone, T. Henderson, D. Ranasinghe, V. G. Zakrzewski, J. Gao, N. Rega, G. Zheng, W. Liang, M. Hada, M. Ehara, K. Toyota, R. Fukuda, J. Hasegawa, M. Ishida, T. Nakajima, Y. Honda, O. Kitao, H. Nakai, T. Vreven, K. Throssell, J. a. Montgomery Jr., J. E. Peralta, F. Ogliaro, M. J. Bearpark, J. J. Heyd, E. N. Brothers, K. N. Kudin, V. N. Staroverov, T. a. Keith, R. Kobayashi, J. Normand, K. Raghavachari, a. P. Rendell, J. C. Burant, S. S. Iyengar, J. Tomasi, M. Cossi, J. M. Millam, M. Klene, C. Adamo, R. Cammi, J. W. Ochterski, R. L. Martin, K. Morokuma, O. Farkas, J. B. Foresman and D. J. Fox, 2016, Gaussian 16, Revision C.01, Gaussian, Inc., Wallin.

16 T. Yanai, D. P. Tew and N. C. Handy, *Chem. Phys. Lett.*, 2004, **393**, 51–57.

17 A. D. Becke, *J. Chem. Phys.*, 1993, **98**, 5648–5652.

18 C. Lee, W. Yang and R. G. Parr, *Phys. Rev. B*, 1988, **37**, 785–789.

19 R. Ditchfield, W. J. Hehre and J. A. Pople, *J. Chem. Phys.*, 1971, **54**, 724–728.

20 M. J. Frisch, J. A. Pople and J. S. Binkley, *J. Chem. Phys.*, 1984, **80**, 3265–3269.

21 J. Tomasi, B. Mennucci and R. Cammi, *Chem. Rev.*, 2005, **105**, 2999–3094.

22 R. Bauernschmitt and R. Ahlrichs, *Chem. Phys. Lett.*, 1996, **256**, 454–464.

23 M. E. Casida, C. Jamorski, K. C. Casida and D. R. Salahub, *J. Chem. Phys.*, 1998, **108**, 4439–4449.

24 R. E. Stratmann, G. E. Scuseria and M. J. Frisch, *J. Chem. Phys.*, 1998, **109**, 8218–8224.

25 G. Scalmani, M. J. Frisch, B. Mennucci, J. Tomasi, R. Cammi and V. Barone, *J. Chem. Phys.*, 2006, **124**, 94107.

26 S. G. Chiodo and M. Leopoldini, *Comput. Phys. Commun.*, 2014, **185**, 676–683.

27 R. R. Valiev, B. S. Merzlikin, R. T. Nasibullin, A. Kurtzevitch, V. N. Cherepanov, R. R. Ramazanov, D.

Sundholm and T. Kurtén, *Phys. Chem. Chem. Phys.*, 2023, **25**, 6406–6415.

28 R. R. Valiev, R. T. Nasibullin, V. N. Cherepanov, A. Kurtsevich, D. Sundholm and T. Kurtén, *Phys. Chem. Chem. Phys.*, 2021, **23**, 6344–6348.

29 R. R. Valiev, R. T. Nasibullin, V. N. Cherepanov, G. V Baryshnikov, D. Sundholm, H. Ågren, B. F. Minaev and T. Kurtén, *Phys. Chem. Chem. Phys.*, 2020, **22**, 22314–22323.

30 V. G. Plotnikov, *Int. J. Quantum Chem.*, 1979, **16**, 527–541.

31 R. R. Valiev, V. N. Cherepanov, R. T. Nasibullin, D. Sundholm and T. Kurten, *Phys. Chem. Chem. Phys.*, 2019, **21**, 18495–18500.

32 E. S. Medvedev and V. I. Osherov, 1995.